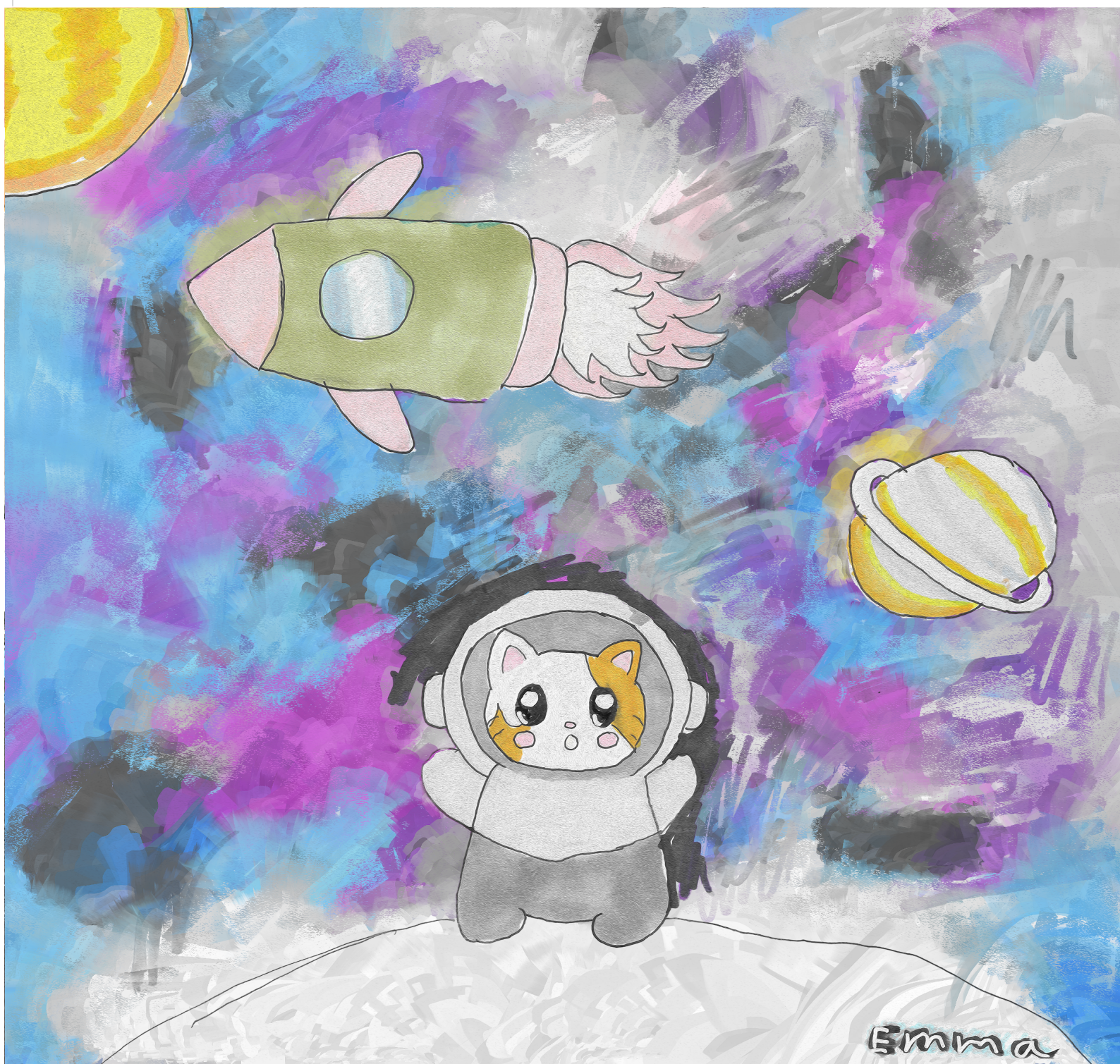**UiT** The Arctic University of Norway

Faculty of Science and Technology, Department of Physics and Technology

Mesospheric Dust - radar applications for detection and investigation

Tinna Líf Gunnarsdóttir
A dissertation for the degree of Philosophiae Doctor   August 2023

Mesospheric Dust - radar applications for detection and investigation

Tinna Lif Gunnarsdottir

A dissertation for the degree of Philosophiae Doctor (PhD)
at UiT The Arctic University of Norway

August 2023

"Your mind is a stream of colors. Extending beyond our sky
A land of infinite wonders. A billion light years from here"
—*Light My Love* by Greta Van Fleet

Abstract

Large amounts of meteoric particles ablate globally into the Earth's atmosphere each day, and they interact with the atmosphere through several processes in the mesosphere and below. These processes include dust charging, where dust is expected to influence the charge balance in the D-region of the ionosphere. Consequently, the charged dust particles can influence the incoherent scatter that is observed from the ionospheric plasma with radar.

Dust also plays a role in the formation of ice particles, and charge interactions of these ice particles take part in a process that forms coherent radar echoes called Polar Mesospheric Summer Echoes (PMSEs). Therefore, radar investigations offer the possibility to investigate the dust and its interactions.

Based on observations with the EISCAT VHF radar, this thesis deals with different radar methods and their possibilities to examine dust particles throughout the year, both looking at dust signatures in incoherent scatter signals as well as dust encased in ice in the cold summer mesosphere and its influence on PMSEs.

Examining dust signatures in incoherent scatter we have found that it is possible to derive dust size and number density information, as long as the electron density is sufficiently high to provide signals that allow for detailed analysis of the spectral shapes. However, this is often not the case, making long-term investigations of the D-region quite difficult. The emergence of the new EISCAT_3D radar with a higher transmit power compared to the present EISCAT radar used for our studies can improve observational studies, providing information on the intricacies of dust clouds. An existing model to describe the incoherent scatter in the presence of charged dust was extended, and a code was made public for future use to calculate the spectra including dust with a size distribution.

We studied PMSEs in combination with artificial heating of the ionospheric electrons at cyclic time intervals. We investigated observations during low solar illumination conditions around midnight in August, late in the PMSE season, which has never been done before. Many heating cycles at high altitude show quite large overshoots, where these do not agree with models that have been used previously to describe similar EISCAT studies during different solar illumination. We also often observe large differences in the PMSE power of consecutive heating cycles with rapid variations. The available results from these heating experiments do not allow systematic investigations of the dust charging properties without further development of existing charging models.

Acknowledgments

List of publications

This thesis consists of a subject introduction and the following papers, which will be referred to by their Roman numerals.

Paper I   **Gunnarsdottir, T. L.** and Mann, I.: Charged dust in the D-region incoherent scatter spectrum, Journal of Plasma Physics, doi: 10.1017/S0022377821000866 ,2021

Paper II   **Gunnarsdottir, T. L.**, Poggenpohl, A., Mann, I., Mahmoudian, A., Dalin, P., Haeggstroem, I. and Rietveld M.: Modulation of polar mesospheric summer echoes (PMSEs) with high-frequency heating during low solar illumination, Annales Geophysicae, doi: 10.5194/angeo-41-93-2023, 2023

Paper III   **Gunnarsdottir, T. L.**, Mann, I., Feng, W., Huyghebaert, D. R., Haeggstroem, I., Ogawa, Y., Saito, N., Nozawa, S. and Kawahara T. D. : Influence of Meteoric Smoke Particles on the Incoherent Scatter Measured with EISCAT VHF, Annales Geophysicae, *Preprint*, 2023

Contents

Chapter 1

Introduction

This thesis looks into meteoric dust particles in the upper Earth's atmosphere and different radar methods to detect them. It was first suggested by Rosinski and Snow (1961) in the 1960s that a certain type of dust particles could be found in the Earth's mesosphere that had their origin in outer space. These dust particles were believed to be a combination of ablated material from meteors or other cosmic dust compounds that are heated when they enter the atmosphere at high speed and some atmospheric molecules or compounds from the ablation altitudes. These particles are called Meteoric Smoke Particles (MSPs) and have sizes in the nanometer range at altitudes of 60-90 km.

The MSPs can collect or release electrons and, if the number density of charged MSPs is sufficiently high, they can start to influence the local charge balance that otherwise is given by the electrons and ions. Under conditions of the ionosphere, dust particles are typically negatively charged by electron attachment (Asmus et al., 2015; Baumann et al., 2013). This has been confirmed by rocket measurements that observe the so-called electron bite-out, a large depletion of electron density at altitudes where also dust particles are detected (Friedrich et al., 2011).

These dust particles are also believed to facilitate the growth of ice particles during summer, where the mesopause (around 85 km) is the coldest part of the atmosphere, with temperatures in the 150 K range (Lübken, 1999). Ice particles are observed in Noctilucent Clouds (NLC) (Vaste, 1993) from Earth, and they are observed from satellites, then called Polar Mesospheric Clouds, PMCs (Bardeen et al., 2010). And ice particles, through charge interactions, participate in a process that forms strong coherent radar echoes; Polar Mesospheric Summer Echoes (PMSE) (Rapp and Lübken, 2004). Charged dust particles can also influence a process called incoherent scatter, which is observed with high-power radars and is used to measure the parameters of the ionospheric plasma (Cho et al., 1998; Kudeki and Milla, 2010).

This thesis focuses on the use of various radar techniques to identify dust particles in the mesosphere through incoherent and coherent radar scatter observations. Chapter 2 describes the dust present in the upper atmosphere of the Earth. Chapter 3 discusses dust studies with observations of PMSE, which is coherent scatter, and modulation of the signal with artificial heating. The influence of charged dust on the incoherent scatter is discussed in Chapter 4, with a model description and analysis of a radar observation under suitable conditions. A summary of the presented work is given in Chapter 5.

The work on this dissertation project includes the preparation of three publications (Papers I to III). Chapter 3 describes the results of Paper II and Chapter 4 describes the results of Paper I and III. The author's contributions are described in each manuscript.

Chapter 2

Dust in Earths Atmosphere

Meteors ablate in the altitude region between 70 and 110 km (see Figure 2.1) depending on atmospheric pressure (Plane, 2012). This ablation occurs globally and recent estimates find a daily influx of 25 ± 7 tons per day (Hervig et al., 2012). The ablated material re-condenses to form dust particles called meteoric smoke particles (MSPs) (Rosinski and Snow, 1961) of nanometer size. They grow further and sediment down to lower altitudes (Hunten et al., 1980), influencing various processes along the way.
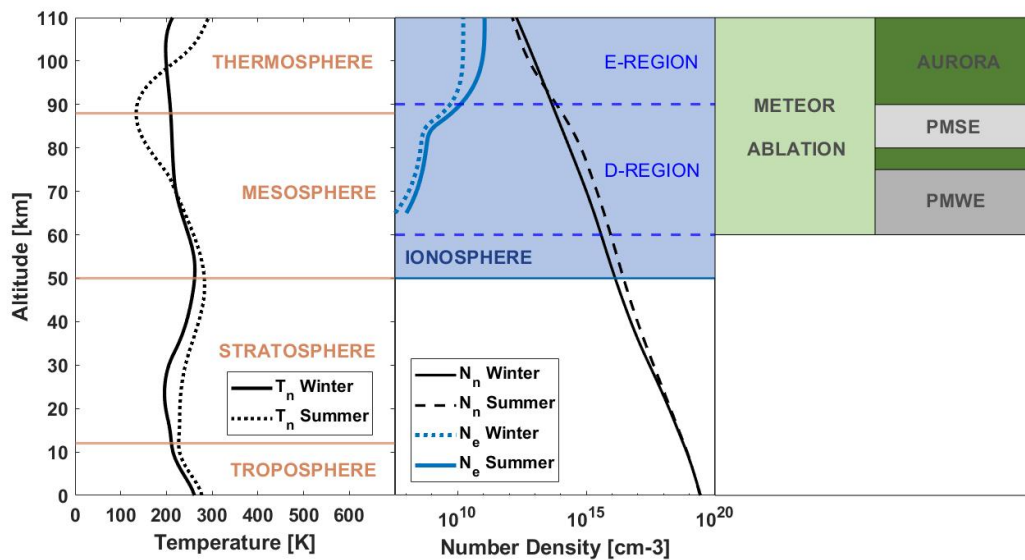

Figure 2.1: An overview of the approximate altitudes of the mesosphere and the D-region ionosphere. Examples of temperature, neutral density and electron density is shown for winter and summer conditions (Data is from 2019 from the nrlsmise-00 model (Hedin, 1991)).

The dust initially forms in the mesosphere and lower thermosphere, which overlap with part of the ionosphere, mainly in the D-region. Dust particles can be negatively or positively charged through various processes in the ionosphere, where electron attachment is assumed to be the most effective and therefore dust particles are often assumed to be negatively charged (Asmus et al., 2015; Baumann et al., 2013, 2015).

In the summer polar mesosphere the temperature can become extremely low as can be seen in Figure 2.1, low enough around the mesopause for ice to form on the dust particles by heterogeneous nucleation (Tanaka et al., 2021). These ice particles can often be seen around 80 km altitude as Noctilucent Clouds (NLC) during the summer season and detected by radar as Polar Mesospheric Summer Echoes (PMSE). Polar Mesospheric Winter Echoes (PMWEs) are echoes found at altitudes lower than PMSE and originally only thought to occur in winter. They have been attributed to the occurrence of MSPs, but recent rocket measurements have shown that PMWEs can be explained without the presence of MSPs (Strelnikov et al., 2021).
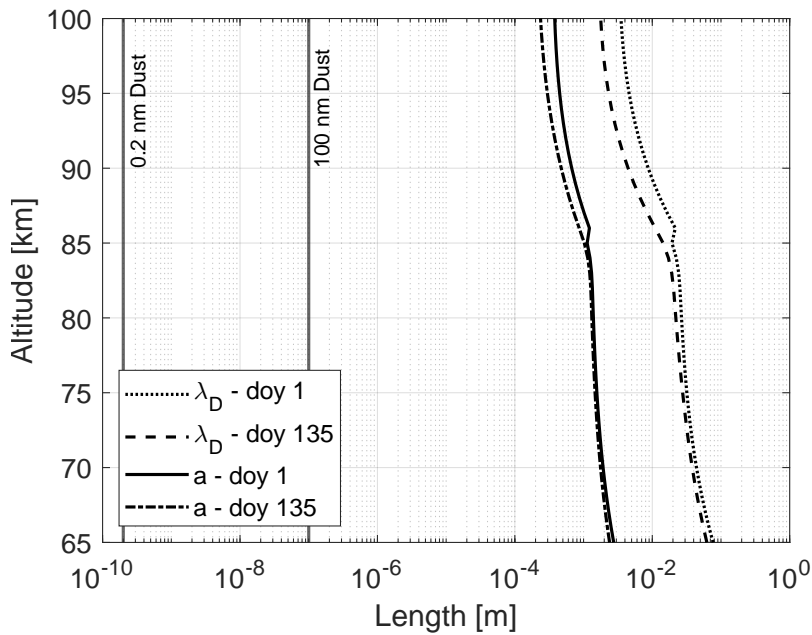
Figure 2.2: Example of a dusty plasma condition, showing two dust sizes, mean length between particles a and plasma Debye length λ_D. Figure from paper I.

Observations of MSPs are quite difficult due to their small size. Some success has been made in detecting them in-situ with instruments on sounding rockets that have examined the dust charge, composition, and possible size ranges (Antonsen et al., 2017; Havnes et al., 2001; Rapp et al., 2010, 2012; Schulte and Arnold, 1992). However, these measurements are not without problems; the smallest particles are often deflected in the air stream around the rocket, as well as dusty ice particles, creating secondary charging effects when they hit the detector (Antonsen, 2019). Recent advances have been made in satellite observations of dust, where possible compositions can be inferred from solar

occultation measurements (Hervig et al., 2012).

These observations have also made estimates of the total input of meteoric material per day (mentioned above). Currently, human-made material input into the atmosphere is only estimated to be a few percent of the total input; this, however, is predicted to change in the coming years, with future predictions being in the range of 15-40 % (Schulz and Glassmeier, 2021). Man-made space debris often contains metals comparable to those of meteoric input material, for example iron (Plane et al., 2015). Therefore, it will be necessary to develop methods for the detection and investigation of dust particles in the D-region/mesospehre to determine the changes that space debris might bring to this region of the atmosphere.

From the ground, the ionosphere can be studied with high-power, large aperture radar by observing a process denoted as incoherent scatter. Incoherent scatter arises because the electromagnetic radar waves are scattered by the electrons, and the wave interaction with other charged components in the ionosphere determines the shape of the spectrum. It is likely that the dust influences incoherent radar scatter when the dusty plasma condition is met, that is, the dust takes part in plasma processes. A measure of dusty plasma conditions is that the dust size is much smaller compared to the distance between plasma particles,a, which in turn is smaller than the Debye length λ_D. Figure 2.2 shows that for typical electron densities the dusty plasma conditions hold in the mesosphere for all dust sizes in the range of 0.2 - 100 nm. Here, a is approximated by $a \propto N_e^{-1/3}$.

Chapter 3

Polar Mesospheric Summer Echoes during HF Heating

A summary of the topic and results from Paper II is given here. We studied the variation of Polar Mesospheric Summer Echoes (PMSEs) observed with the EISCAT VHF radar during artificial heating experiments in which the electron temperature at the PMSE altitude is artificially enhanced. Modulation of the electron temperature with the heating experiments leads to characteristic variations of the PMSE signal that, among others, depend on the dust charging and the size of the particles. Many observations have been made with EISCAT on PMSE echoes with heating during the summer season. The work presented here is the first to focus on observations during late summer at night, where solar illumination is low and hence has less influence on the charging process.

Polar Mesospheric Summer Echoes

Polar Mesospheric Summer Echoes are strong coherent radar echoes that typically form between 80 and 90 km altitude and are most often seen with radar in the polar summer mesosphere, associated with low mesopause temperature minima in summer. These cold temperatures cause ice particles to form and grow up to tens of nanometers in size, and it is believed that these ice particles play a role in the formation of PMSE. PMSE can be measured with radar frequencies ranging from 50 MHz to 1.3 GHz. For an overview of PMSE observations and formation models, the reader is referred to publications by Rapp and Lübken (2004) and Röttger et al. (1988).

Coherent radar echoes are usually observed in the mesosphere when radio waves are reflected by strong fluctuations in the electron density, as these change the refractive index. Scattered radio waves interfere constructively when the distance between the scattering centers is half the radar wavelength. This is called the Bragg condition and causes strong reflected echoes. Such coherent echoes due to scattering at the Bragg condition are typically caused by neutral turbulence in the atmosphere but only at smaller frequencies, hence larger wavelength. This is because electron diffusion smooths out the electron density fluctuations on the smaller spatial scales. It is assumed that the

presence of charged ice particles influences the electron distribution in such a way that even smaller spatial structures can persist for some time and cause PMSE signals to be observed at higher frequencies (Mahmoudian et al., 2017; Rapp and Lübken, 2004). The spatial distribution of the ice particles at these altitudes is influenced by the complex neutral atmosphere, and thus, for example, turbulence in the atmosphere leads to the spatial structures of the ice particles. The ice particles influence the distribution of electrons by becoming charged, where they bind to free electrons. And these strong radar echoes form when the wavelengths of these spatial distributions are half of the radar wavelength, $\lambda_R = 2 * \lambda_{irreg}$.

The ice particles affect the radar signals because their charge affects the distribution of the electrons. Therefore, a brief consideration of charging is included here (e.g. Rapp et al. (2007a,b)). The ice particles collect electrons and ions from the surrounding ionosphere. Incident photons (mainly from the Sun) can cause photoionization or remove surface electrons (photodetachment). The different charging currents associated with these processes depend on the electron, ion and photon fluxes as well as on the charge, i.e. the electrical surface potential of the ice particle. After some time, a particle reaches a surface potential at which the different currents cancel out to zero. Under normal conditions, electrons and ions have similar temperatures in the D-region ionosphere, and because the electrons are less massive, they generate a charging current higher than that of the ions, causing the ice particle to become negatively charged. The charging processes depend on the material-dependent properties of photodetachment and photoionization, particle sizes, and ion and electron fluxes. The latter component can be systematically changed in artificial heating experiments as discussed below.

Heating

Chilson et al. (2000) showed for the first time that PMSE signals are modulated during artificial heating of ionospheric electrons with high-frequency (HF) radio waves. The EISCAT Heating facility generates HF heating and can operate simultaneously with the EISCAT VHF radar (Rietveld et al., 1993). The electrons in the radar volume are instantaneously heated and their temperature can reach 2000 K (Kassa et al., 2005; a detailed investigation of electron temperatures at PMSE altitudes during the EISCAT Heating experiments was recently carried out by Myrvang et al. (2021) and the reader is referred to this work. An example of PMSE measured with the EISCAT VHF radar along with artificial heating is shown in Figure 3.1. During the observation, the heater was turned on and off at time intervals of 48 seconds and 168 seconds, respectively. This cyclic heating causes the PMSE signal to reduce as the heater is turned on and increase again after the heater is turned off. This modulation of the PMSE signal is also sometimes called the Overshoot Characteristic Curve (Havnes, 2004), where the PMSE signal has increased to a higher value after heating than before the heater was turned on. Observing PMSE echoes along with heating should allow us to infer dust information from the observed overshoot curves.
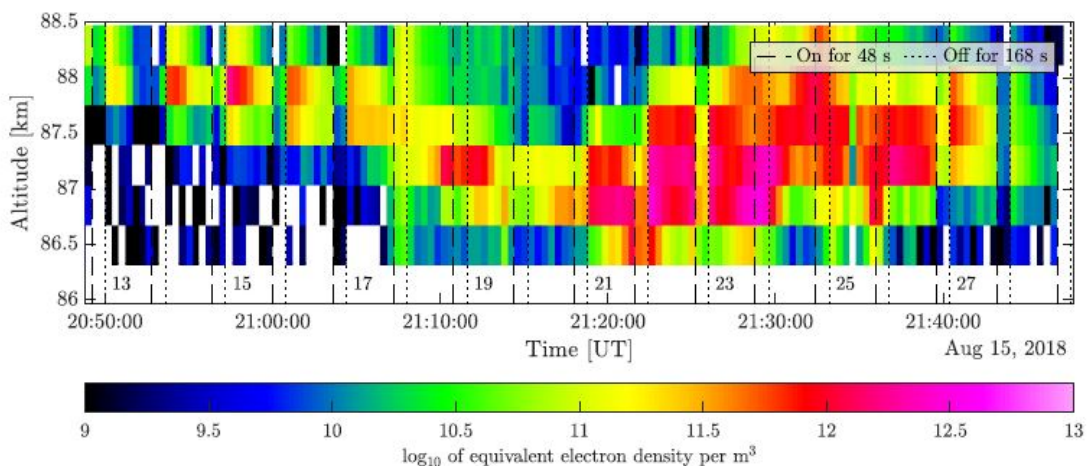
Figure 3.1: Example of an observation with the EISCAT VHF radar of a PMSE radar echo layer that has been heated with the EISCAT heating facility in time sequence 48 seconds on and 168 seconds off. Figure from Paper II.

Clear cases of overshoot curves can be seen in Figure 3.1, for example, in heating intervals 14, 15, 16 around 88 km altitude. The general shape of this overshoot curve can be seen in Figure 3.2. The time the heater is turned on and off and the corresponding decrease or increase of the overshoot curve are marked in the figure. The PMSE variation follows the following phases: an instantaneous decrease when the heater is turned off, a lower signal during the heating phase, and rapid recovery when the heating is turned off. Sometimes the signal is higher than at the beginning of the cycles, which is called an overshoot. Such an overshoot is followed by relaxation, during which the signal returns to the previous undisturbed level.
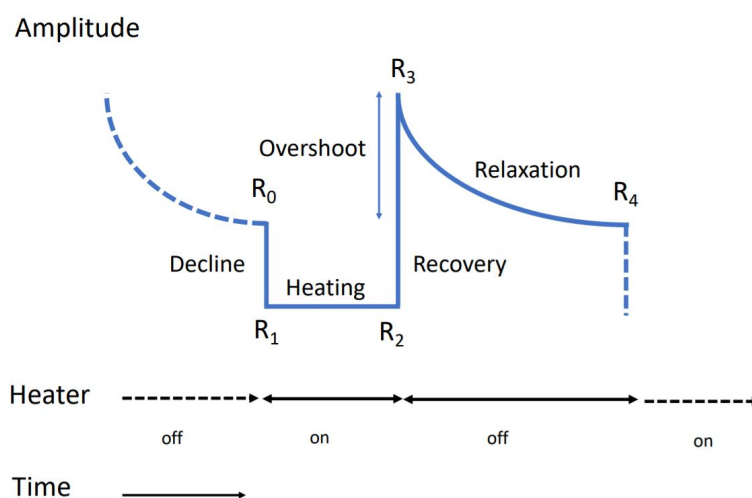
Figure 3.2: Typical shape of an Overshoot Characteristic Curve. Figure from Paper II.

The overshoot behavior can be explained qualitatively: When the heating is switched on, because of the higher temperature, the electron diffusivity is higher and the electron density gradients are smoothed; therefore, the backscatter is less efficient (Havnes, 2004). In addition, the electrons collide more frequently with dust particles and accumulate quickly on the surfaces of nearby large dust particles, causing a decrease in free electrons. The latter effect depends on the charging process, i.e. on the size of the dust particles. When the heater is turned off again, the electron temperature quickly drops to the initial value. However, the dust particles still carry a higher charge than before. As a result, the electron density gradients are larger than before the heater was turned on and therefore the backscatter is higher. The relative contribution of the ion current is larger than that of the equilibrium charge; therefore, the dust charge decreases on the time scale of the ion current and during this process the PMSE power goes back to the initial value of unheated conditions.

The effects of the heating disappear during conditions with high ionization, i.e. high electron density. This can be seen in Figure 3.1, where during heating cycle 18 the electron density is high and no overshoot can be observed; this effect is also seen in cycle 19 where the electron density is still rather high. One can assume that the total electron content in the PMSE layer is so high that the electron density variations caused by the modified dust charging are small in comparison. In addition, much of the HF heating wave may be absorbed below the PMSE layer if the electron density is also high there.

Heating experiments and VHF observations

Four observation campaigns were conducted to study PMSE with EISCAT VHF and artificial heating during dusk conditions with low solar illumination. Two observations were made in 2018, on 11 and 15 August, and two in 2020, on 5 and 6 August. During all four observations, PMSE were observed at several altitudes, always between 80-90 km. The 5 August 2020 observation from 20:30 UT to midnight UT is shown in Figure 3.3. Similar figures are provided for the other observations in Paper II. The figure shows the electron densities derived from the EISCAT VHF analysis as a function of time and altitude; the PMSE layer is seen as strong signals forming horizontal structures. The ionization is at times very high, as can be seen from the high electron densities. The common background ionization is caused by solar illumination, primarily from the Lyman alpha hydrogen line of the solar spectrum. The main source of enhanced ionization above the PMSE is at altitudes below 100 km from energetic particle precipitation (Mironova et al., 2015).

Figure 3.3 shows high electron densities presumably due to particle precipitation at PMSE altitudes between roughly 20:45 UT and 21:30 UT. However, the data collected prior to the first layer marked as Area 1 is not used to some artifact in the measured data. From 21:30 UT the ionosphere at altitudes is unaffected or only slightly affected by particle precipitation. This includes the areas marked with 1 and 2 that we consider for analysis. Similarly, several

observational areas were selected for the other observation days. Area 3 in Figure 3.3 is not PMSE, but is a sporadic E-layer and is not included in the data analysis.
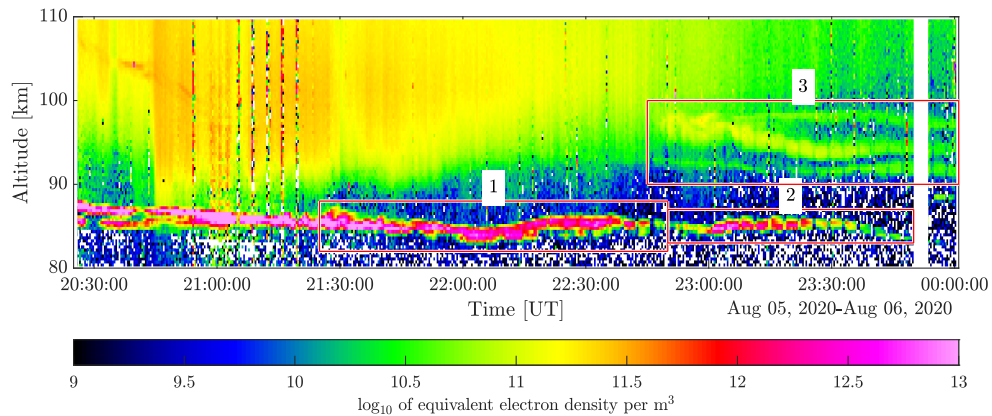
Figure 3.3: Observation with EISCAT VHF along with artificial heating cycles, from 5 August 2020. Figure from Paper II

The observational times are all around local midnight, and it is helpful to consider the solar illumination at the time of the observations. The solar zenith angle for the observations was in the range of 88-97 degrees, and thus most of the radar volumes observed are in reduced sunlight; some have no direct sunlight. Figure 3.4 shows an example of the photon flux that the author estimated for two points in time during the 15.08. 2018 observations (at 22:00 UT and 24:00 UT); the flux for high summer conditions at noon is shown for comparison. As can be seen, the photon flux in the Lyman α line is greatly reduced by one and two orders of magnitude compared to noon/high summer conditions, when the EISCAT studies of PMSE are usually made.
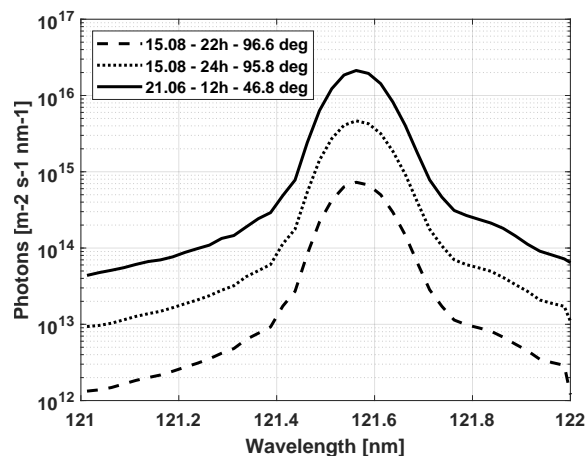
Figure 3.4: Photon flux around the Lyman-α line for three different times at 85 km. Figure from Paper II.

Data analysis method - quantifying overshoots

As mentioned in a previous chapter, an overshoot can occur when heating PMSE echoes in a certain on/off time sequence. The observations are investigated in detail in Paper II, but a brief overview is given here. In each of the four observations, three intervals were identified with layers visibly influenced by heating because the radar signal drops when the heater is on. Two of these layers were identified as sporadic E-layers and not PMSE echoes. This was obvious because of their high altitude and low return power (compared to the usual PMSE power) and no visible overshoots. These layers are mentioned here for comparison, but they were not included in the data analysis.
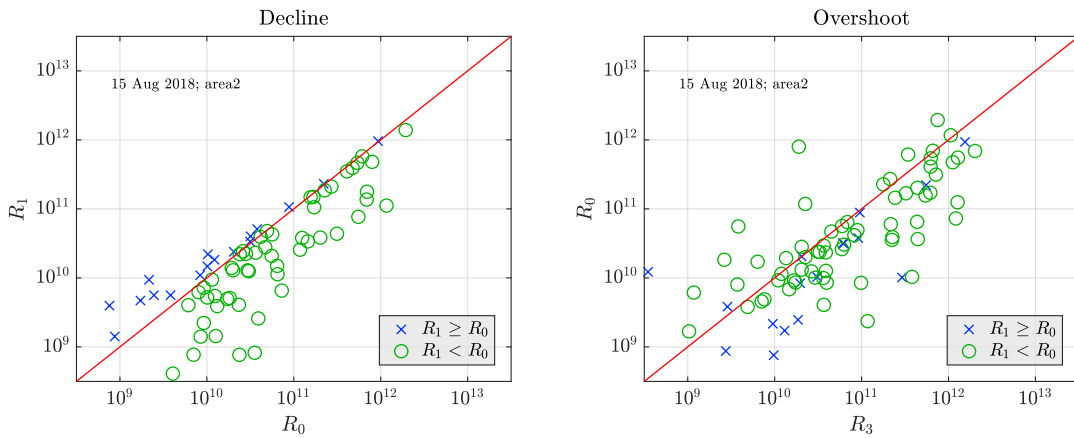
Figure 3.5: Scatter plots of the decline ratios R_0/R_1 and heating ratios R_0/R_3 for area 2 in observation on 15 August 2018. Figures from Paper II.
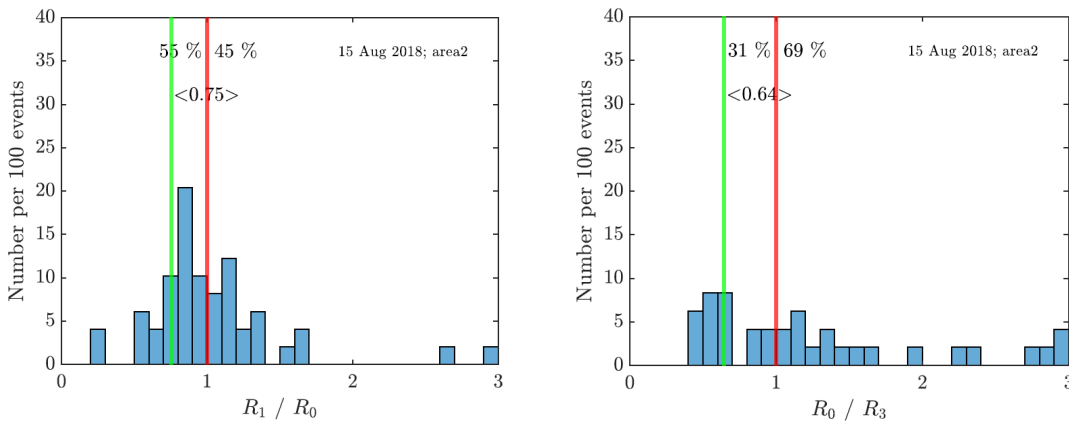
Figure 3.6: Histograms of the decline and overshoot ratios derived in the area 2 of the 15 August 2018 observations. Histograms are only plotted for cycles affected by heating. Green line represents the average of all overshoot ratios. Figures from Paper II.

Overshoots have previously been investigated by several authors, who also used EISCAT VHF and heating and similar heating cycles (Havnes et al., 2014; Pinedo et al., 2014; Ullah et al., 2019). A first view of the discussed observations showed that some of the overshoots are very high in comparison to previous investigations. For a quantitative description, for each heating cycle we determined the amplitudes R_0, R_1, R_2, R_3, and R_4. These are marked in Figure 3.2, where R_0 is the signal amplitude before the heater is turned on, R_1 is the amplitude observed when the heater is turned on, R_2 is the last amplitude observed during the heating cycle, R_3 is the amplitude after the heater is turned off, and R_4 is the amplitude observed before the beginning of the next heating cycle.

Figure 3.5 on the left compares R_0 and R_1 where R_1 being smaller than R_0 indicates that PMSE is influenced by heating in the predicted way. Here, we plotted the amplitudes for all observed cycles in the PMSE layer considered; the green circles mark cycles that show an effect of the heater and the crosses mark observations where switching on the heater had no visible effect.

The right-hand side of the figure shows the ratio of the amplitudes R_0 and R_3 of all the cycles in this area. The symbols used are the same as on the left: green circles mark the cycles that are affected by the heater. They are spread around the red line rather evenly, indicating equal amounts of reduced and increased values after the heater was turned off. Therefore, overshoots and undershoots are about equally abundant (where the overshoot ratio R_0/R_3 is 1). Inspection of the observations shows that the parts of the PMSE that are not affected by heating are in regions where the influence of particle precipitation is also recognizable.

In figure 3.6 the ratio of the decline is shown on the left and the ratio of the overshoot on the right. This only includes the cycles that were affected by heating (that is R_0/R_1 is below 1, the values below the diagonal on the left-hand side of Figure 3.5). One can see that 55 % of the cycles that are affected by heating show a decrease in power when the heater is turned on. The mean of the decline ratio is R_1/R_0 is 0.75, which means that the power reduces by approximately 25 % on average when the heater is turned on.

In the right panel of figure 3.6 the overshoot ratio is shown for all cycles. Only 31 % of them show an overshoot with a mean value of 0.64. That is, on average, the power increases by 46 % for these cycles. This method was used for each of the measurement areas of the four observations. The results are summarized in Table 3.1, together with the ratios for heating (R_1/R_2), recovery (R_2/R_3) and relaxation ($R_4/R3$). For reference, Figure 3.2 is given again below to accompany the table.
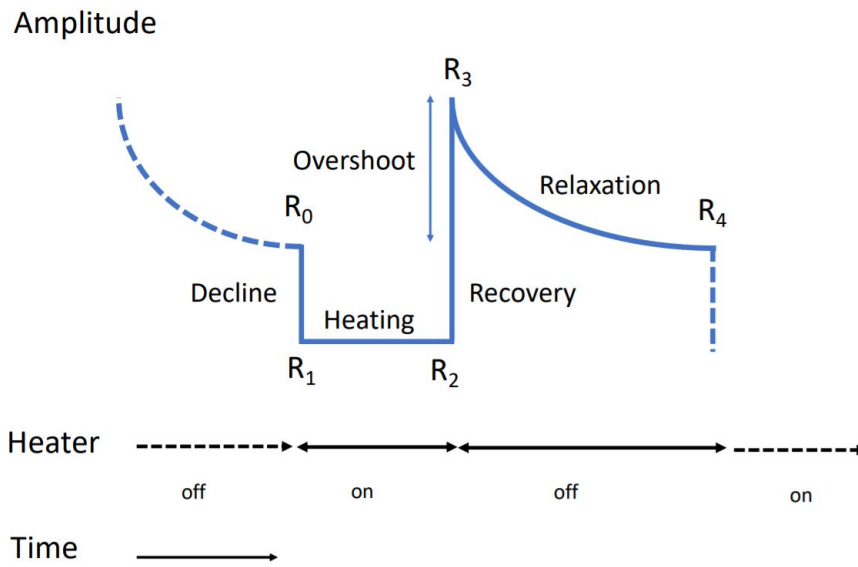
Figure 3.7: Showing the overshoot shape which is often seen when heating PMSE in an on/off sequence. Figure from Paper II. The figure is included here again for comparison purposes with Table 3.1.

Table 3.1: Summary of histogram results for the decline, overshoot, heating, recovery and relaxation ratio when they are smaller than 1 (indicating heating effect and overshoot) for all four observations. These numbers only include observations with the minimum background amplitude $R_0 > 10^{10.5}$. A1 refers to area 1 for that observations date, and so forth. Gray rows mark sporadic E-layers and not PMSE with heating.

| | | Decline | | Overshoot | | Heating | | Recovery | | Relaxation | |
| | | $R_1/R_0 < 1$ | | $R_0/R_3 < 1$ | | $R_1/R_2 < 1$ | | $R_2/R_3 < 1$ | | $R_4/R_3 < 1$ | |
		Mean	%	Mean	%	Mean	%	Mean	%	Mean	%
11.8.18	A1	0.76	58	0.56	45	0.76	56	0.69	51	0.49	63
	A2	0.75	61	0.57	51	0.71	50	0.73	56	0.42	63
	A3	0.77	55	0.61	50	0.74	43	0.72	66	0.50	61
15.8.18	A1	0.74	100	-	-	0	0	0.60	100	0.20	100
	A2	0.75	55	0.64	31	0.77	24	0.72	58	0.41	42
	A3	0.69	63	0.41	40	0.68	43	0.61	46	0.36	64
5.8.20	A1	0.72	46	0.48	44	0.66	32	0.66	66	0.42	61
	A2	0.72	55	0.44	10	0.76	5	0.75	66	0.78	13
	A3	0.75	66	0.87	17	0.83	21	0.83	51	0.81	30
6.8.20	A1	0.74	59	0.54	53	0.73	40	0.66	78	0.42	59
	A2	0.90	61	0.89	10	0.90	14	0.87	54	0.79	34
	A3	0.52	83	0.24	17	0.76	20	0.34	40	0.40	100

From Table 3.1 one can see that for most of the observed areas, overshoots are observed in almost half of the heating cycles. Here, the average increase in PMSE power lies in the 40-60 % range. Here we see that even though we have seen quite high individual overshoots, on average the layer shows approximately a doubling in the PMSE power when the heater is turned on. The heating ratio shows that, in general, power decreases during the heating period for most areas with a mean decrease of about 25-30 %. The relaxation ratio shows how the subsequent heating cycles relate to each other. Where this ratio is expected to be below 1 to indicate that the PMSE power is decreasing after the overshoot increase. Here we can see that most areas show more than 60 % of the cycles below 1 with a mean value of about half or less. For those cycles that show an increase in values after the overshoot, might indicate a cycle being influenced by particle precipitation or a general increase in PMSE power in the layer.

Comparing selected heating cycles to overshoot models

Several models have been developed to calculate the overshoot curves (Havnes, 2004; Mahmoudian et al., 2011) and have been used together with observations to derive the average dust sizes and the relative dust number density distribution producing the PMSE echoes. Since the observations analyzed in this work were the first during dusk conditions, it is interesting to compare them with such models.
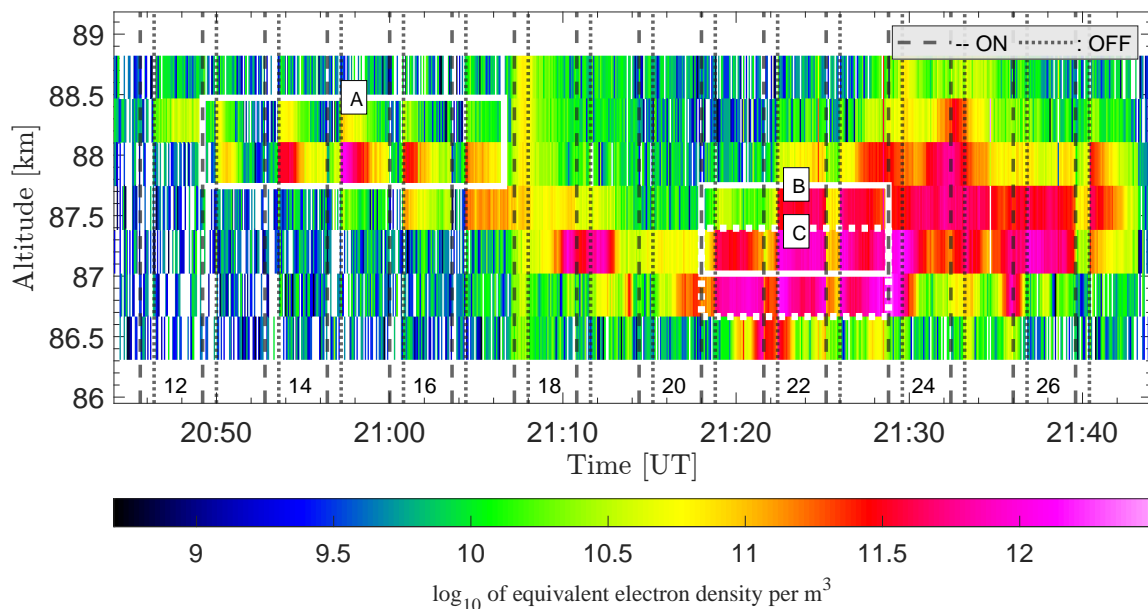

Figure 3.8: Area 2 from observation from 15 August 2018. Marked in the figure are the 3 intervals, A, B and C, that we compared with simulated overshoots. From Paper II.

For this comparison, we identified three intervals from the observation of August 15, 2018, as shown in Figure 3.8. We selected an interval around 88 km altitude with weak PMSE and two intervals with stronger PMSE at altitudes between 86.5 km and 87.5 km. Particle precipitation was observed in a few cycles in between these intervals. The calculation of the modeled overshoot curve was made by Alireza Mahmudian, an expert in the field, see. e.g Mahmoudian et al. (2011); Scales and Mahmoudian (2016) for more information on the model. To take into account the twilight conditions, the dust photoionization rate in the model was reduced by a factor of 10 for the model calculations. The results are summarized in Tables 3.2 and 3.3. Interval A showed very large individual overshoots, and after averaging all cycles in that interval together and normalizing to the preheater value, resulting in an overshoot of almost 9.85; denoted as NormMAX in the table. For the other two intervals, the overshoots had average values of 2.36 and 3.07, respectively. Comparison with simulations showed that for the first interval (A), an 8-fold increase in electron temperature during heating was required to produce an overshoot of 8.35. This is still lower than the average value from the observations. The model calculation could not produce such high overshoots even when accounting for the reduced solar illumination. For the other two intervals, the amplitude of the overshoot was well reproduced with a heating temperature increase by a factor of 5. All simulations showed a 3 nm dust size that fitted best to the observations and 35 % dust number density (compared to the electron density) for interval A and 60 % and 68 % dust number density required for the other two intervals respectively.

Table 3.2: Normalized values of the overshoot shown for the observation and simulation for each of the intervals. Also shown are other parameters from the simulation.

	Observation	Simulation			
Interval	Norm_{MAX}	Norm_{MAX}	T_e/T_i	$r_d[nm]$	n_d/n_e
A	9.85	8.35	8	3	35 %
B	3.07	3.06	5	3	60 %
C	2.36	2.3	5	3	68 %

The differences between the overshoot curves in interval A and the model calculations indicate that either the model assumptions on PMSE, or those on the dust charging, or both are not sufficient. In previous studies that validated the model calculations, the authors compared the models to overshoot curves averaged over multiple heating cycles. For the observations presented in this work, this approach is not meaningful, as it significantly reduces the overshoots compared to the individual curves. The number of very high overshoots in the observations presented here is not negligible, and one can conclude that current overshoot models cannot replicate overshoots for dusk con-

ditions. Unfortunately, the model proposed by Havnes was not available for calculations, but a comparison with published calculations also shows that the overshoots calculated with that model are lower than those in our observations.

Table 3.3: Normalized values of the overshoot shown for the observation and simulation for each of the intervals. Also shown are other parameters from the simulation.

Interval	$Z_{dave,max}$	τ_{diff}/τ_{ch}		N_n	ν_{in}
		ON	OFF		
A	1.38	0.13	0.014	1.19×10^{20}	3.44×10^4
B	0.9	0.093	0.0076	1.33×10^{20}	3.85×10^4
C	0.86	0.08	0.0062	1.48×10^{20}	4.26×10^4

The parameters used in the model calculations provide insight into the discussion of possible explanations for the overshoot. Table 3.3 shows the average charge number, $Z_{dave,max}$, for each model calculation along with the ratio, τ_{diff}/τ_{ch}, of the diffusion and dust charging timescales. Included also are the neutral density and the estimated ion-neutral collision frequency (using values from nrlmise-00). Here, we can see that the average charge number needed to produce such a large overshoot in interval A is quite high,indicating a multiple charge for a fraction of the particles at least. In general, the models show higher overshoots for larger dust charges. The other two observation intervals show an average charge number smaller than 1, as is expected for charging of dust in the size range of few nm. The ratio of timescales indicates that there are different diffusion and charging timescales for these cases, where these two timescales are competing when the heater is turned on and off (Mahmoudian et al., 2011). The decrease in the ion-neutral collision frequency with altitude (as can be seen in Table 3.3) may be a factor in the increase of the timescale ratio and the large overshoots seen at higher altitudes.

Chapter 4

Dust Influence on the Incoherent Scatter Spectrum

A summary of Papers I and III is given here together with a short introduction to relevant topics. The papers investigate the influence of charged dust on the incoherent scatter spectrum based on model calculations and on EISCAT VHF observations.

First, an introduction is given to the incoherent scatter equation used in the model calculation and how it depends on the dust parameters. The model is extended, and it is used to discuss under what conditions the dust noticeably influences the electrons and, consequently, the measured spectrum. An overview of the possible influence of the dust and other parameters on the spectrum is given and how this influence varies over a year. On the basis of this, optimal conditions are derived to identify a suitable EISCAT observation for analysis. We find such an observation during winter and with an increased electron density down to almost 60 km. The observation is compared with the incoherent scatter spectrum model with a dust component, and the dust number density and dust sizes needed to replicate the observation are determined.

Radar Equation and electron backscatter

Incoherent scatter radars send electromagnetic waves up into the upper atmosphere where they cause the free electrons to oscillate and scatter back a very small part of the incoming wave. The radar receives the radiated power from the electrons in the radar volume. This allows one to infer some information on the electrons; however, they are coupled to the ions in the volume. Therefore, the measured scattering from the electrons also contains information on the ions and can be used to infer several plasma parameters like electron density, electron and ion temperature, and ion velocities.

Starting with the radar equation for a monostatic radar system, we can use the equation below to calculate the power scattered and received by the antenna. The received power P_R is:

$$P_R = P_T \frac{G^2 \lambda_R^2 \sigma_N}{(4\pi)^3 R^4 L} \tag{4.1}$$

where P_T is the transmitted power, G is the gain of the antenna and depends on the radar being used, R is the range from the radar to the target, L are any losses, and λ_R is the radar wavelength. σ_N represent the backscatter received from all electrons in the radar volume. If enough charged dust particles are present in the radar volume, the dust will influence the σ_N factor.

Expanding the backscatter equation to include charged dust

Cho et al. (1998) proposed an adaption of the radar backscatter equation for 3 fluids (see, e.g. Mathews (1978); Tanenbaum (1968)) to include an N-fluid description, which allows us to include any number of dust particles of different sizes, as well as positive and negative ions. For this model, the authors assumed that the particles were singly charged. The equation developed by Cho et al. (1998) where dust is included in the incoherent scatter spectrum is given here. The derivation and explanation of this equation can be found in Paper I and is not repeated here except for a short summary. The backscatter equation, including dust particles, is as follows:

$$\sigma_b(\omega_0 + \omega)d\omega = \frac{r_e^2 N_e d\omega}{\pi \omega} \left| \frac{1}{\alpha_e^2 + z_e \left(1 + \sum_{s \neq e} Z_s^2 \frac{\alpha_s^2}{z_s^*}\right)} \right|^2 \tag{4.2}$$

$$\times Im \left(\left| 1 + \sum_{s \neq e} Z_s^2 \frac{\alpha_s^2}{z_s} \right|^2 z_e + \frac{\alpha_e^2}{T_e} \sum_{s \neq e} Z_s^2 T_s \frac{\alpha_s^2}{z_s^*} \right)$$

Here, the terms marked in red (α_s^2, z_s, and T_s) describe the contribution of the dust to the backscatter equation. These terms include the number density and dust mass for each size bin. The mass of the dust particles is calculated by assuming spherical particles and a bulk mass of 2-3 g/cm3 (this number depends on assumptions of the dust material). Here, we have included the charge number Z_s^2, where Cho et al. (1998) has chosen to set it as $Z_s^2 = 1$, which is often assumed to be valid for particles smaller than 10 nm. Note that everywhere the charge number is squared, and thus the addition of dust does not depend on the sign of the charge, except in the assumption of charge neutrality. Cho et al. (1998) assumed that the terms Z_s^2=1 (dust charge number) because particles <10 nm are typically singly charged. We include this term, and this approach is applicable to small multiple dust charges. However, note that assuming the same charge number for each included size bin reduces the

computation effort. In the case of high charge numbers, image charge effects should also play a role.
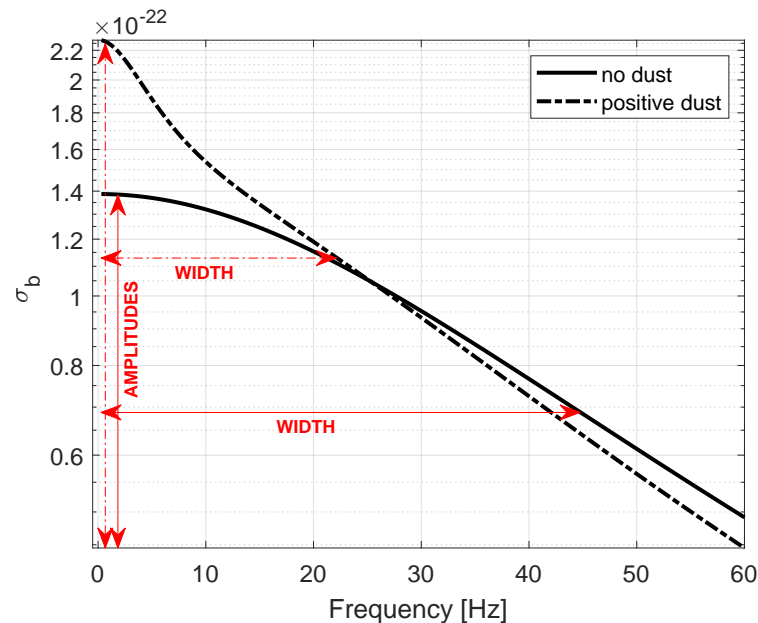

Figure 4.1: Example spectrum without a dust component and one with a positive dust component. Marked in red, are the width and the amplitude of the spectrum. Frequency axis is the angular frequency. Figure from Paper I.

Figure 4.1 shows an example of the central part of the incoherent scatter spectrum, this is usually denoted as the ion line, where the influence of the dust can be noticed. The figure shows a spectrum without dust (solid line) and a spectrum with an added positive dust component (dash-dotted line). The inclusion of a positive dust component creates a peak at the top of the normal background spectrum, and consequently narrows the spectral width. The red lines in the figure show the amplitude and width of each modeled spectrum. Therefore, if the presence of charged dust is large enough, it should be possible to discern, from a measured spectrum, whether there is dust present. The dust influence on the plasma should thus be possible to detect in this altitude region with an incoherent scatter radar. However, the effect that the dust has on the plasma is dependent on their size. Small dust particles behave similarly to negative ions, causing an acceleration in the electron diffusion rate and thus a broadening of the measured radar spectrum, whereas for larger dust particles, they should decrease the electron diffusion and thus cause the measured spectrum to be narrower than if only positive ions were present (Rapp et al., 2007a).

This picture is further complicated by the fact that the neutral density is rather high in the D-region, and thus the collisions between the neutral atmosphere with the plasma and dust will be a dominant factor over charged-component collisions. Different atmospheric temperatures, ion composition, and neutral composition might further complicate things. It has previously been shown by Hansen et al. (1991) that the measured radar spectrum from the D-region was

30% narrower than what theory predicts with only ions present; however, they did not examine the possibility that this was caused by dust. Another limiting factor is the amount of electron density; we need at least $N_e > 1e9 \ m^{-3}$ for a good enough radar signal in the D-region (60-90 km). This is often not the case, and only measurements with an enhanced ionosphere can be applicable for incoherent radar studies of dust with the current radar systems available.

4.1   Different influences on the incoherent scatter spectrum

Summary of variables that can influence the spectrum

The plasma in the D-region/mesosphere is collisionally dominated and weakly ionized, thus the measured incoherent scatter spectrum from these altitude regions depends on many different coupled parameters. Each parameter influences the measured spectrum to a different degree, so adding a dust component to an already complicated model is a challenge. Several authors have shown that there should be a dust presence in the D-region and that it influences the radar spectrum measured there (Rapp et al., 2007a; Strelnikova et al., 2007). To accurately determine dust parameters, the other parameters influencing the spectrum need to be understood and quantified.
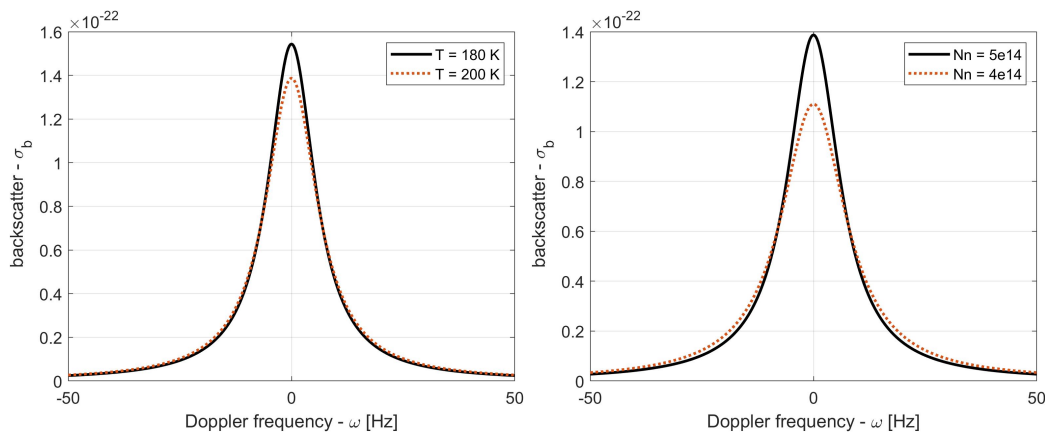

Figure 4.2: Left panel shows spectrum calculations for two different temperatures, T=180 K in black and T=200 K in red. The right panel shows spectrum calculations for two different neutral number densities, $N_n = \times 10^1 4 \ cm^{-3}$ in black and $N_n = 4 \times 10^1 4 \ cm^{-3}$ in red.

Here we have tried to quantify these differences by comparing the amplitude and width of the spectrum for different parameter ranges usually seen in this altitude region. An example spectrum with two different temperatures is given in the left panel of Figure 4.2, here the decrease in temperature from 200 K to 180 K causes a more narrow spectrum with higher amplitude, with a change in spectral width of about 2.3 Hz for this temperature change. On the right in figure 4.2 an increase in neutral density will cause a narrowing of the spectrum

with a change of 3.5 Hz for the spectral width in this particular case. This is summarized in Table 4.1.

Table 4.1: A few examples of different variables and how they influence the spectrum and whether they causes a broadening or a narrowing. The range of the dust size change shown is approximately 5 Hz change for positive dust and 4.5 Hz change for negative dust. Dust mass density change is at a maximum of 0.5 Hz where this is seen for the smallest particles (≈ 0.2 nm).

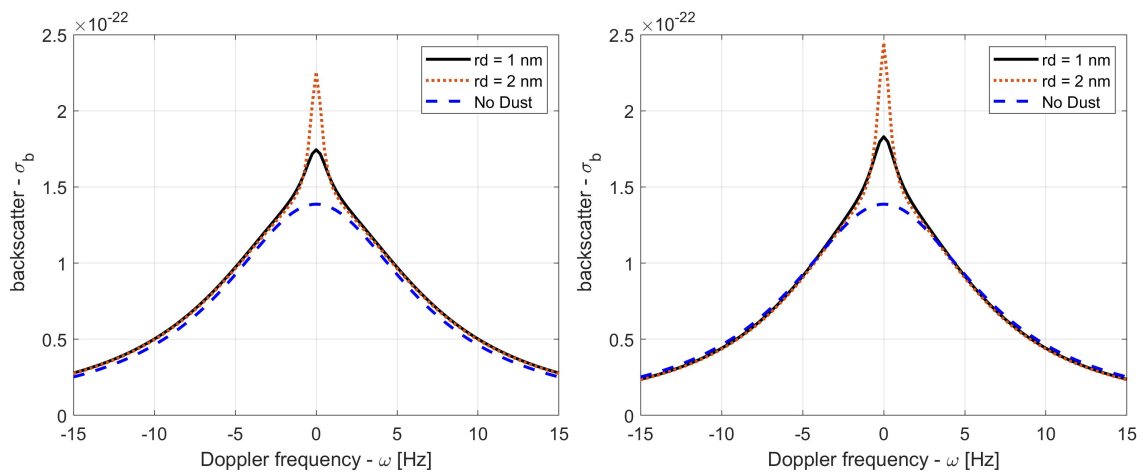| **Variables**	**Change**	**$\triangle$ Width**	**Effect**
Temperature	180 $\rightarrow$ 200 K	$\approx$ + 2.3 Hz	increase in T $\Rightarrow$ Broadening
Neutral Density	4e14 $\rightarrow$ 5e14	$\approx$ - 3.5 Hz	increase in N $\Rightarrow$ Narrowing (<95 km)
Dust size	1$\rightarrow$1.5 nm	$\approx$ -4.5-5 Hz	increase in r $\Rightarrow$ Narrowing ($r_d > 0.5$ nm)
Dust mass density	1$\rightarrow$9 g/cm^3	$\approx$- 0.5 Hz	increase in $\rho \Rightarrow$ Narrowing, ($r_d < 0.5$ nm)
Ion mass	31 $\rightarrow$ 51 amu	$\approx$ - 1.6 Hz	increase in $M_i \Rightarrow$ Narrowing ($r_d < 0.5$ nm)

Figure 4.3: Left panel compares negative dust of sizes r_d = 1 nm (black line), r_d = 2 nm (red dotted line), and no dust (blue dashed line). The right panel shows the same except the dust is positively charged.

When enough of large dust particles in the D-region are charged, they should influence the spectrum by introducing a peak on top of the normal background spectrum, and in that way make the spectral width narrower. An example spectrum is shown in Figure 4.3 with a 500 cm-3 negative dust component of two different sizes on the left and a positive dust component on the right with the same number density and dust sizes. Here we can see that larger dust sizes make the spectrum narrower and that positive dust particles will cause a more narrow spectrum. Here the electron density is 5000 cm-3 and the ion density is varied to keep charge neutrality.

This essentially means that a smaller amount of positive dust is needed to narrow the spectrum compared to a negative dust population. As shown in Table

4.1, by changing the dust size from 1 nm to 1.5 nm, you get a narrowing of 4.5 Hz for negative dust and 5 Hz for positive dust. The introduction of small negative (<0.5 nm) dust will broaden the spectrum and small positive dust will narrow the spectrum; this is due to the influence of dust on the electron diffusion rate, where the small negative dust particles behave more like negative ions (Rapp et al., 2007a).

Variations over a year - influence on dust signature

A summary of the influence of the background conditions on the spectrum is given in Table 4.2. Note that these results are valid for the EISCAT radar location (north hemisphere, at high latitude) and may be different for other locations. Showing that during the summer the main influences, temperature and dust density (depending on dust size) cause a broader spectrum, while for winter conditions, they both contribute to a narrower spectrum. Making it easier to detect dust particles during winter.

The dust number density is according to models (Bardeen et al., 2008; Megner et al., 2008) higher during winter at lower altitudes due to atmospheric circulation, causing an updraft in the summer and a downdraft in the winter. This will cause larger dust sizes to be at lower altitudes during winter and a better chance of discerning them in the radar spectrum. The neutral density decreases during winter, which should cause a broadening compared to summer. However, this is a much smaller broadening than is caused by the narrowing of the temperature increase from summer to winter.

Table 4.2: Overview of the parameters that influence the spectrum and their relative change for winter and summer based on model nrlmsis-00 data over a year (Hedin, 1991). This is based on background values and does not capture local variations in time and space.

Constituents	Summer		Winter	
	>/<	Width	>/<	Width
Temperature	decreasing	Broader	increasing	Narrower
Neutral Density	increasing	Narrower	decreasing	Broader
Electron Density	increasing	-	decreasing	-
Dust number density	decreasing	+/-	increasing	Narrower

Figure 4.4 shows two examples of how the spectral width changes throughout the year, where the left panel shows the spectral width for conditions at 90 km and the right panel shows conditions for 80 km. Here, the spectral width is broader at 90 km when including dust; this is due to the large amount of small negative dust included for this altitude, which broadens the spectrum instead of narrowing it. The results are reversed for the 80 km case, where the spectra are more narrow when dust is included. Here, we can see that there is

a much larger difference between the widths of the spectra with and without dust during winter. Note that here the frequency axis shown for the spectral width is the angular frequency and therefore greater by 2π compared to the frequency axis in Figure 4.3 and elsewhere in the thesis.
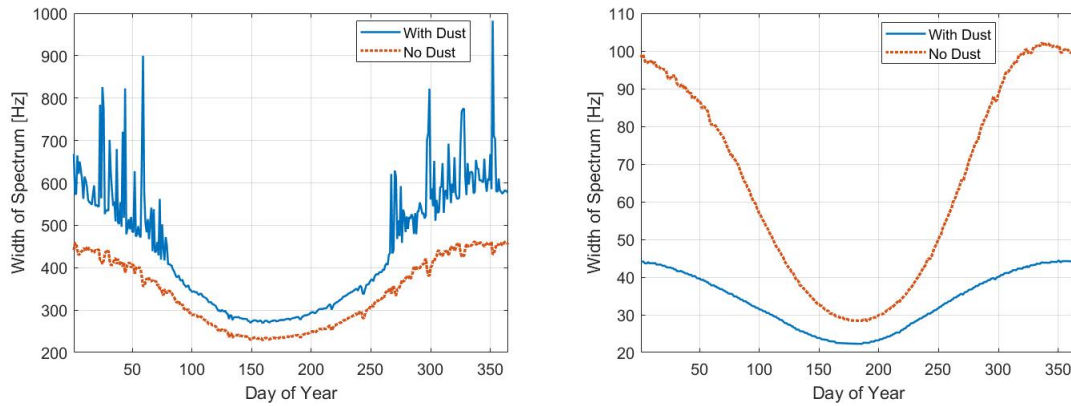

Figure 4.4: Spectral width variation in a year shown for two different altitudes. On the left is spectral width for 90 km and 80 km on the right. Spectral width frequency axis is here in angular frequency. Figures from Paper I.

4.2 Comparison of observational data with model calculations

To investigate the existence of a dust component in the radar spectrum, the radar observation displayed in the left panel of Figure 4.5 was selected. This observation was made with the EISCAT VHF radar on 9 January 2014 from about 08-22 UT. The electron density measurements show the presence of high electron content, possibly related to solar activity in the days prior to the observation (6-9 January 2014, solar flare activity (NASA)). The observation shows electron densities discernible down to almost 60 km altitude, and thus it was deemed a good observation to examine the influence of dust particles on the measured radar spectrum.

On the right in Figure 4.5 is the atmospheric temperature for the same time interval as the observation. It is a combination plot of the measured LIDAR temperature along with modeled temperature when there were no available LIDAR temperature data. The LIDAR temperature was measured with Tromsø Sodium LIDAR (Nozawa et al., 2014) and includes only measurements with an error smaller than 5 K. The model temperature is from the nrlmsise-00 model (Hedin, 1991).
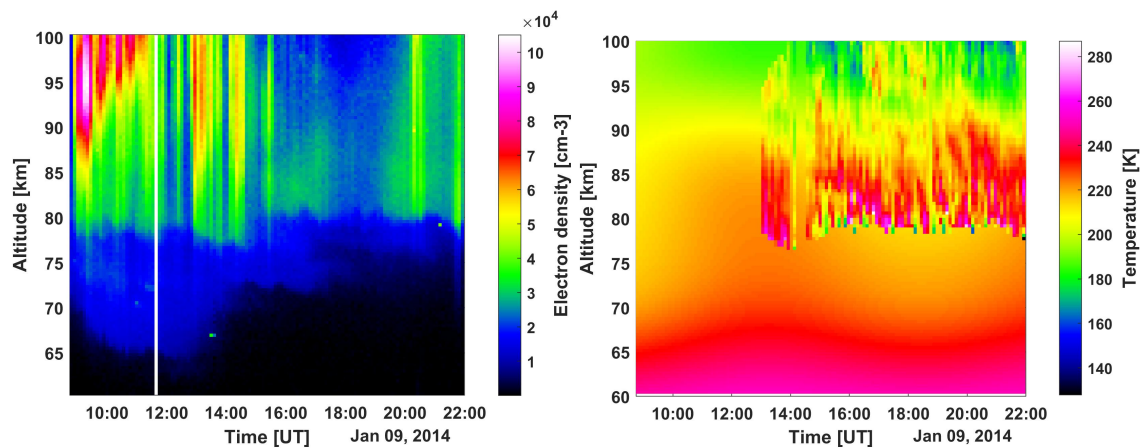
Figure 4.5: The left panels shows the electron density measured with the EISCAT VHF on 9 January 2014 and on the right is a combination plot of the measured LIDAR temperature and model nrlmsis-00 temperature on the same day. Model temperature is included where LIDAR temperature was not available. Figures are from Paper III.

Data processing summary:

- The raw radar data measured with the EISCAT VHF radar is run through Grand Unified Incoherent Scatter Design and Analysis Package (GUISDAP) (Lehtinen and Huuskonen, 1996) with a very low limit of satellite and meteor removal. The low limit is chosen as sigma = 1, or within 1 standard deviation instead of the usual 4 which increases the detection threshold and removes most signals that could be satellites or meteors.

- The GUISDAP raw data output is then run through RTG (real-time graph) with n = 375 and with spectrum and Doppler frequency shift as output. The resulting spectrum is then shifted in frequency.

- The raw radar data are also run through GUISDAP with the same removal as above, but with data processing selected to get the total electron density.

- Smoothing spectra with high noise levels and removing data dominated by noise.

- Adjustment of the ion-neutral collision frequency.

Smoothing the data

Here comes a brief overview of the smoothing of certain parts of the data. This is not explained in detail in Paper III and is therefore highlighted here for reference. Spectrum measured at low altitude (low electron density) and at high altitude (low range resolution) are often quite dominated by noise and do not have a relatively smooth spectral curve. First, all cases of spectrum that clearly are only noise are removed. An example can be seen in Figure 4.6,

in the first two panels. The third case is not removed, since we can see that there is an underlying broad spectrum. However, this spectrum is very noisy and difficult to accurately compare with model calculations.
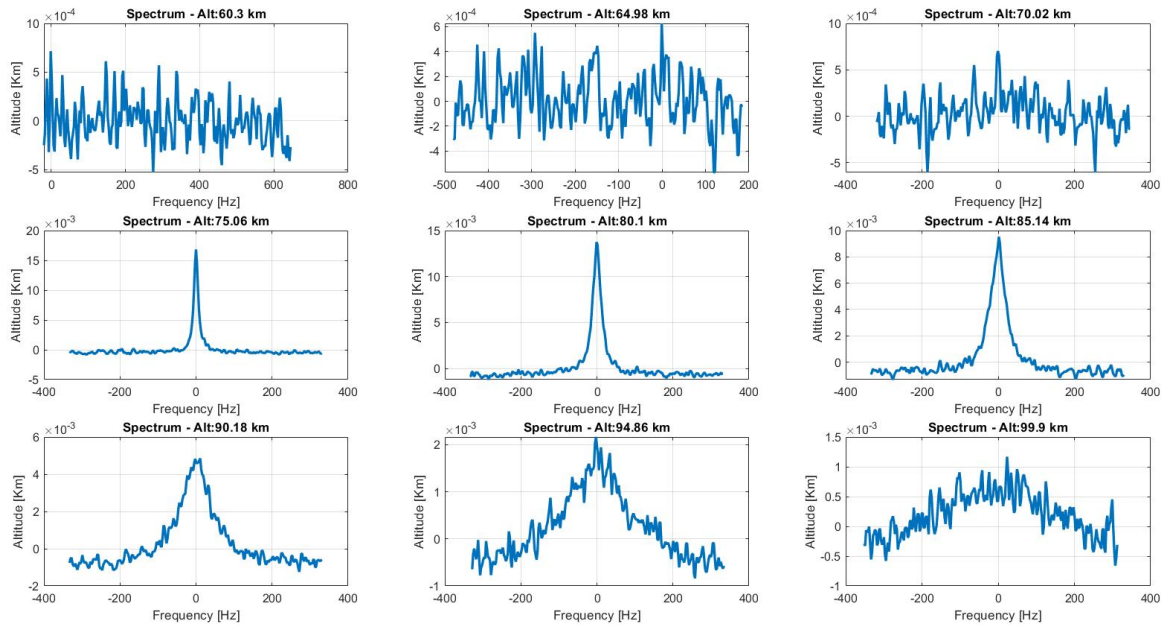

Figure 4.6: Example of several spectra from the observation on 9 January 2014. All are taken at time 11:02:57 UT and represent different altitudes, shown above each corresponding figure.

At higher altitudes, for example, in the top panel of the same figure (Figure 4.6), the measured spectrum becomes increasingly noisy with altitude. This is due to the low range resolution of the Manda code above around 90 km. These spectra (at low and high altitude) are then smoothed with a smoothing filter (Savitzky–Golay matlab filter) in the frequency range $\pm$ 100 Hz. Depending on the "amount" of noise present, the individual spectra are smoothed with two different thresholds of the filter. The Savitzky–Golay filter is a smoothing filter that smooths out the data points in a certain area and essentially removes the noise using a least-squares linear fit of a few data points at a time. For the cases heavily influenced by noise, we used a larger data set of smoothed points.

Figure 4.7 shows the basic overview of the selection method for the two thresholds. First, each spectrum in the frequency range $\pm$ 100 Hz was normalized, and then the sum of the difference between each data point was taken. Then the thresholds of that sum were set empirically by examining the different sums of the observation. Those cases that had a sum smaller than 3 were not smoothed since these spectrum were not influenced by noise, and smoothing these we could potentially remove the peak of the spectrum, which is where the dust influence is expected. The spectra with sums in the range between 3 and 4.5 were smoothed with only a few data points of the filter, while the sums

with a sum between 4.5 and 10 were smoothed with a large filter. All spectra with sums above 10 were removed, since these mainly contained noise.
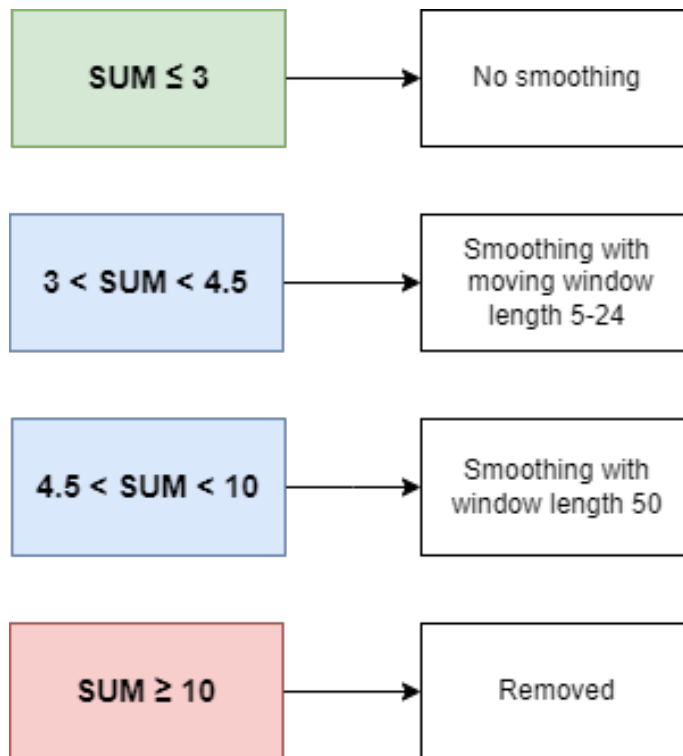

Figure 4.7: Overview of the selection process for different smoothing thresholds.

An example of the smoothing process is shown in Figure 4.8, where the first case is not smoothed, since it clearly contains only noise. The case in the middle is smoothed with a small threshold, and the case on the right shows a heavily noisy spectrum, which is smoothed with a large filter. Cases like the one on the right are removed when smoothing it with a large filter does not work. These spectra are from 99 km altitude and are very noisy. The smoothing process in most cases works quite well except for these heavily noise influenced spectra. Note that smoothing the spectra does not mean that we accurately determine the spectral shape for that altitude. Therefore, for many spectra above 90 km that are smoothed, we cannot determine dust properties with a good accuracy, since the measured spectra are so influenced by noise. As discussed later, these measurements also do not produce good agreement when including a dust distribution.
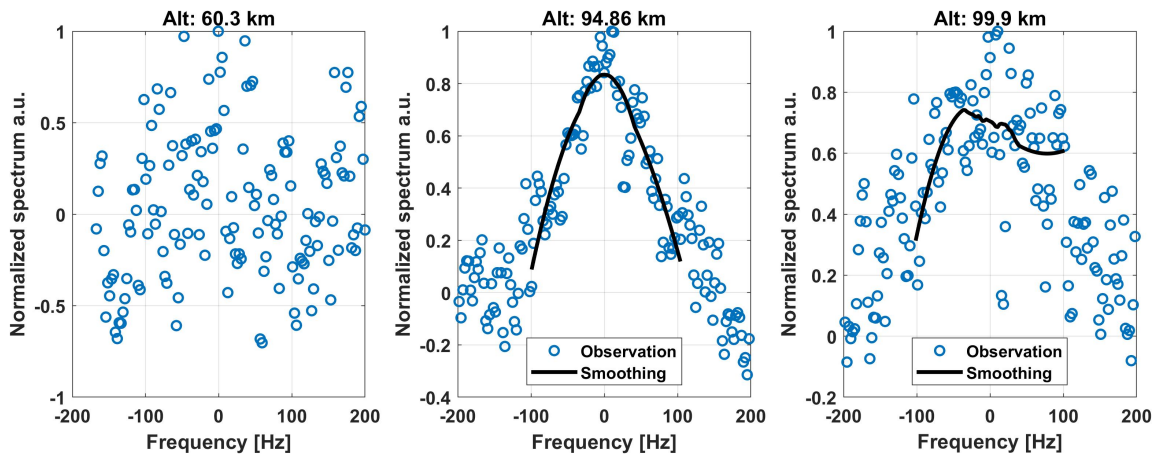
Figure 4.8: Examples of three different measured spectra at different altitudes. The spectrum on the left contains only noise and is not smoothed. The two others are smoothed, the middle one with a small data filter and the one on the right is smoothed with a large data filter.

Adjusting the ion-neutral collision frequency

An adjustment of the ion-neutral collision frequency was necessary prior to fitting the data with a dust component. Since the plasma in this altitude range is highly collisional and is basically determined by their collisions with neutrals, an accurate estimation of this collision frequency is important to get a good agreement with the measurement. It was recently suggested by Thomas et al. (2023) that the collision frequency of the D-region might be reduced by a factor of ≈ 1.5. And after comparing the spectra measured by the EISCAT VHF radar with the model calculations of a spectrum without a dust component, we saw that compared to the modeled spectra, the observations were often too narrow in the frequency range around ± 50 Hz. This could not be caused by the presence of dust, as the dust mainly creates an additional narrow peak on top of the background spectra and does not narrow the entire spectrum in this frequency range.

Therefore, we modeled a spectrum (without a dust component) with several different multiplications of the ion-neutral collision frequency and found the best fit. The tested multipliers ranged from 0 to 3, with 0.5 mainly at the low electron density areas at low altitudes, around 1-1.5 in between 70-80 km and 1.5-2 up to 95 km with a few higher cases. A detailed figure of the multiplier is given in Paper III. An example of a measured spectrum is given in Figure 4.9 (red line), along with a modeled spectrum without a dust component (blue) and a spectrum modeled with the collision frequency adjustment (black). Here, we can see that a spectrum modeled with an adjustment of the collision frequency fits the observed spectra quite well compared to the modeled spectra with no adjustment.
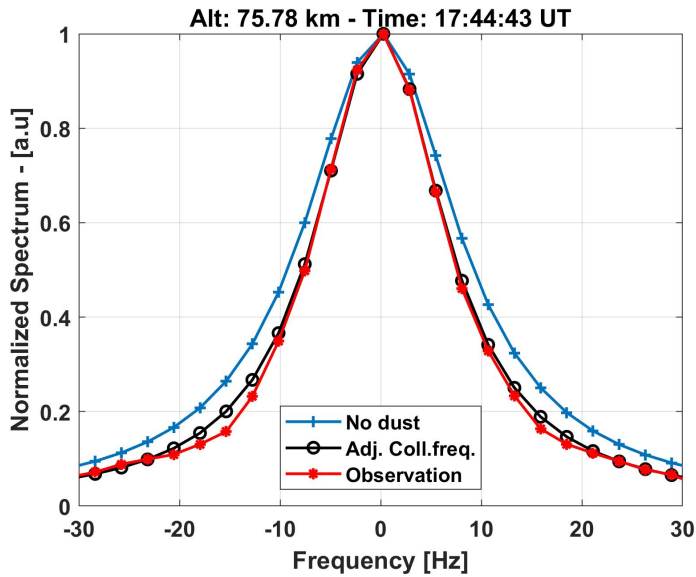
Figure 4.9: Example measured spectrum(red) with a model calculation with an adjusted collision frequency (black) and a modeled spectrum with no adjustment (blue). Figure from Paper III.

Including dust in model calculations

To include a dust component in the modeled spectrum, we use a model output of a dust distribution from the WACCM-CARMA model (see model parameters in Paper III). This distribution is the average distribution for the month of January, and there is no information on the number of charged particles. To estimate the charge of the particles, we extrapolated the charging model given in Table 2.6 in Antonsen (2019). Here, we use the charging model that has the lowest charging probability for small dust particles compared to larger dust sizes. Here we have also assumed that small dust (<0.5 nm) remains uncharged. The reason for this is that the larger dust influences the spectrum to a larger degree (see results from Paper I) and the smaller dust in the range 0.5-1 nm mainly increases the amplitude of the spectrum, while the larger particles will influence the spectral width as well. This is assuming negative dust particles. Positive dust particles will have a narrowing effect on the spectrum for all sizes, but it is more likely that the dust is negatively charged due to electron attachment (Baumann et al., 2013).

By including the charging model, we reduce the total number density, to investigate if there is an increase or a decrease in number density needed of dust to fit to each individual spectra, we test for several multiplications of the starting number density and find the best fit. The resulting multiplier found for the best fit of the dust to the measured spectra is shown in Figure 4.10 on the right and the resulting total number density on the left (both log scales). The white areas in the figures represent spectra with bad data, too little or no electron density, or the spectra fit best to a model calculation without dust or with only adjusting the collision frequency. Note that the collision frequency is adjusted as discussed above before including dust in the model calculation.
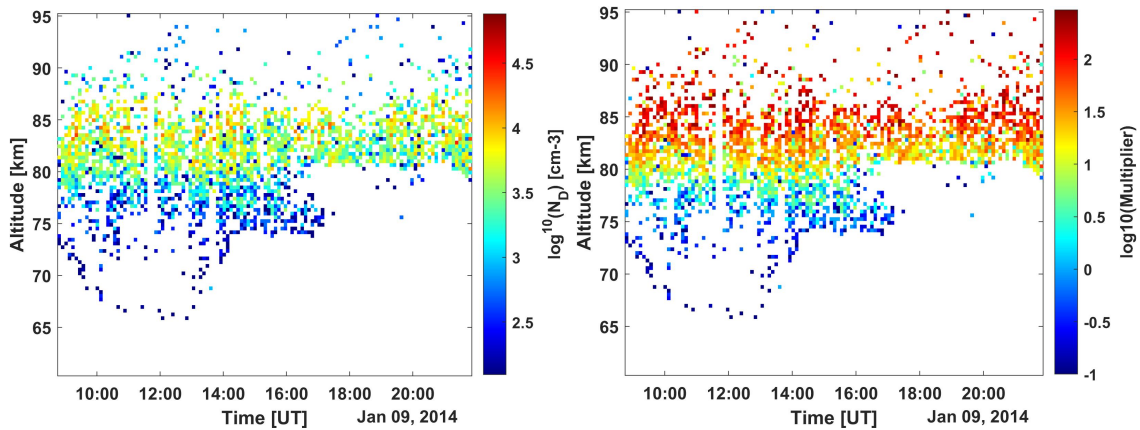
Figure 4.10: Negative dust number density (cm-3) shown on the left with associated multiplier on the right. Both figures are log scale. Figures from Paper III.

On the left in Figure 4.10 a layer of dust is seen in the altitude range 80-85 km with number densities around $10^4 \ cm^{-3}$, and a smaller layer in the altitude range 75-80 km can be seen up to around 17 UT where the electron density is no longer high enough for a good radar signal, with number densities around $10^3 \ cm^{-3}$.
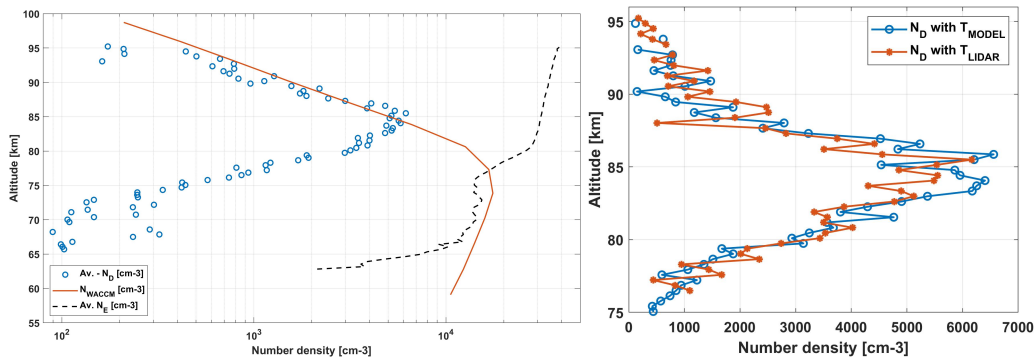

Figure 4.11: Derived average dust density for negatively charged dust particles on the left, shown with the average measured electron density and the total dust density from the WACCM-CARMA model. On the right is the average derived dust density for all cases using LIDAR temperature compared to the average density using model temperature. Figures from Paper III.

Figure 4.11 shows the average charged dust number density needed for each altitude compared to the total dust number density from the WACCM-CARMA model and the average measured electron density. Here, we can see that the peak number density seems to lie around 85 km and mostly follows the total model density to higher altitudes. Below 85 km, the dust number density decreases, following the electron density decrease. On the right in Figure 4.11 the average number density derived using the LIDAR temperature and the

model temperature is shown. They have similar altitude ranges, where centered around 85 km the number density derived with LIDAR temperature often has lower number densities than the model-derived number density. Here, the decrease in the average number density compared to the model number density is most likely due to a decrease in charged dust particles along with the decrease in electron number density. As shown in Figure 4.2 on the left, an increase in temperature causes a broader spectrum, and when comparing the model temperature and the LIDAR temperature of Figure 4.5 there is mainly an increase in temperature in this altitude range compared to the model temperature. A broader spectrum will result in a reduced number density fit for that spectrum compared to a narrower one.

Chapter 5

Summary and future work

Summary of main results

Paper I examines the influence of dust and other variables on the incoherent scatter spectrum. The largest influence (apart from dust) is temperature, its influence is of a similar order to that of dust particles. Larger dust particles influence the spectrum to a greater extent than smaller ones. Positive dust particles have a larger influence than negative ones due to the charge-neutrality condition. Examining background values over the year shows that winter conditions are optimal for detecting dust, as a larger narrowing of the spectrum is expected compared to summer.

Paper II examines the time variations of PMSE signals (overshoot characteristic curves) produced when the electrons are artificially heated at PMSE altitudes. PMSE layers are heated in on-and-off cycles of 48/168 s. To the best of our knowledge, this is the first time that overshoot characteristic curves have been studied during low solar illumination. Similarly to the studies by other authors, we found that no heating effect can be seen in the PMSE layer when particle precipitation is present and the electron density is high. Some individual overshoots seen were very high, where the largest overshoots were seen in PMSE layers with overall low PMSE power at high altitudes. A comparison to a model (by Alireza Mahmoudian) showed that, indeed, a reduced photoionization rate as a result of reduced solar illumination can increase the overshoots. However, the highest observed overshoots could not be reproduced with the model.

Paper III examines an observations with the EISCAT VHF radar from 9 January 2014 with high electron content in the D-region to determine if a dust component can be derived from the observations. We compared measured spectra with 6.5 minute time resolution with model calculations without a dust component, with an adjusted collision frequency and including a dust component. We found that including dust fits best in the altitude range 75-85 km with number densities in the range of a few hundred particles up to a few thousand (cm-3). The average dust density has a peak at 85 km, somewhat higher than the WACCM-CARMA model total number density; however, the total number density of charged dust decreases as the electron density decreases.

Future work

Radar measurements of dust in the mesosphere are possible because dust particles are electrically charged and interact with other plasma components. Dust charging has been studied before, also including recent model calculations of the charge balance (Baumann et al., 2015) but only under quiet ionospheric conditions. It will be important for future research to extend this work. For instance, with variable ionospheric conditions, to better understand how the dust component is charged.

To determine the dust component in the incoherent scatter, an extension of the fluid equation description (Cho et al., 1998) was used. This theory relies heavily on the ion-neutral collision frequency, and, as was shown, this had to be adjusted to fit the measured spectra. The discrepancies between the observations and the modeled ion-neutral collision frequencies have also been noted in other studies; and Thomas et al. (2023) have recently started investigating them. Now that there is observational evidence for the influence of the charged dust, this could also give rise to theoretical investigations of the incoherent scatter in the D-region.

Concerning the coherent scatter observations of PMSE, the large overshoots observed during heating experiments could not be reproduced quantitatively with existing models; investigating the possible different charging conditions may help to properly understand the role of dust in PMSE and to find out whether the rapid variations that occur from one heating cycle to the next are caused by dust charging effects.

The new EISCAT_3D is expected to provide improved conditions for observational studies. In general, different radar methods used to determine a dust component should be further developed and tested along with examining the dust charging in detail, especially to be used with EISCAT_3D. It is important to combine future radar measurements with other complementary experiments, like different instruments on sounding rockets. Simultaneous observations of the same volume with radar and rockets would allow a better determination of the neutral density and the dust charge density. A better understanding of the D-region incoherent scatter spectrum achieved with the studies would allow us to develop long time-series observations. This is especially important since the material from space debris is increasing and might eventually or locally surpass the different ablated meteors (Schulz and Glassmeier, 2021).

References

Antonsen, T.: In-situ Measurements of Mesospheric Aerosols - On the observable characteristics of nanoscale ice and meteoric smoke particles, Ph.D. thesis, UiT, 2019.

Antonsen, T., Havnes, O., and Mann, I.: Estimates of the Size Distribution of Meteoric Smoke Particles From Rocket-Borne Impact Probes, Journal of Geophysical Research: Atmospheres, 122, 2017.

Asmus, H., Robertson, S., Dickson, S., Friedrich, M., and Megner, L.: Charge balance for the mesosphere with meteoric dust particles, Journal of Atmospheric and Solar-Terrestrial Physics, 127, 137–149, 2015.

Bardeen, C., Toon, O., Jensen, E., Marsh, D., and Harvey, V.: Numerical simulations of the three-dimensional distribution of meteoric dust in the mesosphere and upper stratosphere, Journal of Geophysical Research: Atmospheres, 113, 2008.

Bardeen, C., Toon, O., Jensen, E., Hervig, M., Randall, C., Benze, S., Marsh, D., and Merkel, A.: Numerical simulations of the three-dimensional distribution of polar mesospheric clouds and comparisons with Cloud Imaging and Particle Size (CIPS) experiment and the Solar Occultation For Ice Experiment (SOFIE) observations, Journal of Geophysical Research: Atmospheres, 115, 2010.

Baumann, C., Rapp, M., Kero, A., and Enell, C.-F.: Meteor smoke influences on the D-region charge balance–review of recent in situ measurements and one-dimensional model results, in: Annales Geophysicae, vol. 31, pp. 2049–2062, Copernicus GmbH, 2013.

Baumann, C., Rapp, M., Anttila, M., Kero, A., and Verronen, P. T.: Effects of meteoric smoke particles on the D region ion chemistry, Journal of Geophysical Research: Space Physics, 120, 10–823, 2015.

Chilson, P. B., Belova, E., Rietveld, M. T., Kirkwood, S., and Hoppe, U.-P.: First artificially induced modulation of PMSE using the EISCAT heating facility, Geophysical research letters, 27, 3801–3804, 2000.

Cho, J. Y., Sulzer, M. P., and Kelley, M. C.: Meteoric dust effects on D-region incoherent scatter radar spectra, Journal of atmospheric and solar-terrestrial physics, 60, 349–357, 1998.

Friedrich, M., Rapp, M., Plane, J. M., and Torkar, K. M.: Bite-outs and other depletions of mesospheric electrons, Journal of atmospheric and solar-terrestrial physics, 73, 2201–2211, 2011.

Hansen, G., Hoppe, U.-P., Turunen, E., and Pollari, P.: Comparison of observed and calculated incoherent scatter spectra from the D region, Radio science, 26, 1153–1164, 1991.

Havnes, O.: Polar Mesospheric Summer Echoes (PMSE) overshoot effect due to cycling of artificial electron heating, Journal of Geophysical Research: Space Physics, 109, 2004.

Havnes, O., Brattli, A., Aslaksen, T., Singer, W., Latteck, R., Blix, T., Thrane, E., and Trøim, J.: First common volume observations of layered plasma structures and polar mesospheric summer echoes by rocket and radar, Geophysical research letters, 28, 1419–1422, 2001.

Havnes, O., Gumbel, J., Antonsen, T., Hedin, J., and La Hoz, C.: On the size distribution of collision fragments of NLC dust particles and their relevance to meteoric smoke particles, Journal of Atmospheric and Solar-Terrestrial Physics, 118, 190–198, 2014.

Hedin, A. E.: Extension of the MSIS thermosphere model into the middle and lower atmosphere, Journal of Geophysical Research: Space Physics, 96, 1159–1172, 1991.

Hervig, M. E., Deaver, L. E., Bardeen, C. G., Russell III, J. M., Bailey, S. M., and Gordley, L. L.: The content and composition of meteoric smoke in mesospheric ice particles from SOFIE observations, Journal of Atmospheric and Solar-Terrestrial Physics, 84, 1–6, 2012.

Hunten, D. M., Turco, R. P., and Toon, O. B.: Smoke and dust particles of meteoric origin in the mesosphere and stratosphere, Journal of the Atmospheric Sciences, 37, 1342–1357, 1980.

Kassa, M., Havnes, O., and Belova, E.: The effect of electron bite-outs on artificial electron heating and the PMSE overshoot, 2005.

Kudeki, E. and Milla, M. A.: Incoherent scatter spectral theories—Part I: A general framework and results for small magnetic aspect angles, IEEE Transactions on Geoscience and Remote Sensing, 49, 315–328, 2010.

Lehtinen, M. S. and Huuskonen, A.: General incoherent scatter analysis and GUISDAP, Journal of Atmospheric and Terrestrial Physics, 58, 435–452, 1996.

Lübken, F.-J.: Thermal structure of the Arctic summer mesosphere, Journal of Geophysical Research: Atmospheres, 104, 9135–9149, 1999.

Mahmoudian, A., Scales, W. A., Kosch, M., Senior, A., and Rietveld, M.: Dusty space plasma diagnosis using temporal behavior of polar mesospheric summer echoes during active modification, in: Annales Geophysicae, vol. 29, pp. 2169–2179, Copernicus GmbH, 2011.

Mahmoudian, A., Mohebalhojeh, A., Farahani, M., Scales, W., and Kosch, M.: Remote sensing of mesospheric dust layers using active modulation of PMWE by high-power radio waves, Journal of Geophysical Research: Space Physics, 122, 843–856, 2017.

Mathews, J. D.: The effect of negative ions on collision-dominated Thomson scattering, Journal of Geophysical Research: Space Physics, 83, 505–512, 1978.

Megner, L., Siskind, D., Rapp, M., and Gumbel, J.: Global and temporal distribution of meteoric smoke: A two-dimensional simulation study, Journal of Geophysical Research: Atmospheres, 113, 2008.

Mironova, I. A., Aplin, K. L., Arnold, F., Bazilevskaya, G. A., Harrison, R. G., Krivolutsky, A. A., Nicoll, K. A., Rozanov, E. V., Turunen, E., and Usoskin, I. G.: Energetic particle influence on the Earth's atmosphere, Space science reviews, 194, 1–96, 2015.

Myrvang, M., Baumann, C., and Mann, I.: Modelling of the influence of meteoric smoke particles on artificial heating in the D-region, Annales Geophysicae Discussions, pp. 1–21, 2021.

NASA: Solar Proton Events from 1976, URL `https://umbra.nascom.nasa.gov/SEP/`, [Online; accessed 20-june-2023].

Nozawa, S., Kawahara, T., Saito, N., Hall, C., Tsuda, T., Kawabata, T., Wada, S., Brekke, A., Takahashi, T., Fujiwara, H., et al.: Variations of the neutral temperature and sodium density between 80 and 107 km above Tromsø during the winter of 2010–2011 by a new solid-state sodium lidar, Journal of Geophysical Research: Space Physics, 119, 441–451, 2014.

Pinedo, H., La Hoz, C., Havnes, O., and Rietveld, M.: Electron–ion temperature ratio estimations in the summer polar mesosphere when subject to HF radio wave heating, Journal of Atmospheric and Solar-Terrestrial Physics, 118, 106–112, doi: https://doi.org/10.1016/j.jastp.2013.12.016, URL `https://www.sciencedirect.com/science/article/pii/S1364682613003349`, recent progress from networked studies based around MST radar, 2014.

Plane, J. M., Feng, W., and Dawkins, E. C.: The mesosphere and metals: Chemistry and changes, Chemical reviews, 115, 4497–4541, 2015.

Plane, J. M. C.: Cosmic dust in the earth's atmosphere, Chem. Soc. Rev., 41, 6507–6518, doi: 10.1039/C2CS35132C, URL `http://dx.doi.org/10.1039/C2CS35132C`, 2012.

Rapp, M. and Lübken, F.-J.: Polar mesosphere summer echoes (PMSE): Review of observations and current understanding, 2004.

Rapp, M., Strelnikova, I., and Gumbel, J.: Meteoric smoke particles: Evidence from rocket and radar techniques, Advances in Space Research, 40, 809–817, 2007a.

Rapp, M., Strelnikova, I., Strelnikov, B., Latteck, R., Baumgarten, G., Hoppe, U., Brattli, A., Friedrich, M., Gumbel, J., Megner, L., et al.: Measurements of Meteor Smoke and Ice Particles During the ECOMA-2006 and ECOMA/MASS-2007 Rocket Campaigns, in: AGU Fall Meeting Abstracts, vol. 2007, pp. SA21A–0271, 2007b.

Rapp, M., Strelnikova, I., Strelnikov, B., Hoffmann, P., Friedrich, M., Gumbel, J., Megner, L., Hoppe, U.-P., Robertson, S., Knappmiller, S., et al.: Rocket-borne in situ measurements of meteor smoke: Charging properties and implications for seasonal variation, Journal of Geophysical Research: Atmospheres, 115, 2010.

Rapp, M., Plane, J., Strelnikov, B., Stober, G., Ernst, S., Hedin, J., Friedrich, M., and Hoppe, U.-P.: In situ observations of meteor smoke particles (MSP) during the Geminids 2010: constraints on MSP size, work function and composition, in: Annales geophysicae, vol. 30, pp. 1661–1673, Copernicus Publications Göttingen, Germany, 2012.

Rietveld, M., Kohl, H., Kopka, H., and Stubbe, P.: Introduction to ionospheric heating at Tromsø—I. Experimental overview, Journal of atmospheric and terrestrial physics, 55, 577–599, 1993.

Rosinski, J. and Snow, R.: Secondary particulate matter from meteor vapors, Journal of Meteorology, 18, 736–745, 1961.

Röttger, J., La Hoz, C., Kelley, M. C., Hoppe, U.-P., and Hall, C.: The structure and dynamics of polar mesosphere summer echoes observed with the EISCAT 224 MHz radar, Geophysical research letters, 15, 1353–1356, 1988.

Scales, W. and Mahmoudian, A.: Charged dust phenomena in the near-Earth space environment, Reports on Progress in Physics, 79, 106 802, 2016.

Schulte, P. and Arnold, F.: Detection of upper atmospheric negatively charged microclusters by a rocket-borne mass spectrometer, Geophysical research letters, 19, 2297–2300, 1992.

Schulz, L. and Glassmeier, K.-H.: On the anthropogenic and natural injection of matter into Earth's atmosphere, Advances in Space Research, 67, 1002–1025, 2021.

Strelnikov, B., Staszak, T., Latteck, R., Renkwitz, T., Strelnikova, I., Lübken, F.-J., Baumgarten, G., Fiedler, J., Chau, J. L., Stude, J., et al.: Sounding rocket project "PMWE" for investigation of polar mesosphere winter echoes, Journal of Atmospheric and Solar-Terrestrial Physics, 218, 105 596, 2021.

Strelnikova, I., Rapp, M., Raizada, S., and Sulzer, M.: Meteor smoke particle properties derived from Arecibo incoherent scatter radar observations, Geophysical Research Letters, 34, 2007.

Tanaka, K. K., Mann, I., and Kimura, Y.: Formation of ice particles through nucleation in the mesosphere, Atmospheric Chemistry and Physics Discussions, 2021, 1–17, doi: 10.5194/acp-2021-728, URL `https://acp.copernicus.org/preprints/acp-2021-728/`, 2021.

Tanenbaum, B. S.: Continuum theory of Thomson scattering, Physical Review, 171, 215, 1968.

Thomas, N., Kero, A., and Virtanen, I.: Study of D region ionosphere using incoherent scatter radar measurements, doi: https://doi.org/10.5194/egusphere-egu23-12698, 2023.

Ullah, S., Li, H., Rauf, A., Meng, L., Wang, B., and Wang, M.: Statistical study of PMSE response to HF heating in two altitude regions, Earth, Planets and Space, 71, 1–14, 2019.

Vaste, O.: Noctilucent clouds, Journal of atmospheric and terrestrial physics, 55, 133–143, 1993.

PAPER I

Charged Dust in the D-region incoherent scatter spectrum

Charged dust in the D-region incoherent scatter spectrum

Tinna L. Gunnarsdottir [1],† and Ingrid Mann [1]

[1]Department of Physics and Technology, UiT Arctic University of Norway, 9037 Tromsø, Norway

We investigate the influence of charged dust on the incoherent scatter from the D-region ionosphere. Incoherent scatter is observed with high-power, large aperture radars and results from electromagnetic waves scattering at electrons that are coupled to other charged components through plasma oscillations. The influence of charged dust can hence be considered an effect of dusty plasma. The D-region contains meteoric smoke particles that are of nanometre size and form from incoming ablating meteors. Detection of such charged dust in the incoherent scatter spectrum from the D-region has previously been proposed and studied to some degree. We here present model calculations to investigate the influence of the charged dust component with a size distribution, instead of the one size dust components assumed in other works. The developed code to calculate the incoherent scatter spectrum from the D-region including dust particles with different sizes and different positive and negative charge states is made available (https://doi.org/10.18710/GHZIIY). We investigate how sizes, number density and charge state of the dust influence the spectrum during different ionospheric conditions. We consider the ionospheric parameters for the location of the EISCAT VHF radar during a year and find that conditions are most suitable for dust detection in winter below 80 km at times with increased electron densities. The prospects to derive dust parameters increase, when the incoherent scatter observations are combined with those of other instruments to provide independent information on electron density, neutral density and temperature.

Key words: dusty plasmas, space plasma physics

1. Introduction

The ionosphere of Earth is one of the few systems where dusty plasma can directly be observed in nature. The influence of charged dust on the incoherent scatter is a result of dusty plasma and we study this systematically. The ionospheric D-region is a low temperature, partially ionized plasma environment which contains small charged dust particles. Parts of the D-region with this embedded dust can be considered a dusty plasma where the charged dust takes part in the collective effects of the plasma. Hagfors (1992) studied the theory of a plasma with embedded charged dust to investigate the resulting enhancement of radar signals. While this influence was found to be small, the charged

† Email address for correspondence: tinna.gunnarsdottir@uit.no

dust affects the incoherent scatter spectrum and Cho, Sulzer & Kelley (1998) developed a model to describe the spectrum in the presence of charged dust.

Strelnikova *et al.* (2007) and Rapp, Strelnikova & Gumbel (2007) applied this model and further developed a method to detect the dust signatures in observed radar spectra. Such dust signatures in observed spectra were also reported by Fentzke *et al.* (2009, 2012), but these are only a few cases and the detection is probably constrained by spectral resolution and radar capabilities (Rapp *et al.* 2007). It is, however, worthwhile to pursue such observational studies, since they would be helpful for investigating the dust formation in the vicinity of meteors and the role of dust in other observed radar phenomena (Mann *et al.* 2019). Since the incoherent scatter technique provides a robust method of ground-based observations independent from the weather conditions, it would also be worthwhile to use them for monitoring observations of the dust.

Estimating the influence of the charged dust is also of interest for analysing observed D-region incoherent scatter spectra and for understanding observed differences between observations and models (Hansen *et al.* 1991; Rapp *et al.* 2007). The influence that ion composition and mass and collisions with neutrals have on the spectrum, make the analysis of D-region incoherent scatter difficult and the charged dust is an additional factor.

The dust in the mesosphere originates from the ablation of meteors (Kalashnikova *et al.* 2000) and most material deposition in the atmosphere occurs around 75–120 km (Hunten, Turco & Toon 1980). The ablated material re-condenses into nanometre sized particles denoted as meteoric smoke particles (MSPs) (Rosinski & Snow 1961). These MSPs are transported with the neutral atmosphere and they can further grow through coagulation. They are additionally thought to influence several processes, both in the mesosphere and the stratosphere. This includes the growth of ice particles, chemical processes and charge interactions (Hunten *et al.* 1980). Their small size and high altitude make them difficult to measure and several inherent properties are not well known or only predicted based on theory.

Atmospheric models have been employed to better understand the possible conditions of MSPs in the mesosphere and to understand their effect on their surroundings as well as how they are transported in the meridional circulation (Megner, Rapp & Gumbel 2006; Bardeen *et al.* 2008; Megner *et al.* 2008); coupling of atmospheric models and chemistry models has also been investigated (Baumann *et al.* 2015). A major uncertainty in the model calculations is the number of forming MSPs, their size, their charge state and the amount of neutral versus charged particles (Megner *et al.* 2008; Baumann *et al.* 2015).

In this paper we investigate the incoherent scatter spectrum in the presence of charged dust. The aim of this work is to investigate to what extent charged dust particles influence the incoherent scatter spectrum from the D-region and to find ionospheric conditions that are best suited for deriving dust parameters. Starting with the description of the scatter spectrum developed by Cho *et al.* (1998) we expand this to include a dust size distribution and dust with different charge numbers. We investigate the spectrum for different ionospheric conditions and different assumptions on the dust component based on present knowledge on MSPs. We calculate spectra for the frequency of the EISCAT VHF radar (224 MHz) and investigate the influence that ionospheric conditions have on the spectra. For this we consider the ionospheric conditions at the EISCAT site in Ramfjordmoen and the variation of these during a year. We developed a code to calculate the incoherent scatter spectrum which we base on previous works by Strelnikova (2009) and Teiser (2013) and expand by including dust with different charge numbers and with a size distribution. We investigate in detail how the dust influences the spectra and prepare future observations by deriving the conditions that are most suitable for retrieving dust information from observed spectra.

This paper is organized as follows. Section 2 provides an overview of the model approach to calculate the incoherent scatter spectrum and discusses the inclusion of dust parameters as well as the role of dust collisions with neutrals in the equations. We discuss the dusty plasma conditions, the influences of dust size and charge distributions and the limitations of the model in § 3. In § 4 we investigate the variation of the spectrum with different ionospheric conditions and dust assumptions based on MSP models. Section 5 addresses the variation of spectra during the day and during the year. Section 6 provides a summary and conclusions. We give supporting information on the calculations and the access to the code that we developed in Appendix C.

2. Model approach

The radar signal that is denoted as incoherent scatter comes from Thomson scattering of ionospheric electrons that are coupled to the other charged components, predominantly positive ions. Below 80 km, also negative ions play a role. Similar to the ions, the charged dust particles participate in the plasma oscillations and influence the charge balance.

Due to the high neutral density in the D-region, collisions with neutrals damp the charge oscillations and change the shape of the spectrum. A theory of backscatter from a weakly ionized plasma has been developed by Dougherty & Farley (1963) and extended by Mathews (1978) to include multiple ion species (denoted the 3-fluid theory). Cho *et al.* (1998) further developed from this an N-fluid description to include dust particles in addition to the positive and negative ions for which they use the continuum approach by Tanenbaum (1968). We use this description for our model calculations.

2.1. *Incoherent scatter model*

We start by describing the formalism developed by Cho *et al.* (1998) and relevant equations that will be used in this work. The basic backscatter cross-section σ_b equation is given by

$$\sigma_b(\omega_0 + \omega)\,d\omega = Vr_e^2\langle|\Delta N_e(k, \omega)|2\rangle, \tag{2.1}$$

where ω_0 is the radar frequency and ω is the Doppler frequency shift from the radar frequency; V is the radar volume, r_e^2 is the classical electron radius, ΔN_e describes the electron density fluctuation spectrum and k is the Bragg wavenumber. The backscatter in the presence of charged dust can be described as (Cho *et al.* 1998)

$$\sigma_b(\omega_0 + \omega)\,d\omega = \frac{r_e^2 N_e}{\sqrt{2}\pi\omega} \left|\frac{1}{\alpha_e^2 + z_e\left(\sum_{s \neq e} Z_s^2 \frac{\alpha_s^2}{z_s}\right)}\right|^2$$
$$\times \left(\left|1 + \sum_{s \neq e} Z_s^2 \frac{\alpha_s^2}{z_s}\right|^2 z_e + \frac{\alpha_e^2}{T_e}\sum_{s \neq e} Z_s^2 T_s \frac{\alpha_s^2}{z_s^*}\right), \tag{2.2}$$

where T_s is the constituent temperature (the s constituents refer to ions and dust, positive or negative), T_e is the electron temperature and N_e is the electron number density. Here, we have included the charge number Z_s^2, where Cho *et al.* (1998) have chosen to set this as $Z_s^2 = 1$, which is often assumed valid for particles smaller than 10 nm. Note that everywhere the charge number is squared and thus the addition of dust does not depend

on the sign of the charge except in the assumption of charge neutrality. The constant α_s for each constituent s is given by

$$\alpha_s = \frac{1}{k\lambda_{Ds}} = \frac{e}{k}\left(\frac{N_s}{\varepsilon_o k_B T_s}\right)^{1/2}, \tag{2.3}$$

with λ_{Ds} being the Debye length, N_s the number density of each component, k_b is the Boltzmann constant and e is the elementary charge. Then z_s is given by

$$z_s = \frac{1 + i\dfrac{5\theta_s}{3\sigma s}}{1 + i\dfrac{\theta_s}{\sigma s}} + 2i\theta_s\left(\psi_s + \frac{2}{3d_s\psi s}\right) - 2\theta_s^2, \tag{2.4}$$

with d_s as the viscosity constant (the value used is given in table 1) and ψ_s is the normalized constituent–neutral collision frequency, here given by

$$\psi_s = \frac{v_{sn}}{\sqrt{2}kv_s}, \tag{2.5}$$

where v_{sn} is the constituent–neutral collision frequency defined below for each constituent and v_s is the mean thermal velocity, which is given by

$$v_s = \left(\frac{k_B T_s}{m_s}\right)^{1/2}, \tag{2.6}$$

with m_s as the component mass and the normalized frequency, θ_s from (2.4), is given by

$$\theta_s = \frac{\omega}{\sqrt{2}kv_s}. \tag{2.7}$$

Now σ_s (from (2.4)) is given by

$$\sigma_s = \frac{5m_s\psi_s}{m_s + m_n} + \frac{5}{4c_s\psi_s}, \tag{2.8}$$

with m_n being the neutral mass and c_s the thermal conductivity constant (values used here is given in table 1). The collision frequency v_{sn} with neutrals in (2.5) depends on the particles in question. First, the electron collision frequency with the neutrals can be approximated as (Banks & Kockarts 1973; Cho *et al.* 1998)

$$v_{en} = (3.78 \times 10^{-11} T_e^{1/2} + 1.98 \times 10^{-11} T_e)N_n. \tag{2.9}$$

Collision frequency of other constituents with the neutrals can either be described by the so called polarization collision frequency or the hard-sphere collision frequency. For both positive and negative ions the former is preferred and further discussions on the validity of that choice can be found in Cho *et al.* (1998). We assume a hard boundary of 0.5 nm for the size of the dust in relation to what collision frequency with the neutrals should be chosen and assume that this will not influence the spectrum in a large way. The polarization collision frequency is given by Banks & Kockarts (1973) and Cho *et al.* (1998) as

$$v_{sn}^P = 2.59 \times 10^{-9} \frac{N_n}{M_s^{1/2}} \sum_t F_t \left(\frac{M_{nt}\,\chi_{nt}}{M_s + M_{nt}}\right)^{1/2}, \tag{2.10}$$

where M_s is the mass of the charged constituent in atomic mass units (amu), F_t is the fractional volume of the neutral gas present, M_{nt} is mass of each neutral component (in

Parameters	*Mass*	*Radius*	
Electrons	$\sim 9.1 \cdot 10^{-31}$ kg	$\sim 2.82 \cdot 10^{-15}$ m	
Neutrals	$\sim 3.85 \cdot 10^{-26}$ kg	~ 0.15 nm	
Particle	*Viscosity constants*	*Thermal conductivity constants*	
Electrons	$d_e = 1.55$	$c_e = 1.5$	
Ions	$d_n = 1.78$	$c_n = 2.28$	
Dust	$d_d = 1.6$	$c_d = 2.1$	
Constituents	*Mass [amu]*	*Volume fraction %*	*Polarizability*
N2	$M_{N_2} = 28.01$	$f_{N_2} = 0.78$	$\chi_{N_2} = 1.74$
O2	$M_{O_2} = 31.99$	$f_{O_2} = 0.21$	$\chi_{O_2} = 1.57$
Ar	$M_{Ar} = 39.95$	$f_{Ar} = 0.01$	$\chi_{Ar} = 1.64$

TABLE 1. Parameters and values used for calculations as inputs into equation (2.2). Values from Cho *et al.* (1998). The constants given remain the same and are not changed for any of the calculations.

amu) and χ_{nt} is the polarizability of those components. The values used in the calculations are given in table 1. The major neutral atmospheric constituents: molecular nitrogen and oxygen and atomic argon are taken into account. For the dust collisions with the neutrals both collision frequencies must be used. For the smaller dust sizes the polarization collision frequency is larger until the size reaches around 0.5 nm. Then the hard-sphere collision frequency starts to become larger and should be preferred. Thus for particles larger than 0.5 nm we use hard-sphere collisions with frequency (Schunk 1975; Cho *et al.* 1998)

$$v_{sn}^H = \frac{8(r_s + r_n)^2 N_n}{3(m_s + m_n)} \left[\frac{2\pi k_B m_n (m_s T_n + m_n T_s)}{m_s} \right]^{1/2}, \qquad (2.11)$$

where r_n is the radius of the neutral particles. For neutral particles, we take an average radius of 0.15 nm (Cho *et al.* 1998). The collision frequencies for dust with neutrals thus can vary with dust size, mass density as well as the conditions of the neutral atmosphere. The influence these factors have on the spectrum are varied and we will examine them further in subsequent chapters.

2.2. *Incoherent scatter spectrum*

To illustrate the parameters that we will discuss in the following sections, we start by presenting in figure 1 the spectrum in the presence of positively charged dust, because this changes most clearly in comparison with the spectrum without dust. The solid line describes the typical D-region spectrum, the dashed line describes the spectrum with an added positive dust component. The influence of the dust can be seen in the central part of the spectrum which is displayed in the figure. It is often denoted as the ion line and it contains the vast majority of the back-scattered power. The inclusion of dust causes the amplitude of the spectrum to increase and the corresponding width of the spectrum narrows as is illustrated in panel (*a*) of figure 1 showing the back-scattered power as a function of the frequency shift (equation (2.2)). Here and in subsequent discussion we refer to the width as the half-width-half-maximum (HWHM) value of the spectrum.

Following the presentation of calculated spectra by Cho *et al.* (1998) and other authors, we show in figure 1(*b*) the same spectra with respect to the normalized frequencies (2.7). Note here the logarithmic scale and broader range of frequency. The spectra shown in the
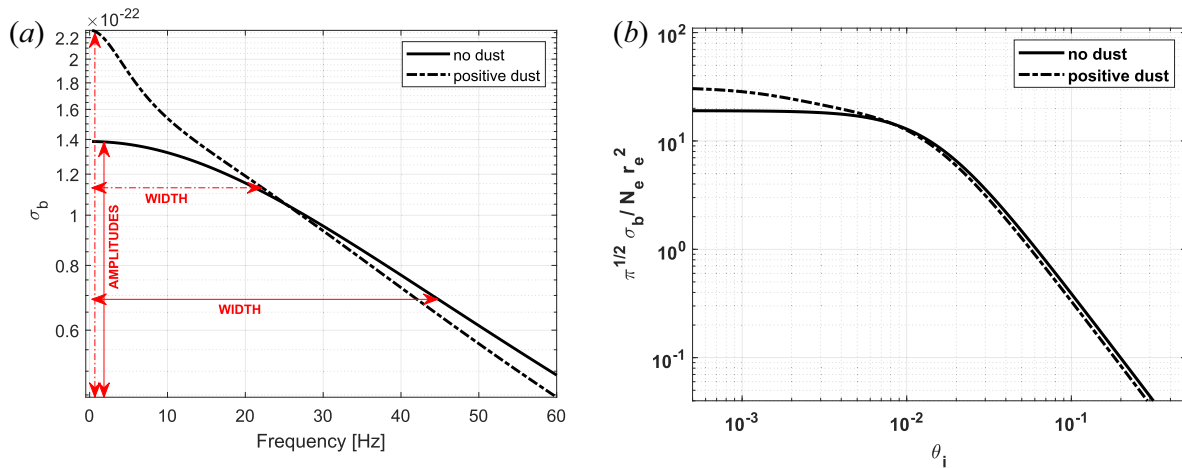
FIGURE 1. The central part of the incoherent scatter spectrum, ion line, calculated for conditions without dust and for different dust components is shown on the left; and the amplitude and width are indicated for both spectra. The figure on the right shows the corresponding normalized spectra; parameters used for the calculations are described in the text.

figure are calculated for the EISCAT VHF frequency of 224 MHz; this frequency is used throughout the paper. Other parameters used in these calculations are a constant electron density of 5000 cm^{-3} for each individual spectrum calculation while the amount of dust present was set to 1000 cm^{-3} and the positive ion density thus set to 4000 cm^{-3} to keep charge neutrality. If not mentioned otherwise, we use for the calculation singly charged dust, ion mass of 31 amu, neutral density of $5 \times 10^{14} \text{ cm}^{-3}$ and electron density values for 85–90 km height.

As can be seen in the figures, the presence of charged dust narrows the width of the spectrum and increases the central amplitude. This occurs independent from charge polarity but is most prominent for only positive dust particles and less so in the presence of negative and positive dust or of only negative dust. We choose in this paper to focus on the spectrum and the corresponding frequency as is seen in part (*a*). What we are interested in further is to examine the different parameters of the background atmosphere as well as the dust properties that might be present and how these influence both the spectrum amplitude and the width. And thus in the following sections we show for various cases the spectrum amplitude change on one side and the spectrum width on the other.

3. Dusty plasma conditions and influence of dust parameters

3.1. *Dusty plasma conditions*

The incoherent scatter from the D-region that we examine here is an example of dusty plasma, where the presence of charged dust particles changes the properties of the plasma. Goertz (1989) defines dusty plasma as an ensemble of dust particles in a plasma consisting of electrons, ions and neutrals. The dust charging leads to interactions with the surrounding plasma and charged dust particles are included through the charge neutrality condition describing the plasma. The charged dust particles are further influenced by electromagnetic forces and can be described as an additional ion component with a different charge to mass ratio. In a more narrow sense, dusty plasma describes conditions when the charged dust particles participate in the screening process rather than acting as isolated particles. For dusty plasma according to this latter definition (Mendis & Rosenberg 1994; Verheest 1996), the dust grain size, r_d, inter-particle distance a and
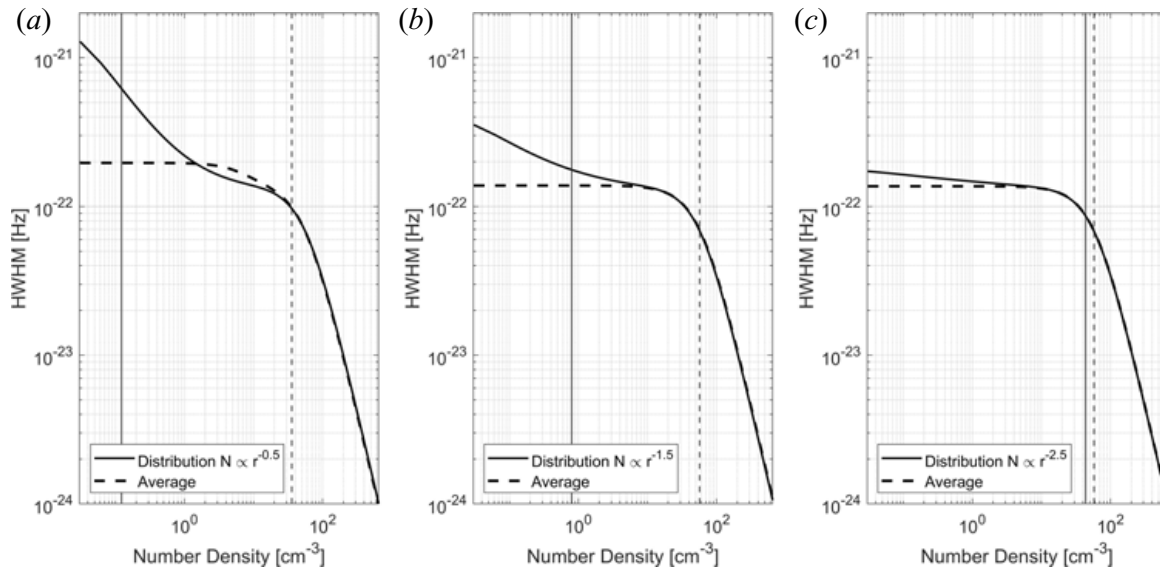
FIGURE 2. Spectrum shown for size distributions with different power laws given in figure 18 in Appendix A. Shown here with the spectrum calculated for the average size for each respective distribution. The number density of electrons is 5000 cm^{-3} and total number density for dust is chosen as 2000 cm^{-3} of negative particles. The vertical lines show the spectral width of each respective spectral line.

plasma Debye length, λ are such that $r_d \ll a < \lambda$. This relation holds for the conditions in the D-region ionosphere that we consider here (figures are shown in Appendix A).

3.2. *Dust size distributions*

The model can easily accommodate any size distribution of dust when calculating the spectrum. Let us consider three power law distributions where the number density is inversely proportional to the radius raised to the power of 0.5, 1.5 and 2.5; the number densities are constrained to 2000 cm^{-3} (see figure 18 in Appendix A). We use geometric size bins with the volume 1.6 times the previous size because this description is also used in dust transport models (Megner *et al.* 2006). Figure 2 compares the spectra calculated for the size distributions with those calculated with an average dust size. One can see that assuming an average dust size, as was done by other authors, provides a good result for steep size distributions (figure 2*c*) but fails to describe the spectra for a flatter dust size distribution. Thus obtaining an average size from spectra that are strongly influenced by the larger particles would overestimate the derived average size by a large amount.

3.3. *Dust charge state*

To investigate the influence of dust charge, we display the width of calculated spectra in figure 3. All cases shown are for negative dust particles (for positive particles see figure 19 in Appendix A). Figure 3(*a*) shows that the width of the spectra for different dust sizes and charge states 1 and 2 because the majority of dust in the D-region probably has small charges states (Baumann *et al.* 2015). One can see that the width of the spectra does not vary a lot with dust density for small particles, while the spectral width changes with density for the larger dust particles. This change depends in addition on the charge state. In 3(*b*) we show how the width changes for a 10 nm particle with several different charge numbers. For small negative charge, the spectrum is broad for small dust densities and then narrows. For charge states 5 and higher, the spectra are in general very narrow and
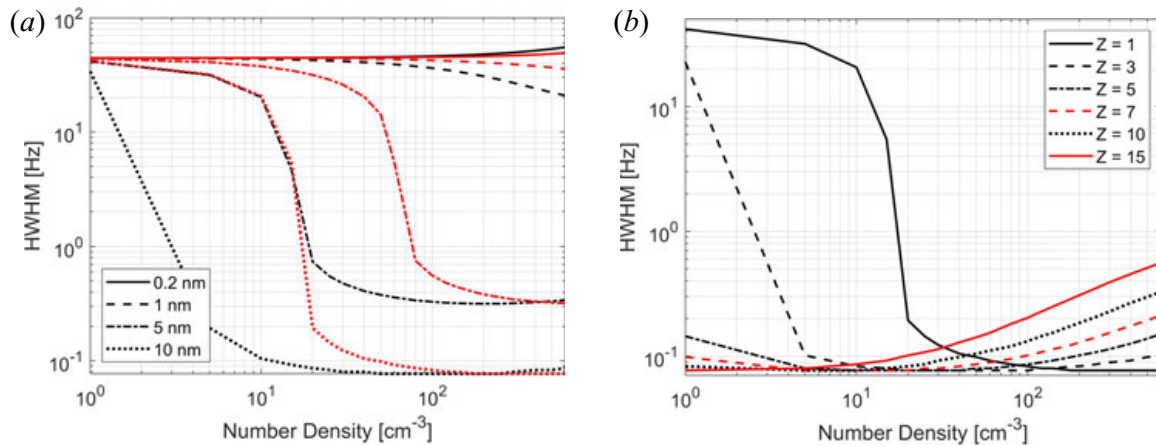
FIGURE 3. Spectral width (Hz) shown as a function of number density (cm^{-3}) for negative dust particles. In (*a*) several dust radii are shown for two different charge numbers Z where the red lines show $Z = 1$ and black lines show $Z = 2$. In (*b*) we show the spectral width for **10** nm particles for several charge numbers Z; (*a*) $Z_d = 1$ and **2** for $r_d = 0.2$, **1**, **5**, **7** and **10** nm and (*b*) $Z_d = 1$, **3**, **5**, **7**, **10** and **15** for $r_d = 10$ nm.

the width increases with dust density. We point out that the charge assumptions here are made for illustration and a discussion of charging models is beyond the scope of this work.

3.4. *Model limitations*

We use this model approach to investigate the influence of dust at 60–100 km altitude on the incoherent scatter. The model applies to a plasma that is collision dominated and weakly ionized (Cho *et al.* 1998). The frequencies of collisions of the charged particles with neutrals are high and any magnetic field effects as well as collisions between the charged particles can be neglected. Because of the high neutral density and predominance of collisions with neutrals, the temperatures of the different components can be considered equal. If the dust density in this region is large enough, it can influence the surrounding plasma and affect the spectra measured with radar.

4. Variation of the spectrum with ionospheric and dust parameters

We now investigate how the scatter spectrum depends on the dust properties and atmospheric conditions. Our calculations are made for mesospheric conditions at the location of the EISCAT VHF radar in Northern Norway (69.58° N and 19.23° E); they also apply for the new EISCAT_3D system, because both locations are less than 50 km apart. The MSPs are thought to reside at altitudes ranging in the D-region so we consider altitudes from 60 to 100 km for which we need to assume typical values for electron density, ion density and mean ion mass, neutral density and neutral temperature and their variation with height and in a course of a year.

We assume the electron density given in the International Reference Ionosphere (IRI2012) model (Bilitza 2001) and the neutral density and temperature obtained from the MSISE model (NRLMSISE-00 Picone *et al.* 2002). For all calculations, the temperature of each constituent is assumed equal to the neutral temperature, which is a good approximation because the number densities of neutrals are high and therefore also their collision rates with the other constitutes. In the following, we discuss how different parameters influence the spectrum.
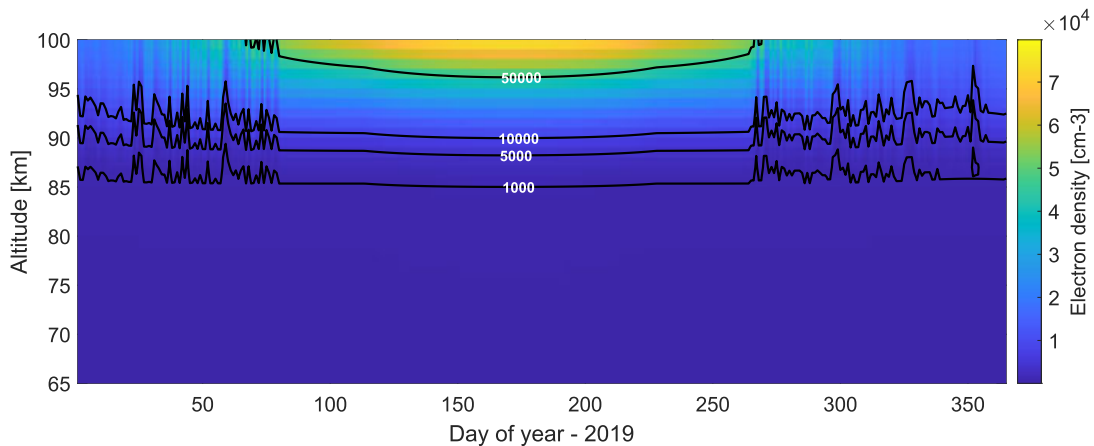
FIGURE 4. The electron density (cm^{-3}) above EISCAT location at noon (UTC) obtained from the IRI model (Bilitza 2001). The colour scale gives electron number densities, lines of constant number densities are superimposed with lowest line describing EISCAT VHF approximate detection limit.

4.1. *Electron background conditions*

The number of electrons present at the altitudes in question is an important parameter because it determines the strength of the signal and signal to noise ratio (SNR) and hence accuracy and the quality of the measurements. To resolve plasma parameters, small SNRs require a longer integration time, which on the other hand, is limited by the variation of the ionosphere with time. To find typical values, we consider the electron density from the IRI model (Bilitza 2001) at noon (UTC) for each day of the year of 2019, shown in figure 4 at altitudes 65 to 100 km. UTC time was chosen due to variation in local time between summer and winter and noon UTC time is quite close to the maximum background electron density values during the day. The figure includes a few contour lines describing equal electron densities. One can see that for most of the days, the electron density below 85 km, is less than 10^9 m^{-3} or 1000 cm^{-3}, which is a typical limit for studies with the EISCAT VHF. The year 2019 for which we selected the parameters is close to the solar minimum, so that we here consider the more challenging conditions of small electron content in the D-region. It is important to note that chances to measure spectra differ during disturbed conditions that occur for example during high solar activity. During certain times, the number of free electrons can increase by several orders of magnitude (Turunen 1993; Schlegel 1995) so that radar signals can be obtained from heights as low as 60–70 km; as for instance, one study of the D-region spectrum mentioned above covered heights of 70-92 km (Hansen *et al.* 1991).

4.2. *Temperature and neutral density*

The temperature and the density of the neutrals in the D-region vary considerably throughout a year and with altitude and their influence on the spectrum is significant. The global atmospheric circulation causes an up-welling of air at high latitudes during summer and downward motion during winter in the mesosphere. As a result the densities below 90 km are higher in summer and diminished in winter; and the motion is associated with low temperatures in summer and warmer temperatures in winter. The temperature variations at altitudes 60–100 km over one year are displayed in figure 5(*a*). These data are from the IRI2012 model (Bilitza 2001) at noon UTC for the year 2019 at the EISCAT VHF location. One can see a cold minimum during the summer months reaching down to 140 K and the warmer winter months with temperatures exceeding 200 K.
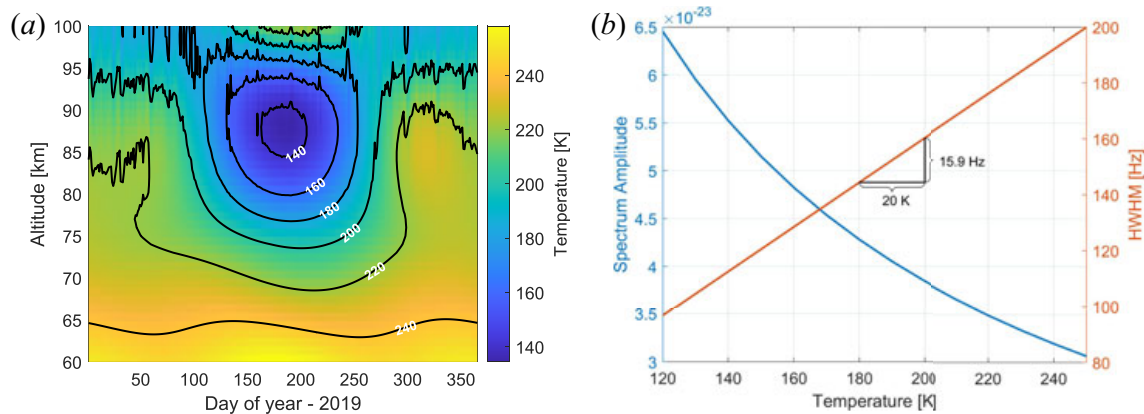
FIGURE 5. Temperature from the IRI model (Bilitza 2001) for EISCAT location at noon (UTC) and year 2019 on the left and corresponding variation of the spectrum at 85 km altitude shown for the amplitude (blue line) and width (orange line) on the right.
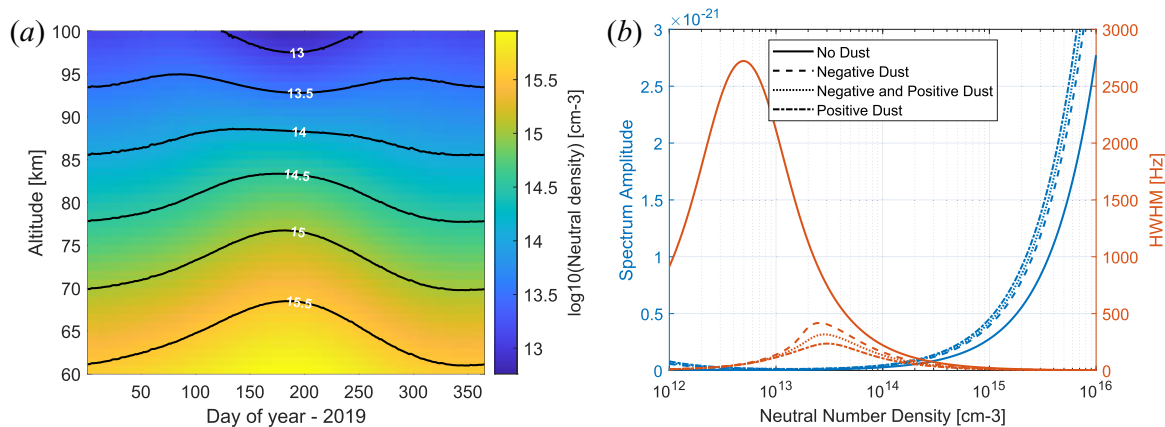

FIGURE 6. Neutral density from the NRLMISE-00 model for EISCAT location at noon (UTC) and year 2019 on the left and corresponding variation of the spectrum at 85 km shown with the spectral amplitudes (blue lines) and widths (orange lines) on the right calculated without dust and including different charged dust components as explained in the text.

The variation of the incoherent scatter spectrum with these temperatures can be seen in figure 5(b), which gives the corresponding variation of the spectral amplitude and width. One can see that the spectral amplitude increases with decreasing temperature while the width of the spectrum decreases. Increasing the temperature by for example 20° K reduces the spectral width by approximately 16 Hz, which also shows how temperature estimates influence the interpretation of the results.

Figure 6(a) shows the neutral density at 60–100 km altitude and noon UTC from the NRLMSISE-00 model (Picone *et al.* 2002) during the year 2019. As can be seen, the density strongly varies from winter to summer, especially for the lower altitudes by almost a factor of 10 (not the log scale). An exception is the highest considered altitudes (above 95 km ca.) where the density is lower during the summer months compared with spring/autumn and a bit higher during the main winter months. Figure 6(b) shows the variation of the calculated spectrum for those conditions. The spectral amplitude increases with increasing neutral density. The spectral width initially increases with increasing neutral density and then decreases. The increase in the width is only for very low neutral density at the limit of our model calculations for summer conditions. For the
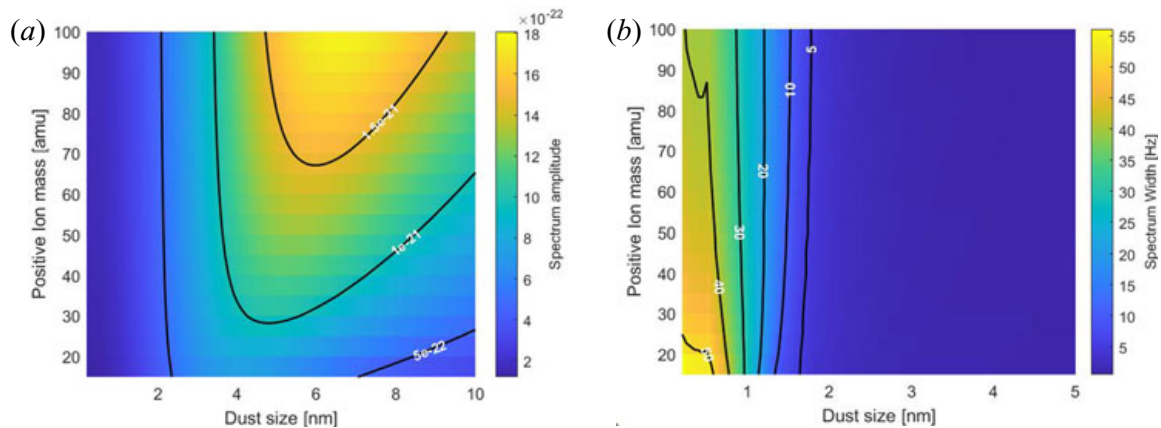
FIGURE 7. The variation of spectral amplitude (*a*) and spectral width (*b*) for different ion masses and dust radii.

winter conditions the spectrum only narrows for increasing altitude and decreasing neutral density.

4.3. *Positive and negative ions*

The composition of ions, both positive and negative, is more complicated in the mesosphere. This is especially true for the altitudes below around 80 km where negative ions start to appear. The inclusion of negative ions adds another complication to the derivation of the spectrum. For one, the ions are negatively charged due to attachments to electrons causing a depletion in the electron density, an important factor to have in order to detect strong enough signals from radars. And secondly, the negative ions cause a widening of the spectrum thus for spectrum calculations below 80 km the dust influence would seem diminished due to negative ion presence. Thus, investigating the spectrum below 80 km, is challenging both in terms of the observations as well as with regard to interpretation of the results.

For comparison, the main ion components at 80–100 km are $O2+$ and $NO+$ (with some variations during season). Since their masses are 30 and 32 amu respectively and their electron recombination rates are also similar, the variation in the ions mass is not so significant at these altitudes (see, e.g. Strelnikova *et al.* 2007; Friedrich *et al.* 2011). While the presence of large positive ions, for example water clusters, would cause the mean value of the positive ion mass to increase and influence the spectrum.

Figure 7(*a*) shows the change in the amplitude of the spectrum for dust radii ranging from 0.2 to 10 nm and ion masses from 20 to 100 amu. One can see that for sizes of dust up to around 5 nm the ion size does not influence the resulting spectrum but for larger sizes of dust the spectrum becomes higher for the larger ion sizes (this is only including positive ions). In figure 7(*b*) the changes in spectral width are shown for dust sizes 0.2 to 5 nm and for the same variation in the ion mass. Here, we can see that for small ion mass the width is broader than for the largest sizes by approximately 15 Hz thus the largest ion sizes would cause a narrowing in the spectrum compared with the smallest. And since the main ion mass above 80 km is considered to lie in the 31 amu range we can see that at lower altitudes where the ion mass might be larger since the composition is more complex that the spectrum might be more narrow and interfere with the narrowing caused by the dust particles. This is, however, mostly true for the smallest particles. For the largest dust particles the width of the spectrum is less variable. In summary, we note that the change in molecular compositions and resulting mean ion mass influences the spectrum, however, to a smaller extent than the temperature does.
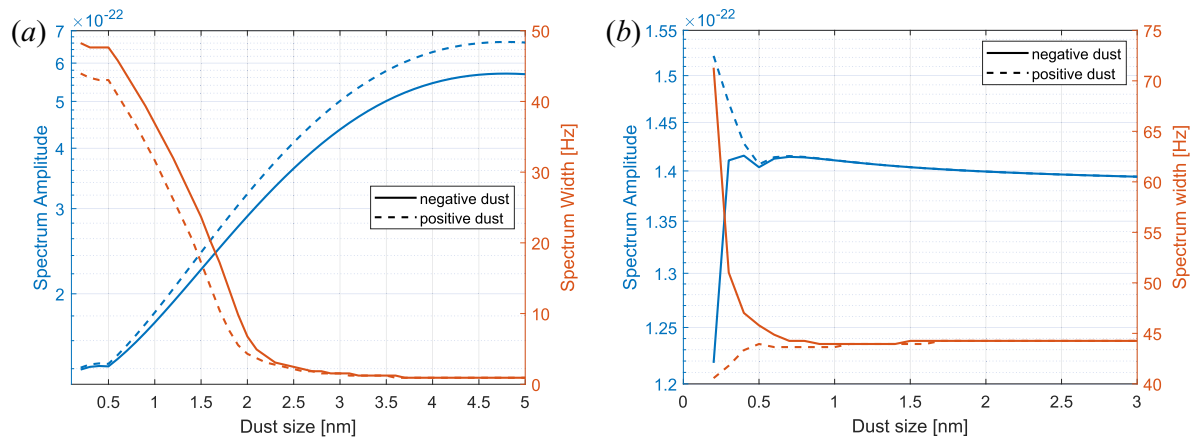
FIGURE 8. The spectral amplitude (blue) and spectral width (red) for positive (dashed lines) and negative (solid lines) dust particles with varying dust sizes shown in (*a*). Both negative and positive dust have number density of 500 cm^{-3} in respective cases. In (*b*) the amplitude and width is shown for varying dust sizes but the number density is kept such that the total mass for each particle size is the same. The number density used for each dust size is shown in figure 21 in Appendix B.

4.4. *Dust conditions*

MSPs are thought to reside at altitudes around 60–100 km, with larger and fewer particles at lower altitudes and more abundant and smaller particles higher up. There is a strong indication that a fraction of the dust is electrically charged, and this portion of the dust is the one that theoretically can be detected with radar backscatter. The most important consideration in detecting the dust is the number of free electrons, too low density and the signal detected by the radar will not exceed the noise level. Too high electron content compared with the dust density and the dust will 'disappear' and thus not be detected. For the current EISCAT radar a number density of $1e9$ m^{-3} would be the absolute minimum for a good enough signal. Now for the dust density, that too needs to be in adequate numbers to be detected. Which we will examine here in more detail.

In order to investigate the distribution of MSPs in the atmosphere several authors have used atmospheric modelling. The earlier models mainly made one-dimensional (1-D) model calculations but thus disregarded the atmospheric circulation (Hunten *et al.* 1980; Megner *et al.* 2006). The dust distributions on a global scale, were studied in 2-D models that include the atmospheric circulation and some particle micro-physics. The results show that dust distributions are different in the equatorial regions and at the high latitudes (Bardeen *et al.* 2008; Megner *et al.* 2008).

These differences in the distribution result from the influence of the global atmospheric circulation and the polar vortex at high latitudes which includes the EISCAT location considered here. The absolute number densities differ between different models, but are in a similar range as those obtained with the 1-D model, i.e. of the order of 1000 particles cm^{-3} between mesopause and middle stratosphere (Hunten *et al.* 1980). For the discussion here, we choose the number density model with largest variation between winter and summer conditions which we take from Bardeen *et al.* (2008).

4.4.1. *Dust size, number density and bulk density*

The spectrum varies greatly with dust size and different combinations of dust sizes will influence in a different way. In figure 8(*a*) the amplitude of the spectrum is shown for both positive and negative dust particles with radii from between 0.2 and 10 nm. The number
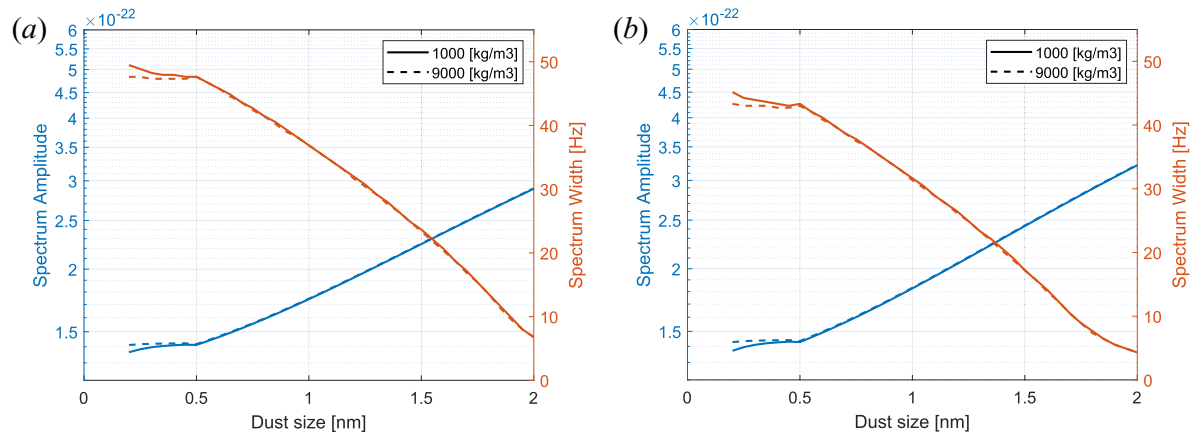
FIGURE 9. Variation in the spectrum amplitude and width for two different bulk densities of dust, 1000 and 9000 kg m^{-3} respectively. Dust number density kept at 500 cm^{-3} and electron density at 5000 cm^{-3} while the positive ion density was varied to keep charge neutrality. (*a*) Negative dust and (*b*) positive dust.

density for the positive dust and the negative dust was kept the same, at 500 cm^{-3}, while the electron and ion densities were varied to keep charge neutrality. For the negative dust the electron density was 5000 cm^{-3} and the positive ion density was at 5500 cm^{-3}. For the positive dust the number densities for the electrons was the same and for the positive ions the number density was at 4500 cm^{-3}.

The figure indicates that the presence of positive dust has a larger influence on the spectrum than negative dust; for both the amplitude and the width of the spectrum. This results from both the charge neutrality condition we keep, making the positive ion density lower by 1000 cm^{-3} compared with the negative dust case as well as the fact that positive dust particles always cause a narrowing of the spectrum as while the negative dust causes a broadening for dust particles smaller than approximately 1 nm. This can be seen in figure 8(*b*). Here, the dust number density is varied for each size of dust so that the total mass of dust used in the calculations is kept constant. Thus for 3 nm dust size the number density is 1 cm^{-3} and this increases for decreasing size. The number densities used are given in figure 21 in Appendix B. Here, we can clearly see that for equal mass the width of the respective spectrum is narrowing for the positive dust while it is broadening for small dust sizes and narrowing for increased size. In figure 20 in Appendix B we give a 3-D figure for the variation of the spectrum with different dust size and densities.

As was previously mentioned the dust bulk density is unknown but has been suggested to be approximately 2–3 g cm^{-3} by several authors (Hunten *et al.* 1980; Megner *et al.* 2006; Bardeen *et al.* 2008) and these are typical values for silicate particles. We choose for the calculations 3 g cm^{-3} but the results are not so different for 2 g cm^{-3} as we will see here. A larger variation in the density could occur if the particles have an irregular porous structure. The spectrum equation (2.2) is dependent on the mass of the particles and to calculate this we need to assume spherical particles of a certain mass density, the particles are definitely not spherical but we assume the mass difference using this assumption is negligible.

Comparison of spectrum calculations for bulk density 1 and 9 g cm^{-3} (1000 and 9000 kg m^{-3}) for the dust particles is shown in figure 9 for both negative dust in (*a*) and positive dust (*b*), showing that, for both the amplitude and the width of the spectrum, the variation is very small for dust larger than 0.5 nm. The largest difference is for particles smaller than 0.5 nm, however, the difference is at most a few Hz for the width and thus
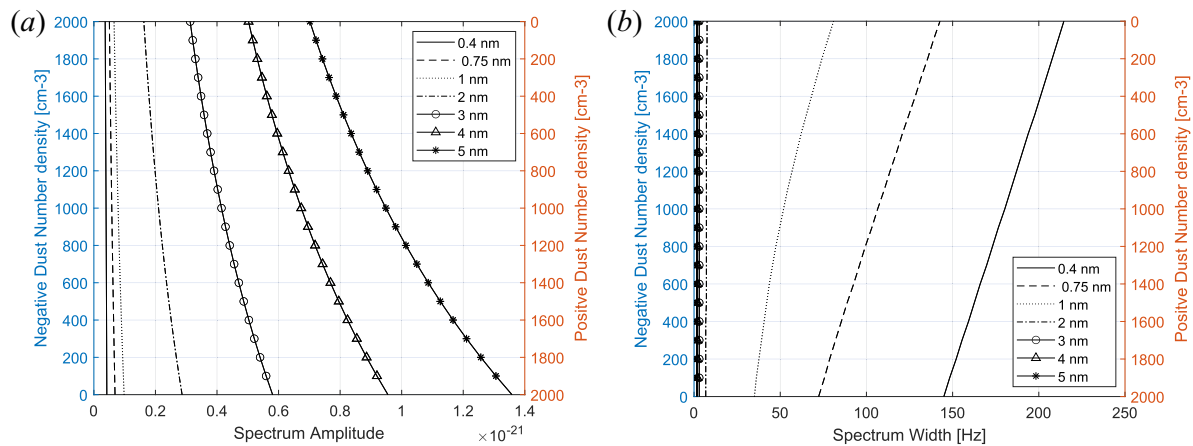
FIGURE 10. Spectral amplitudes and widths for selected cases of dust sizes: density of negative and positive dust particles is varied from 0 to 2000 cm^{-3} and 2000 to 0 cm^{-3}, respectively. (*a*) Spectral amplitude and (*b*) spectral width.

should not be influential in deriving the width from radar measurements except for cases with a very large number of small dust particles since the difference is also dependent on the number density of dust.

4.4.2. *Amount of charged dust and charge balance*

The amount of dust that is charged is a subject of debate and largely depends on the charging model assumed. The results either conclude on approximately 6 % of the particles being charged or close to 100 % (Rapp *et al.* 2007; Baumann *et al.* 2015; Plane, Feng & Dawkins 2015). This, however, is highly unlikely since allowing all the dust to become charged would in some cases remove all the free electrons from the D-region (Baumann *et al.* 2015), which is especially true for the higher altitudes where the smallest dust sizes are assumed to be most abundant and could equal the number of free electrons present (Megner *et al.* 2006, 2008).

Now the positive and negatively charged dusts influence the spectrum in different ways. This is due to the charge neutrality requirement we impose on the calculations, so that increasing the amount of positive dust would either increase the number of electrons or decrease the number of positive ions for example. In figure 10, the spectrum amplitude and width are shown for varying number density of negative and positive dust particles. So the electron density is kept constant and the dust particles are varied from 0 to 2000 particles cm^{-3} for negative dust and from 2000 to 0 cm^{-3} for the positive dust, so that the total number density of charged dust is kept constant at 2000 cm^{-3} while the ratio of number of negative particles to positive particles is varied.

One can see a stronger influence of the positive dust particles on the spectrum compared with the negative dust particles. The larger dust more influences the amplitude while the smaller dust particles influence the width and cause a narrowing of the spectrum. The narrowing of the spectrum could be more easily noted in the spectrum, because most of the other parameters broaden it.

We base our considerations of the influence of different number densities of charged dust on results obtained by Baumann *et al.* (2015) who combined an ionospheric chemistry model (Sodankylä Ion-Neutral Chemistry (SIC) model) and the MSP distribution modelled by Megner *et al.* (2006) to study the influence of MSPs on the D-region charge balance. They found large differences in the charging conditions between positive and negative dust particles and strong diurnal variations. The negative particles showed a rather

large number density during night at approximately 80–100 km due to effective electron attachment. The positive dust particles were most abundant during daytime at low altitude (55–75 km) and they were less abundant at night when they were located at higher altitude (up to 90 km) (see figure 22). This distribution poses several problems.

First, the negative dust particles mainly occur during night when electron densities are already low. Secondly, they form via electron attachment which further reduces the electron density. Figure 4 displays the noon variation of electrons from a solar minimum year and the electron density could be even further depleted in the presence of dust. From this we conclude that observational studies during the night are difficult, because the electron densities are low and therefore the SNR of observed spectra would not be optimal. As discussed above, positive dust particles would reduce the width of the spectrum to a larger degree than negative particles which could better be distinguished from the influences of other parameters. The conditions leading to positive charging of dust are, however, according to Baumann *et al.* (2015) best during the day at very low altitudes. The dust particles tend to be larger at low altitudes, making the detection even more promising, but the electron density is very low and even during the day often below the detection limit. The number of positively and negatively charged MSPs increases with an increased number of free electrons (Baumann *et al.* 2015) caused, for example, by incoming photons or precipitating particles. Thus, a disturbed ionosphere with a high number density of electrons during daytime at low altitudes would be optimal.

5. Variations of the spectrum during the day and during the year

To investigate in detail observation conditions above the EISCAT site, we first carry out a case study regarding variation within 24 hours and then simulate spectra for ionospheric parameters varying over a year.

5.1. *Case study – September conditions*

The dust size and density distributions in the mesosphere are determined by transport and collisional growth in the neutral atmosphere (e.g. Hunten *et al.* 1980; Megner *et al.* 2006; Bardeen *et al.* 2008). The number of charged particles is determined by sunlight and ionospheric conditions,including ion chemistry reactions as simulated in a model by Baumann *et al.* (2015), which includes the dust distribution by Megner *et al.* (2006).

We take the combined results for these two models as input to simulate the incoherent scatter spectrum. For comparison, we also simulate the spectrum in the absence of dust, assuming the parameters from the same model calculations done by Baumann *et al.* (2015). For the background parameters we use the NRLMISE-00 atmospheric model (Picone *et al.* 2002) for the temperature and neutral density for the same time period as the data from Baumann *et al.* (2015), 24 h data for 7–8 of September 2010.

The calculated spectrum amplitude and width during these 24 hours are presented in figure 11 using negative and positive dust densities (shown in figure 22 in Appendix B). The dust particles were mostly negatively charged during the night and at high altitudes and mostly positively charged at low altitudes during the day; some positively charged dust is also found at higher altitude during night (figure 22). We calculated the spectra for these dust parameters and compared the results with those obtained without dust.

Figure 11(*a*) displays the amplitudes relative to amplitude without dust and in (*b*) the spectrum width for the no dust case is shown relative to the dust case. The strongest influence on the amplitude and on the width can be seen at lower altitudes, mainly during daytime. Here, the width seems to narrow much more for the dust case compared with the no dust case, i.e. up to approximately 40 times. Thus conditions to detect charged dust in this particular case would be best during the day and at altitudes of approximately
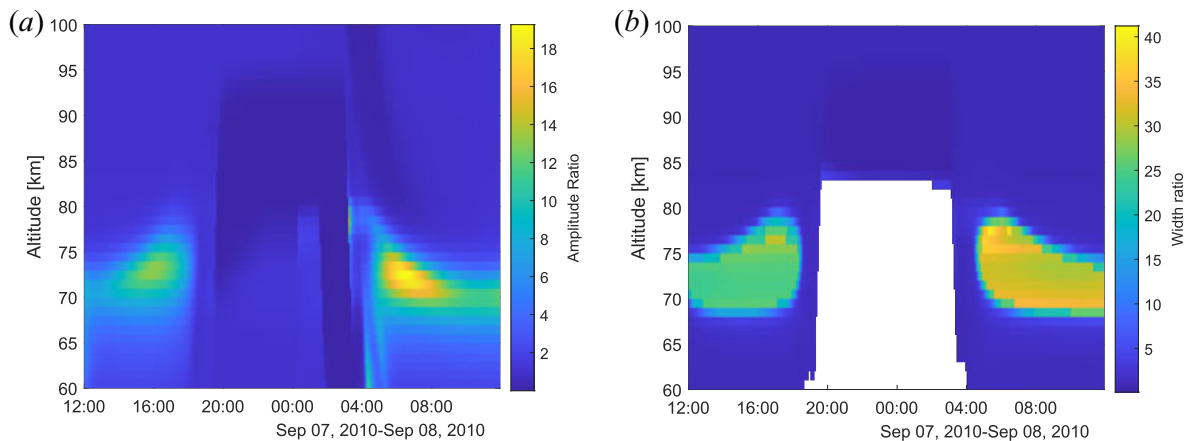
FIGURE 11. Spectrum amplitude ratio for dust to the no dust case shown in (*a*) and ratio of the width in (*b*) for no dust to the dust case; using values from noon to midnight 7–8 September 2010. White area depicts times and altitudes when the electron density is much lower than the dust density.

70–80 km. Looking at the ratio of positive dust to positive ions given in figure 24(*b*) there are similarities in the altitude range and time for when the amplitude and width are very influenced by the charged dust.

Note that the conditions below 80 km at night are not included in figure 11(*b*). This is because the electron density is very low, up to 300 times lower than the negative dust density, and hence the radar signal would be below the detection limit (see figure 24(*a*) in Appendix B). The charged dust would make the spectrum very narrow, however, so this time period could be considered for future radar observations if the electron density would be sufficiently enhanced above the radar detection limit.

According to Baumann *et al.* (2015) the presence of dust changes the D-region charge balance and the relative magnitude of each constituent present. Thus the data used here for the dust case and the case without the dust do not correspond in electron density or the amount of positive or negative ions. Thus, for radar observations it would be beneficial to run similar model calculations on the charge state to get the most accurate results on the relative narrowing of the spectrum.

5.2. *Variation of the spectrum during the year*

We now consider all parameters discussed above to investigate the variation of the spectrum during a year. To calculate the spectra, we used two different dust size distributions from Baumann *et al.* (2015): one at 80 km during the day (noon) where positive and large dust particles are more abundant and one at 90 km where small and negative particles are more abundant, the distributions are shown in figure 12. The total number densities of the dust are from Bardeen *et al.* (2008) for average summer dust number densities which are smaller than their average winter values. We assume that 6 % of this total dust number density is charged with values used given in table 2. We then calculate the spectrum for the altitudes 80 km and 90 km using model assumptions for electron densities and relative ion composition from the IRI model (Bilitza 2001) (figure 4) and the neutral density (figure 6) and temperature (figure 5) from the NRLMISE-00 model (Picone *et al.* 2002).

First, we present calculations for 90 km altitude in figure 13, showing the amplitude of the spectrum (panel *a*) and the width (panel *b*). We compare spectra with dust (red dotted line) and without dust (the solid blue line). The electron density here is of order
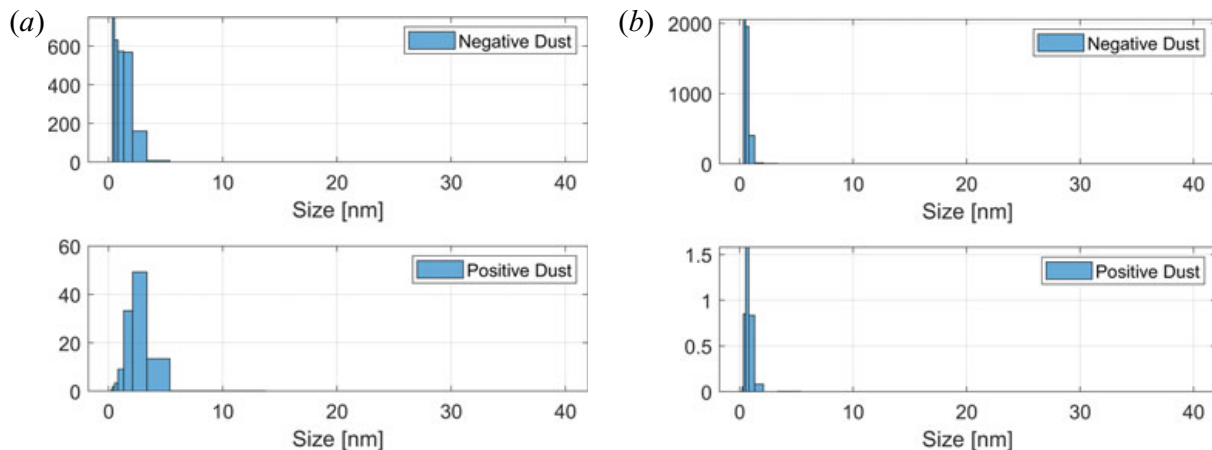
FIGURE 12. Size distributions of negative and positive dust particles, further explained in the text. (*a*) Dust number density in cm^{-3} at 80 km and (*b*) dust number density in cm^{-3} at 90 km. The top panel shows negative dust and bottom panel shows positive dust.

	80 km	**90 km**
Total	1.2733×10^4	4.1798×10^4
6 %	763.9866	2.5079×10^3
Negative dust	733.6855	2.5059×10^3
Positive dust	30.3011	1.9248

TABLE 2. Number densities (in cm^{-3}) of dust used in calculations of figures 13, 14 and 15 in § 4.2 where we have used a total of 6 % of the total dust density as charged dust for both 80 km and 90 km. The total number densities are from Bardeen *et al.* (2008), where we have used the average number densities for these altitudes for summer conditions (approximate). Number of negative dust vs. positive dust comes from the size distributions from Baumann *et al.* (2015) for 80 km and 90 km.

5000 cm^{-3} or more for most of the year (cf. figure 4) and therefore exceeds the total dust number densities that we considered. One can see that the dust increases the width of the spectrum. This is caused by the small dust particles that are largely dominant in the assumed size distribution (see figure 8). The charge neutrality condition is also important here, and we keep the electron density as given from the IRI model (Bilitza 2001) for the year 2019, while we vary the positive ions to keep the charge neutrality due to the increased negative dust particles.

Results for spectra at 80 km altitude are shown in figure 14. One can see that the amplitudes are much higher in the case when dust is included, while the spectral width is reduced. This is because the large dust particles included here lead to a more narrow spectral width, as mentioned above. This result, however, describes a case that because of low electron density cannot be observed, or at least not with the systems we are aware of. For the sake of investigating the spectra, we now assume an enhanced electron density (∼90 km) for otherwise 80 km conditions.

In such a case, the amplitude difference between the dust and no dust cases is largest during the summer. The differences in the width of the spectra are most pronounced during the winter while the summer spectra do not much differ between the cases with and without dust where both spectral widths are quite narrow due to the cold
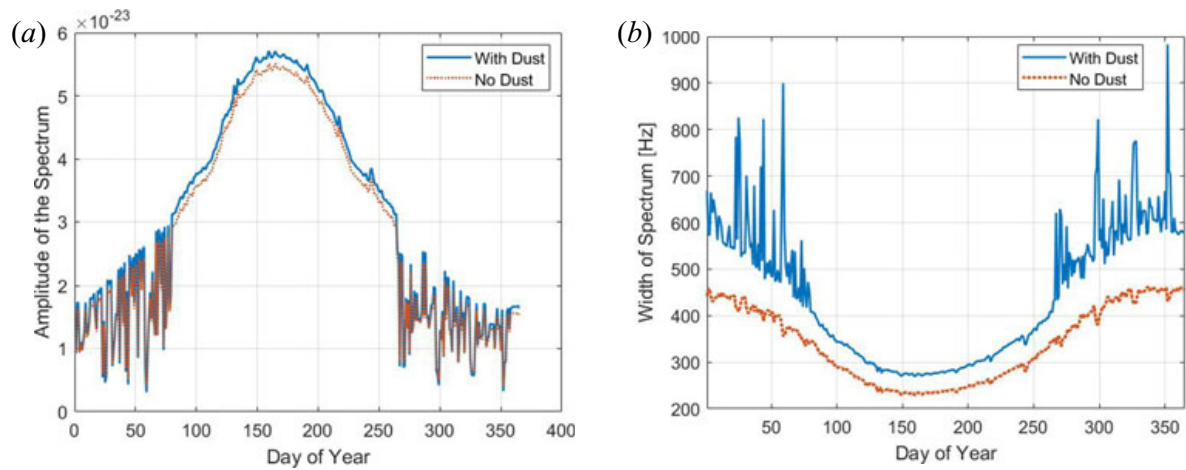
FIGURE 13. Amplitude and width for spectrum calculations for altitude of 90 km and a dust number density shown in figure 12(*a*). (*a*) Spectrum amplitude and (*b*) spectrum width.
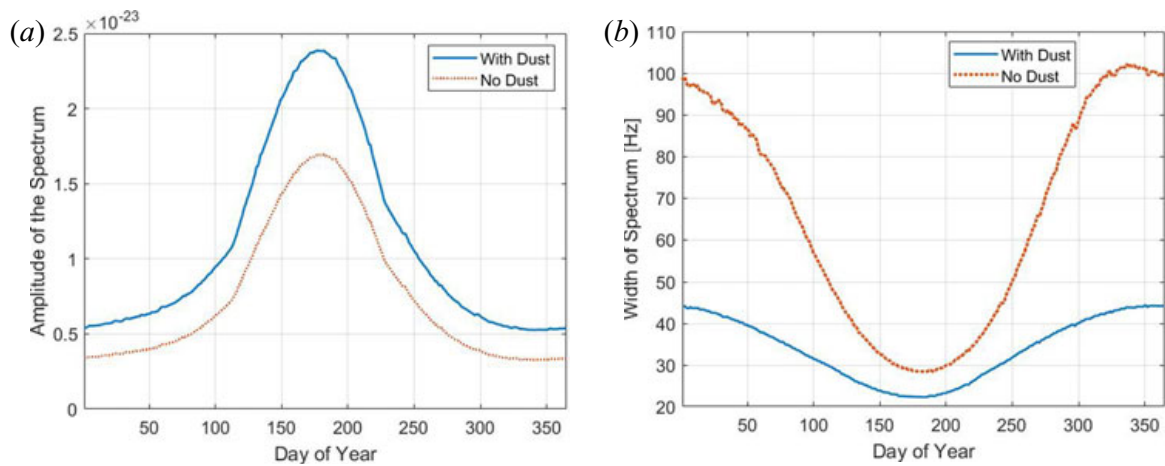

FIGURE 14. Amplitude and width for spectrum calculations for altitude of 80 km and a dust number density shown in figure 12(*b*). (*a*) Spectrum amplitude and (*b*) spectrum width.
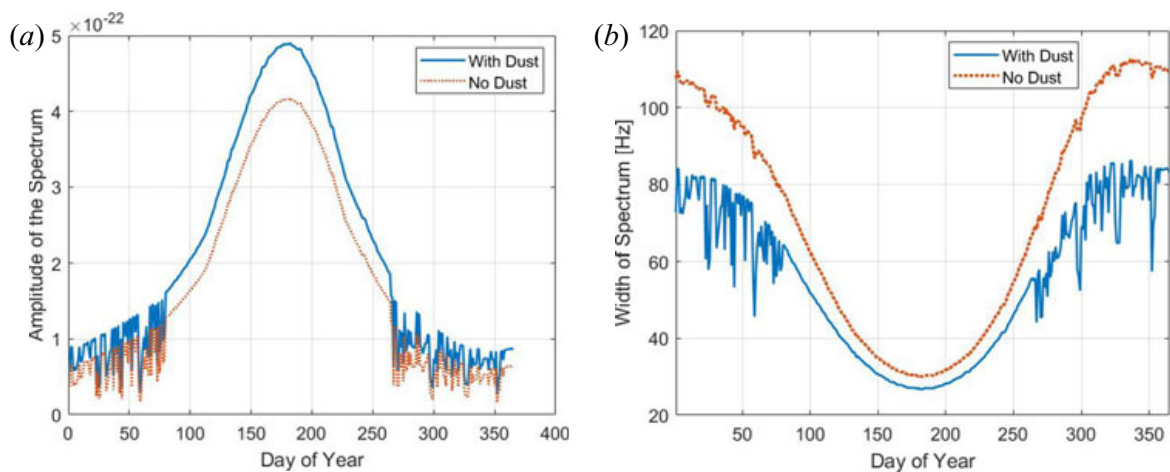

FIGURE 15. Amplitude and width for spectrum calculations for altitude of 80 km with electron number density from 90 km and a dust number density shown in figure 12(*a*). (*a*) Spectrum amplitude and (*b*) spectrum width.

mesospheric temperatures. The presence of charged dust in both cases narrows the spectra at 80 km and variations during the year are less pronounced than they are without dust. The spectral width is approximately 20 % narrower during the winter months, which corresponds well to the discrepancy found by Hansen *et al.* (1991) for similar altitudes under enhanced electron density conditions.

Note that, during winter, the electron density in the IRI model (Bilitza 2001) fluctuates from day to day and because of this all calculated parameters shown in the figures fluctuate during the winter months, i.e. roughly the first and the last 90 days of the year. The cyclic nature of the curves, easy to see in the red curve representing the no dust scenario, can mainly be attributed to the background variations. For example, the temperature being higher in the winter which produces a wider spectrum while a lower temperature narrows the spectrum; this is also the case for the temperature minimum of the summer mesosphere. The spectrum is also broader because of a typically higher neutral and electron density during summer, which is due to up-welling of air at the northern pole (polar vortex). We point out that investigations during summer at mid and high latitude can be further complicated by the formation of strong coherent radar echoes called polar mesospheric summer echoes (see e.g. Rapp & Lübken 2004) The cold temperature in the mesosphere during the summer causes large ice particles to form in the altitude range 80–90 km, using dust as condensation nuclei. These can become charged and turbulence causes structures in these charged ice particle clouds that cause large electron density gradients and subsequently powerful coherent radar echoes. The presence of these coherent radar echoes would make it difficult to detect the much weaker incoherent radar signal.

6. Summary and conclusions

We investigate the incoherent scatter from the D-region ionosphere taking into account the influence of charged dust particles. The model is based on the previously used fluid description of a weakly ionized plasma and charged dust (Cho *et al.* 1998). In our calculations we include dust particles with a size distribution and, different from previous works, we include also different charge states of the dust. We show that the charge number has a strong influence on the spectra for large particle radii. However, based on present understanding of the dust charging in the ionosphere, we expect the dust particles to be typically singly or at best doubly charged; in this case the differences are not so strong for particles in the smaller size range, which are the dominant sizes in the D-region, excluding conditions favouring ice particle formation in the summer mesopause.

While the backscatter cross-section does not change with the charge polarity of the dust, we find that the spectra strongly differ between the positively and negatively charged dust particles. This is because they contribute in different ways to the charge balance. Positive dust particles are easier to detect because they are associated with a decrease in the ion component. The lack of ions narrows the spectrum so that the influence of the charged dust becomes more apparent.

We discuss the dusty plasma conditions and show that it is valid in the D-region ionosphere for all conditions we considered here. We find, however, that it is hard to derive information on charged dust from observed spectra for a number of reasons.

We consider the conditions at the EISCAT VHF radar with 224 MHz transmit frequency and find that the spectrum can narrow due to the presence of dust by up to 50 Hz (HWHM). The positive dust particles influence the spectrum more strongly than negative dust particles and we find high dust number density to be quite important. Models predict higher numbers of large positive dust particles during the day at lower altitudes as opposed to during the night (Baumann *et al.* 2015).

Conditions are more favourable for dust detection during the winter compared with summer conditions, mainly because in the winter mesosphere we expect higher temperature, lower neutral density and higher dust number density (Megner *et al.* 2006). The electron density during observations needs to be high enough so that the SNR of the measurements is sufficient to analyse the spectra. This latter requirement is somewhat in contradiction to the best spectra being expected at low altitude. A target condition to search for dust signatures in the spectra is therefore during special ionospheric conditions when the electron content is large below 80 km. We will consider these results to choose the most suitable observational data and observation conditions in future work.

In summary we see that the spectra depend on a number of different parameters. It would therefore be helpful to derive some parameters independently from other observations along with any radar measurements in order to accurately determine the spectrum and distinguish the dust signatures from those of the other parameters.

Both the temperature and the density of the neutral atmosphere can influence the spectrum in various ways. Temperatures vary a lot throughout a year and also locally and with height; a 20 K temperature change can alter the width of the spectrum by almost 20 Hz. Independent temperature and neutral density observations can be made using LiDAR (Light Detection and Ranging, cf. Nozava *et al.* 2014). Additional electron density measurements can be made using ionosondes. *In situ* observations with rockets can provide independent information at a given time and location on the charge and size distributions of dust, on the neutral density and on the neutral temperature.

To carry out this study, we have developed a code to calculate the incoherent scatter spectrum, including a set of size bins for charged dust particles; different from and extended from previous codes, we include dust components with different charge numbers. The code is open access at the repository of UiT, Arctic University of Norway (see Appendix C).

Declaration of interest

The authors report no conflict of interest.

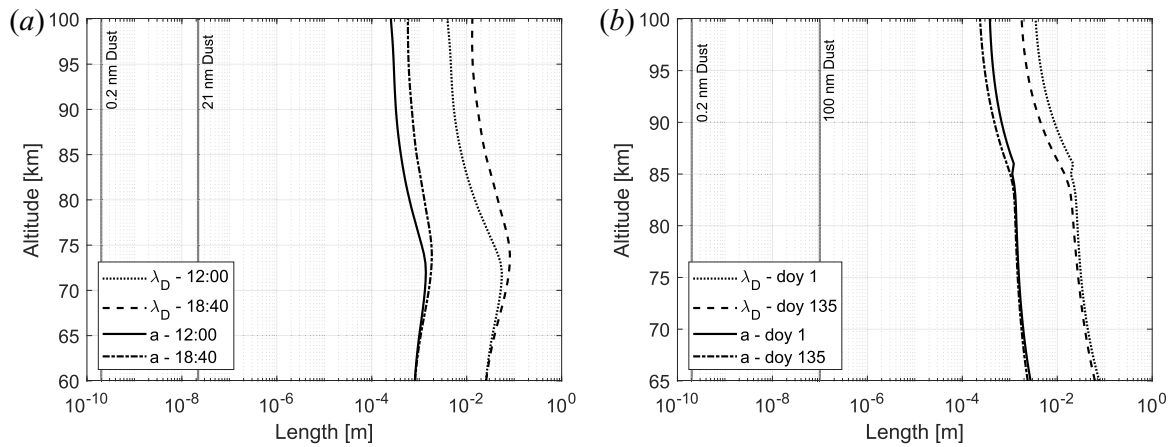## Appendix A. Dusty plasma conditions

FIGURE 16. The figures show dust sizes, mean distance between plasma particles a and plasma Debye length λ for conditions used in the case studies for September conditions in (*a*) and two days in 2019 (*b*). One can see that the relation $r_d \ll a < \lambda$ is always valid. It would hold even for large particles up to 100 nm. We approximate $a \propto N_e^{-1/3}$.
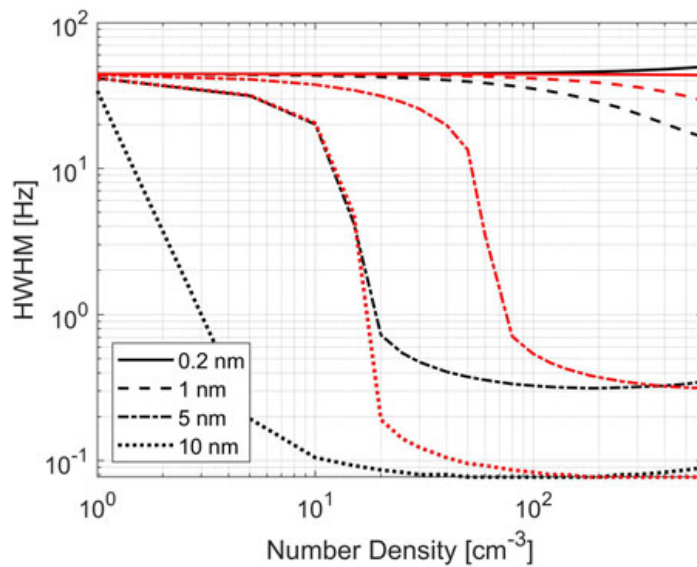

FIGURE 17. Spectral width (Hz) shown as a function of number density (cm^{-3}) for positive dust particles with two different charge numbers. Charge number $Z = 1$ is shown in red and $Z = 2$ is shown in black.
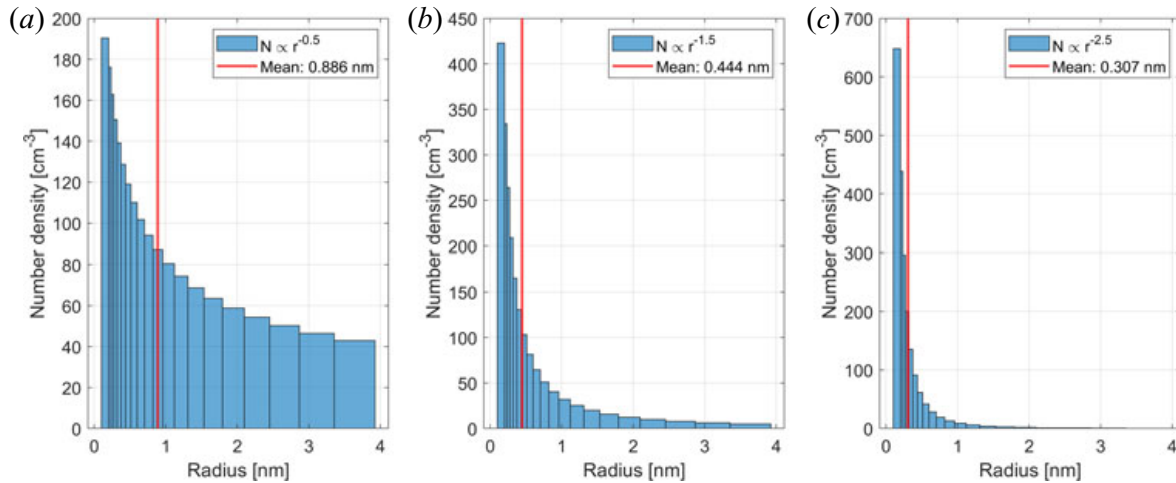
FIGURE 18. Dust size distributions with three different power laws, $r^{-0.5}$, $r^{-1.5}$ and $r^{-2.5}$, each with a total number density of 2000 cm^{-3}. The average size is marked in the histograms in red. We choose 20 size bins that are calculated from the initial size of 0.2 nm using a geometric distribution as the one used by Megner *et al.* (2006).
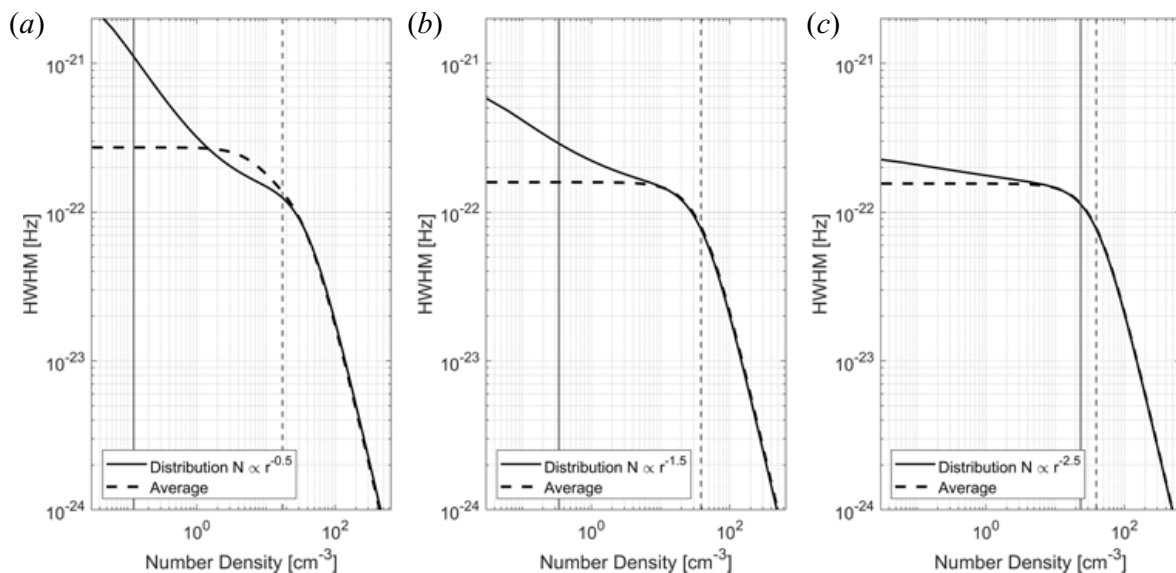
FIGURE 19. Spectrum shown for size distributions with different power laws given in figure 18. Shown here with the spectrum calculated for the average size for each respective distribution. The number density of electrons is 5000 cm^{-3} and total number density for dust is chosen as 2000 cm^{-3} of positive particles.

Appendix B. Supporting figures on D-region conditions

The spectrum varies with dust size but also the amount of dust for each size. Since we do not have an adequate amount of information on what size distributions we could expect at each time, we can get a closer look at how the spectrum varies for a certain dust size and with number densities. In figure 20 we show the amplitude and width of the spectrum for positive and negative dust and how each size varies with a respective number density. For negative dust, the amplitude and width in (*a*) and (*b*) are similar to the amplitude and width of the positive particles. The amplitude is higher for positive dust, especially for large sizes, and the width is broader for negative dust in the smaller size regime. Both positive and negative dust show a narrower spectrum for larger dust sizes. The negative
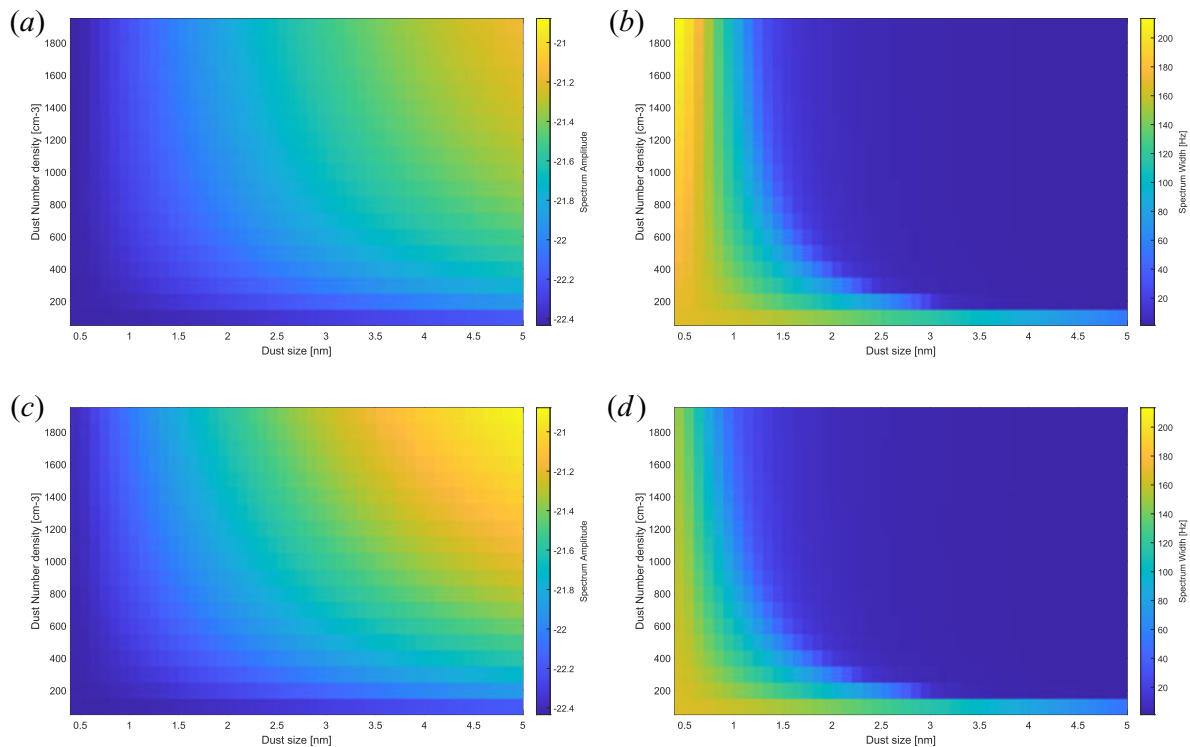
FIGURE 20. Spectral amplitudes and widths calculated for negative and positive dust particles, respectively, as a function of dust radius with radii ranging from 0.4 to 5 nm (horizontal axes) and as function of dust number densities from 50 to 2000 cm^{-3} given on the vertical axes. (*a*) Negative dust – amplitude, (*b*) negative dust – width, (*c*) positive dust – amplitude and (*d*) positive dust –width.
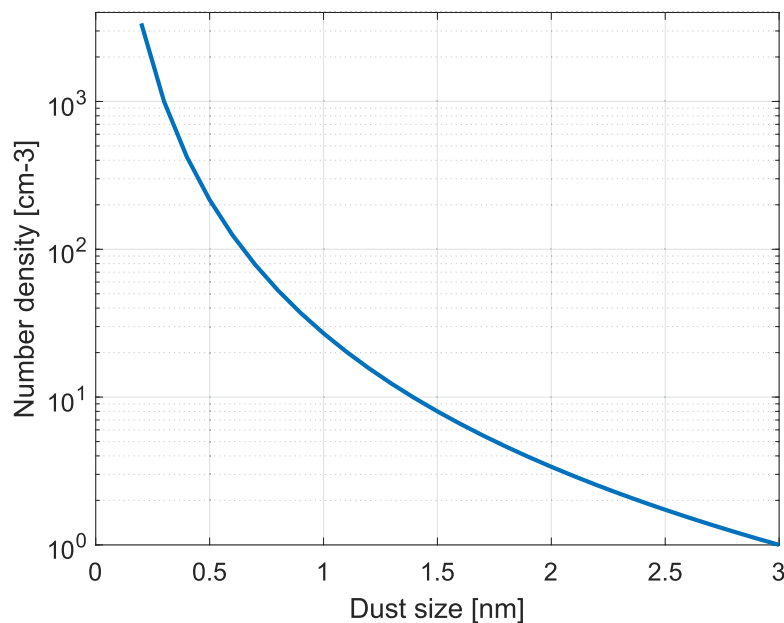

FIGURE 21. Dust number density in cm^{-3} used in figure 8.

particles also show that the widest spectrum happens for the smallest sizes and largest number densities. Both positive and negative particles show that, for vary small number densities, the spectrum is at its widest. This is interesting to note since for large dust sizes
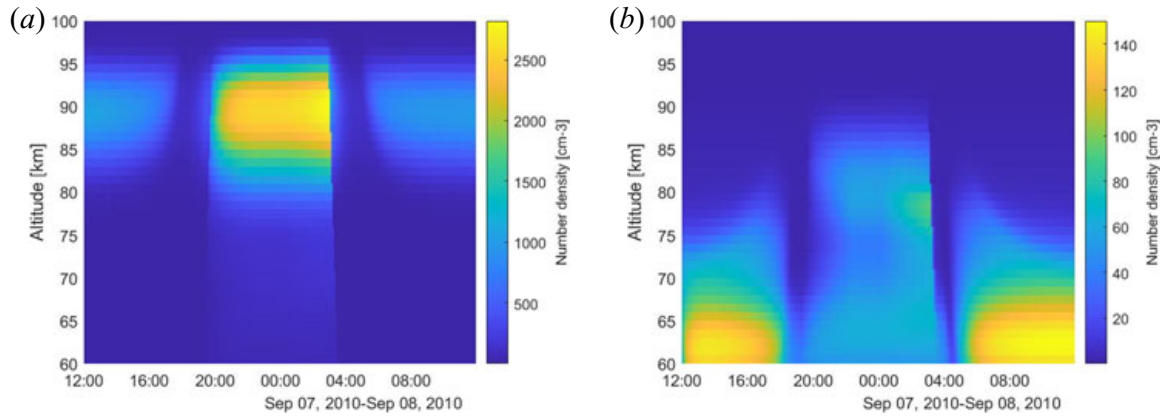
FIGURE 22. Number densities of charged dust for conditions from noon to midnight 7–8 September 2010; these are used for the model calculations presented in § 5.1 (from Baumann *et al.* (2015), courtesy of the author). (*a*) Negative dust density cm^{-3} and (*b*) positive dust density cm^{-3}.
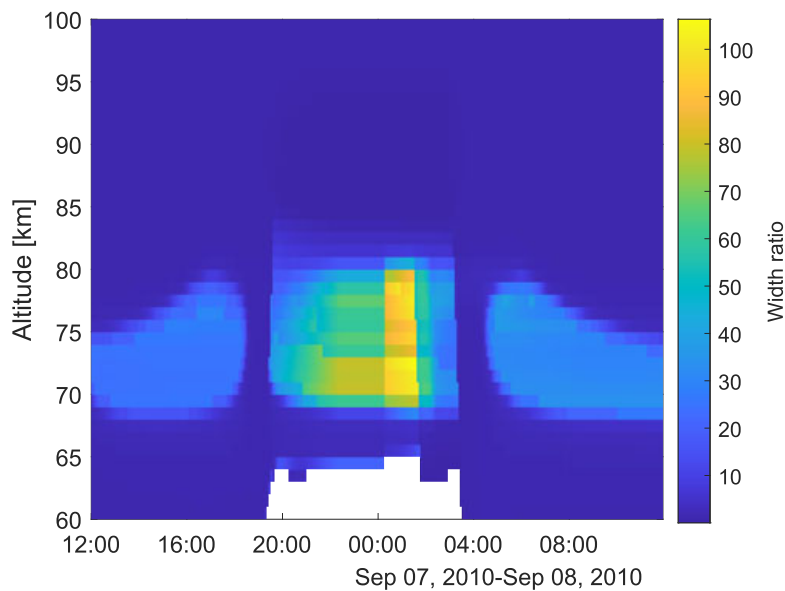

FIGURE 23. Spectrum width ratio calculated for the parameters used in the case study from § 5.1 where the smallest electron densities are included as well. Here, the ratio is the spectral width for the no dust case to the spectral width for included dust.
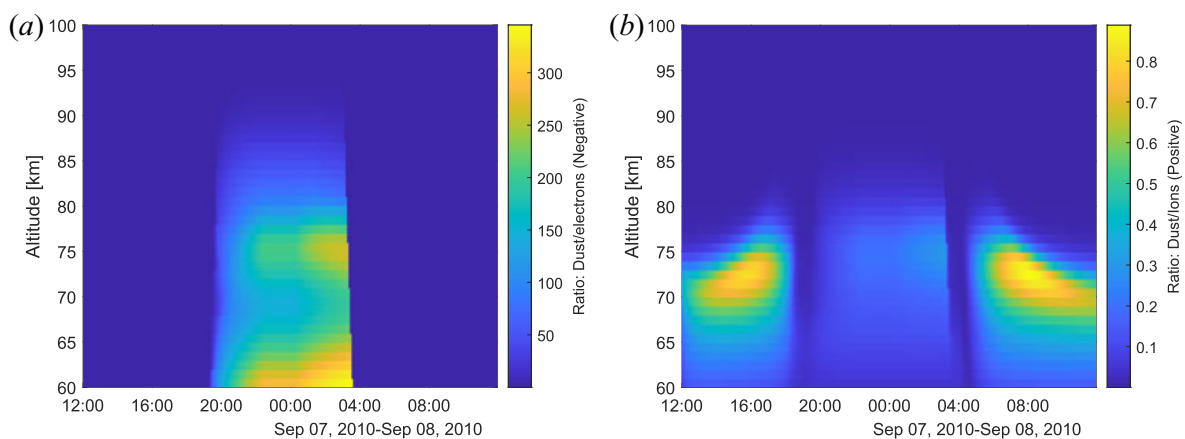

FIGURE 24. Ratio of the negative dust to electrons on the left and positive dust to positive ions on the right. Data from Megner *et al.* (2006) and Baumann *et al.* (2015) used in § 5.1.

the number density will most likely always be very small and thus its contribution to the narrowing of the spectrum is large even for just a few particles.

Dust number density for different sizes is shown in figure 21 where the total mass has been assumed the same regardless of size and the particles assumed to be spherical and have bulk density of $3000\,\mathrm{kg\,m^{-3}}$ and we choose the total mass to be the same as 1 particle of 3 nm size.

Number densities used in § 5.1 are shown in figure 22 with negative dust number densities on the left and positive dust number densities on the right. These data are from Baumann *et al.* (2015) and are courtesy of C. Baumann.

We include all the spectrum amplitudes, as well as those that are very low and have almost no electron density present, in figure 23, where we can see large narrowing in the spectrum during night for altitudes 70 to 80 km. This case, however, has electron densities almost 300 times smaller than the negative number density, as can be seen in figure 24(*a*), where we show the ratio of the negative dust particles to the electron density. The ratio of positive dust to positive ions is shown in (*b*) with the areas of largest difference corresponding well with areas of largest narrowing of the spectrum width shown in § 5.1.

Appendix C. Code

We have developed a code to calculate the incoherent scatter spectrum including a set of size bins for charged dust particles. The code is written in MATLAB. It was developed based on previous codes by Strelnikova (2009) and Teiser (2013) and includes, in addition to those previous codes, dust components with different charge numbers. The code is open access at the repository of UiT, Arctic University of Norway. It can be found at: https://doi.org/10.18710/GHZIIY.

REFERENCES

BANKS, P.M. & KOCKARTS, G. 1973 *Aeronomy - Part A*. Academic Press.

BARDEEN, C.G., TOON, O.B., JENSEN, E.J., MARSH, D.R. & HARVEY, V.L. 2008 Numerical simulations of the three-dimensional distribution of meteoric dust in the mesosphere and upper stratosphere. *J. Geophys. Res.: Atmos*. **113** (D17).

BAUMANN, C., RAPP, M., ANTTILA, M., KERO, A. & VERRONEN, P.T. 2015 Effects of meteoric smoke particles on the d region ion chemistry. *J. Geophys. Res.: Space Phys*. **120** (12), 10–823.

BILITZA, D. 2001 International reference ionosphere 2000. *Radio Sci*. **36** (2), 261–275.

CHO, J.Y.N., SULZER, M.P. & KELLEY, M.C. 1998 Meteoric dust effects on d-region incoherent scatter radar spectra. *J. Atmos. Sol.-Terr. Phys*. **60** (3), 349–357.

DOUGHERTY, J.P. & FARLEY, D.T.JR. 1963 A theory of incoherent scattering of radio waves by a plasma: 3 Scattering in a partly ionized gas. *J. Geophys. Res*. **68** (19), 5473–5486.

FENTZKE, J.T., HSU, V., BRUM, C.G.M., STRELNIKOVA, I., RAPP, M. & NICOLLS, M. 2012 D region meteoric smoke and neutral temperature retrieval using the poker flat incoherent scatter radar. *Geophys. Res. Lett*. **39** (21).

FENTZKE, J.T., JANCHES, D., STRELNIKOVA, I. & RAPP, M. 2009 Meteoric smoke particle properties derived using dual-beam arecibo uhf observations of d-region spectra during different seasons. *J. Atmos. Sol.-Terr. Phys*. **71** (17–18), 1982–1991.

FRIEDRICH, M., RAPP, M., PLANE, J.M.C. & TORKAR, K.M. 2011 Bite-outs and other depletions of mesospheric electrons. *J. Atmos. Sol.-Terr. Phys*. **73** (14–15), 2201–2211.

GOERTZ, C.K. 1989 Dusty plasmas in the solar system. *Rev. Geophys*. **27** (2), 271–292.

HAGFORS, T. 1992 Note on the scattering of electromagnetic waves from charged dust particles in a plasma. *J. Atmos. Terr. Phys*. **54** (3–4), 333–338.

HANSEN, G., HOPPE, U.-P., TURUNEN, E. & POLLARI, P. 1991 Comparison of observed and calculated incoherent scatter spectra from the d region. *Radio Sci*. **26** (5), 1153–1164.

HUNTEN, D.M., TURCO, R.P. & TOON, O.B. 1980 Smoke and dust particles of meteoric origin in the mesosphere and stratosphere. *J. Atmos. Sci.* **37** (6), 1342–1357.

KALASHNIKOVA, O., HORANYI, M., THOMAS, G.E. & TOON, O.B. 2000 Meteoric smoke production in the atmosphere. *Geophys. Res. Lett.* **27** (20), 3293–3296.

MANN, I., GUNNARSDOTTIR, T., HÄGGSTRÖM, I., EREN, S., TJULIN, A., MYRVANG, M., RIETVELD, M., DALIN, P., JOZWICKI, D. & TROLLVIK, H. 2019 Radar studies of ionospheric dusty plasma phenomena. *Contrib. Plasma Phys.* **59** (6), e201900005.

MATHEWS, J.D. 1978 The effect of negative ions on collision-dominated thomson scattering. *J. Geophys. Res.: Space Phys.* **83** (A2), 505–512.

MEGNER, L., RAPP, M. & GUMBEL, J. 2006 Distribution of meteoric smoke - sensitivity to microphysical properties and atmospheric conditions. *Atmos. Chem. Phys.* **6** (12), 4415–4426.

MEGNER, L., SISKIND, D.E., RAPP, M. & GUMBEL, J. 2008 Global and temporal distribution of meteoric smoke: a two-dimensional simulation study. *J. Geophys. Res.: Atmos.* **113** (D3).

MENDIS, D.A. & ROSENBERG, M. 1994 Cosmic dusty plasma. *Annu. Rev. Astron. Astrophys.* **32** (1), 419–463.

NOZAWA, S., KAWAHARA, T.D., SAITO, N., HALL, C.M., TSUDA, T.T., KAWABATA, T., WADA, S., BREKKE, A., TAKAHASHI, T., FUJIWARA, H., OGAWA, Y. & FUJII, R. 2014 Variations of the neutral temperature and sodium density between 80 and 107 km above Tromsø during the winter of 2010-2011 by a new solid-state sodium lidar. *J. Geophys. Res.: Space Phys.* **119**, 441–451.

PICONE, J.M., HEDIN, A.E., DROB, D.P. & AIKIN, A.C. 2002 Nrlmsise-00 empirical model of the atmosphere: statistical comparisons and scientific issues. *J. Geophys. Res.: Space Phys.* **107** (A12), SIA–15.

PLANE, J.M.C., FENG, W. & DAWKINS, E.C.M. 2015 The mesosphere and metals: chemistry and changes. *Chem. Rev.* **115** (10), 4497–4541.

RAPP, M. & LÜBKEN, F.-J. 2004 Polar mesosphere summer echoes (PMSE): review of observations and current understanding. *Atmos. Chem. Phys.* **4** (11/12), 2601–2633.

RAPP, M., STRELNIKOVA, I. & GUMBEL, J. 2007 Meteoric smoke particles: evidence from rocket and radar techniques. *Adv. Space Res.* **40** (6), 809–817.

ROSINSKI, J. & SNOW, R.H. 1961 Secondary particulate matter from meteor vapors. *J. Meteorol.* **18** (6), 736–745.

SCHLEGEL, K. 1995 Eiscat and the eiscat data base–a tool for ionospheric modeling (e-and d-region). *Adv. Space Res.* **16** (1), 147–154.

SCHUNK, R.W. 1975 Transport equations for aeronomy. *Planet. Space Sci.* **23** (3), 437–485.

STRELNIKOVA, I. 2009 Mesospheric aerosol particles: evidence from rocket and radar techniques. PhD thesis, Leibniz-Institute of Atmospheric Physics.

STRELNIKOVA, I., RAPP, M., RAIZADA, S. & SULZER, M. 2007 Meteor smoke particle properties derived from arecibo incoherent scatter radar observations. *Geophys. Res. Lett.* **34** (15).

TANENBAUM, B.S. 1968 Continuum theory of Thomson scattering. *Phys. Rev.* **171** (1), 215.

TEISER, G. 2013 Zum Einfluss von geladenen Aerosolen auf die inkohärente Rückstreuung von Radarwellen aus der oberen Mesosphäre. Master's thesis, Fachbereich Physik an der Mathematisch-Naturwissenschaftlichen Fakultät der Universität Rostock, Germany.

TURUNEN, E. 1993 Eiscat incoherent scatter radar observations and model studies of day to twilight variations in the d-region during the PCA event of August 1989. *J. Atmos. Terr. Phys.* **55** (4–5), 767–781.

VERHEEST, F. 1996 Waves and instabilities in dusty space plasmas. *Space Sci. Rev.* **77** (3–4), 267–302.

PAPER II

Modulation of polar meospheric summer echoes (PMSEs) with high-frequency heating during low solar illumination

Annales
Geophysicae

Modulation of polar mesospheric summer echoes (PMSEs) with high-frequency heating during low solar illumination

Tinna L. Gunnarsdottir[1], Arne Poggenpohl[1,2], Ingrid Mann[1], Alireza Mahmoudian[3], Peter Dalin[4], Ingemar Haeggstroem[5], and Michael Rietveld[6]

[1]Department of Physics and Technology, UiT The Arctic University of Norway, Tromsø, Norway
[2]Physics Faculty, TU Dortmund University, Dortmund, Germany
[3]Institute of Geophysics, University of Tehran, Tehran, Iran
[4]Swedish Institute of Space Physics, IRF, Kiruna, Sweden
[5]EISCAT Scientific Association, Kiruna, Sweden
[6]EISCAT Scientific Association, Ramfjord, Norway

Correspondence: Tinna L. Gunnarsdottir (tinna.gunnarsdottir@uit.no)

Abstract. Polar mesospheric summer echo (PMSE) formation is linked to charged dust/ice particles in the mesosphere. We investigate the modulation of PMSEs with radio waves based on measurements with EISCAT VHF radar and EISCAT heating facility during low solar illumination. The measurements were made in August 2018 and 2020 around 20:02 UT. Heating was operated in cycles with intervals of 48 s on and 168 s off. More than half of the observed heating cycles show a PMSE modulation with a decrease in PMSE when the heater is on and an increase when it is switched off again. The PMSE often increases beyond its initial strength. Less than half of the observed modulations have such an overshoot. The overshoots are small or nonexistent at strong PMSE, and they are not observed when the ionosphere is influenced by particle precipitation. We observe instances of very large overshoots at weak PMSE. PMSE modulation varies strongly from one cycle to the next, being highly variable on spatial scales smaller than a kilometer and timescales shorter than the timescales assumed for the variation in dust parameters. Average curves over several heating cycles are similar to the overshoot curves predicted by theory and observed previously. Some of the individual curves show stronger overshoots than reported in previous studies, and they exceed the values predicted by theory. A possible explanation is that the dust-charging conditions are different either because of the reduced solar illumination around midnight or because of long-term changes in ice particles in the

mesosphere. We conclude that it is not possible to reliably derive the dust-charging parameters from the observed PMSE modulations.

1 Introduction

Polar mesospheric summer echoes (PMSEs) are strong, coherent radar echoes observed from altitudes of 80 to 90 km at high and middle latitudes during the summer. It was first noted in the 1970s that these coherent radar echoes were unusually strong (Ecklund and Balsley, 1981; Czechowsky et al., 1979) and that they originate from the height of the extreme temperature minimum around the mesopause that occurs at high and middle latitudes in the summer months (Ecklund and Balsley, 1981). Later, the echoes were observed from various locations using radars with frequencies ranging from 50 MHz–1.3 GHz (Cho and Röttger, 1997). The PMSE is observed from mid-May to the end of August in the Northern Hemisphere, with the main occurrence during local noon (Latteck et al., 2021).

The observed reflection of the radio waves results from strong variations in the electron density and, thus, the refractive index. The echoes are strong as the backscattered radio waves interfere constructively when the distance between the scattering centers is half the radar wavelength, called the Bragg condition. Scattering at the Bragg condition

is typically caused by neutral turbulence in the atmosphere. PMSEs arise from a combination of neutral turbulence and the presence of charged ice particles that form near the cold mesopause and influence the electron distribution; the presence of these ice particles expands the Bragg scales for which the echoes are observed (Rapp and Lübken, 2004). The spatial distribution of the ice particles at these altitudes is influenced by the complex neutral atmosphere dynamics caused by the upward-propagating gravity waves. It can also be seen in the structure of noctilucent clouds (NLCs) (Dalin et al., 2004).

The region of PMSE occurrence overlaps with that of NLCs, which is an optical manifestation of these ice particles. Temperature studies of the summer Arctic mesosphere suggest that both phenomena are temperature controlled and occur at temperatures of 150 K and lower around the mesopause (Lübken, 1999), where water ice particles can form. Since 2007, water ice particles have also been observed by satellites in so-called polar mesospheric clouds (PMCs); the optical properties of water ice explain the measured cloud extinctions with inclusions of smaller meteoric smoke particles (Hervig et al., 2012). The meteoric smoke particles are nanometer-sized dust particles that form from ablated meteoric material in the altitude range 70–110 km (Rosinski and Snow, 1961; Hunten et al., 1980; Megner et al., 2006). The satellite observations also support the existing hypothesis that the ice particles are formed by heterogeneous condensation, which has recently been supported by a study that applies a new theoretical condensation model (Tanaka et al., 2022). The surface charging of dust particles, be it meteorite smoke, ice particles, or a mixture of both, is a necessary process that influences the growth of ice particles and, at the same time, gives clues to their size and composition (Rapp and Thomas, 2006). The dust can, for example, become negatively charged from electron attachment in the PMSE altitude range. This is indicated by rocket measurements of so-called electron "bite-outs" (depletion in electron density), where PMSE is present (Rapp and Lübken, 2004, and references therein).

Previous studies have shown that the modulation of PMSEs during artificial heating with high-frequency (HF) radio waves could be used to study the underlying plasma and dust particles (Biebricher et al., 2006; Mahmoudian et al., 2011, 2020). During such heating experiments, the electron temperature is locally and temporarily enhanced (Rietveld et al., 1993); Chilson et al. (2000) first noticed that PMSEs can be modulated during such heating. The PMSE often almost disappears when the heater is turned on and then returns when the heater is turned off again. It is assumed that the increased electron temperature during heating and the resulting increased diffusion reduces the fluctuations in the electron density and thus the PMSE power (Rapp and Lübken, 2000). Havnes (2004) found that with an adequate on/off time of the heater, a so-called overshoot characteristic curve could be generated, in which the PMSE power did

not return to the original value after heating but exceeded it. Such overshoot curves have been observed in many simultaneous radar and heating studies of PMSE made with EISCAT. The overshoot curves have also been observed for some polar mesospheric winter echoes (PMWEs) (Kavanagh et al., 2006; Belova et al., 2008; Havnes et al., 2011). Most PMWEs do not appear to be associated with the presence of dust (Latteck et al., 2021). Still, those showing overshoots are more likely related to the presence of small dust particles, possibly meteoric smoke.

With this work, we want to investigate whether and how the PMSE modulation during heating can be used for systematic investigations of the charged dust component. We present observational studies of PMSE with the EISCAT VHF radar during four VHF/heating campaigns, which are all done in August during twilight or night conditions. This is the first systematic investigation of PMSE modulation under reduced sunlight conditions and toward the end of the PMSE season.

The remaining part of the paper is structured as follows. First, Sect. 2 introduces the PMSE modulation during heating and the overshoot effect. Section 3 describes the experiments we performed, including the radar and heating parameters, and gives an overview of the observational results. Then a discussion of the PMSE modulation is given in Sect. 4, where we first discuss the cases of quiet ionospheric conditions and of an ionosphere that is moderately influenced by energetic particle precipitation; we then give an overview of the observed PMSE modulation. We make a comparison with a model calculation and discuss the overall outcome. A short conclusion is given in Sect. 5, and additional information on observational data is provided in Appendix A and the Supplement.

2   PMSE and heating

The EISCAT heating facility transmits high-frequency radio waves of high power into the atmosphere (Rietveld et al., 1993). Electron oscillations associated with wave absorption translate into thermal motion, heating the electron component while the other plasma components keep their initial temperature. As mentioned above, it was found that this active heating influences the PMSE signal. During the experiments, the heating is switched on and off in pre-defined time intervals (48 s on and 168 s off). The PMSEs are simultaneously observed with the EISCAT radar. The time variation of the observed PMSE power is sketched in Fig. 1 to illustrate the observed phases of the PMSE heating cycle and the often seen overshoot curve: decline, heating phase, recovery/overshoot, and relaxation.

The amplitudes (R_0, R_1, R_2, R_3, and R_4) marked in Fig. 1 will be considered in our analysis of the observations below, where R_4 is then the start (R_0) of the next subsequent cycle. We follow previous studies (e.g. Havnes et al., 2015) and
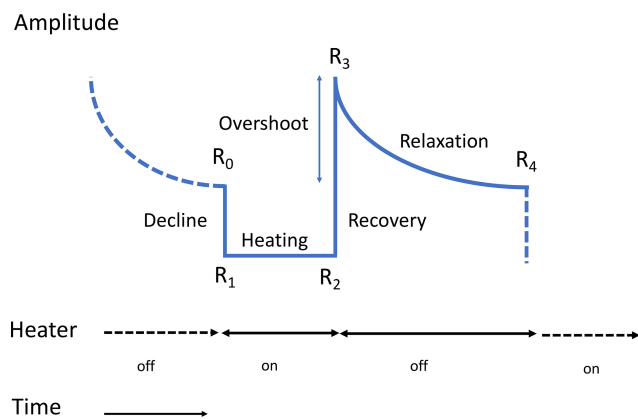
Figure 1. Sketch of the PMSE modulation due to HF heating in a typical overshoot curve; the power amplitudes during different times of the heating cycle are defined.

refer to the curves that describe the measured PMSE during one heating cycle (on and off time) as overshoot curves.

2.1 Decline

$R_0 \to R_1$: As the heater is switched on at R_0, the power effectively falls off instantaneously (depending on the radar frequency used) (Havnes, 2004). The backscattered power drops as the heating enhances the electron temperature and, consequently, the electron diffusivity so that the large electron density gradients are reduced. Therefore, the backscatter is less efficient (Rapp and Lübken, 2000).

2.2 Heating

$R_1 \to R_2$: During the heater-on phase from R_1 and R_2, there are some variations in the power amplitude. Because of the higher electron temperature, the charging electron flux on the dust particles increases during the heater-on period, and often an increase in the power can be seen. The charging timescales become shorter and compete more with the faster electron diffusion (Mahmoudian et al., 2011).

2.3 Recovery/overshoot

$R_2 \to R_3$: The power then increases when the heater is switched off (recovery), and in many cases, the power rises above the previous undisturbed level (overshoot). The electron temperature drops quickly to the initial value before the heater is on due to the highly collisional regime at these altitudes. The dust particles carry a higher charge than before and repel the electrons more strongly. The electrons follow the ion diffusivity, and as a result, the electron density gradients become larger. This causes the backscatter to be larger, creating an overshoot in power.

2.4 Relaxation

$R_3 \to R_4$: Now the power relaxes back to the previous undisturbed level, with a varying relaxation time depending on the conditions. With a long relaxation time, new and undisturbed plasma can enter the radar beam, or the dust present has time to discharge (Havnes, 2004).

3 Observations

We first describe the overall observation conditions, radar operations, and radar analysis, and then we present an overview of the data.

3.1 Overall observation conditions

The presented observations were carried out during the "Mesoclouds 2018" and "Mesoclouds 2020" campaigns in collaboration with UiT Tromsø and IRF Kiruna. The EISCAT VHF radar and the EISCAT heating facility are located in Ramfjord near Tromsø, Norway (69.59° N, 19.23° E). The observations were made on 11/12 and 15/16 August 2018 and 5/6 and 6/7 August 2020, during the night between 20:00 and 02:00 UT. These observations thus represent dusk and night conditions with reduced influence of sunlight on the observational volume compared to other observations, mainly done around noon in June and July.

The solar zenith angles during the observations are in the range of 88–97°. PMSEs at 80–90 km altitude are still sunlit but to a lesser extent for most of the previous PMSE observations. To estimate the difference, we compare the solar illumination at the time of our 15 August (2018) observations to those of the summer solstice in the same year. We derive the solar UV flux by calculating the absorption of the solar UV flux by O_2 along its path through the atmosphere (described by Giono et al., 2018). We use solar Lyman-α line (121.56 nm) flux from the SOLSTICE instrument on the SORCE satellite (https://lasp.colorado.edu/home/sorce/data/ssi-data/, last access: 27 February 2020) and O_2 densities from the NRLMSISE-00 atmosphere model (Hedin, 1991) for the location of the EISCAT VHF radar. We estimate that the solar photon flux in August at PMSE altitudes is reduced by at least 1 order of magnitude compared to noon conditions in June, as seen in Fig. 2. This translates to a reduced photoemission current by an order of magnitude. It thus influences the dust-charging conditions since the photoemission current is proportional to the photon flux (Mahmoudian et al., 2018).

Simultaneous optical measurements of NLCs were done using two cameras located at Kiruna and Nikkaluokta, Sweden (about 200 km south of Tromsø). There was, however, no NLC observation above the radar site, mainly because of weather conditions. During the night of 15/16 August, faint NLCs were observed from Kiruna close to the horizon, approximately above Andøya, i.e., more westward than the EISCAT site. Figure 3a and b shows the temperature profiles
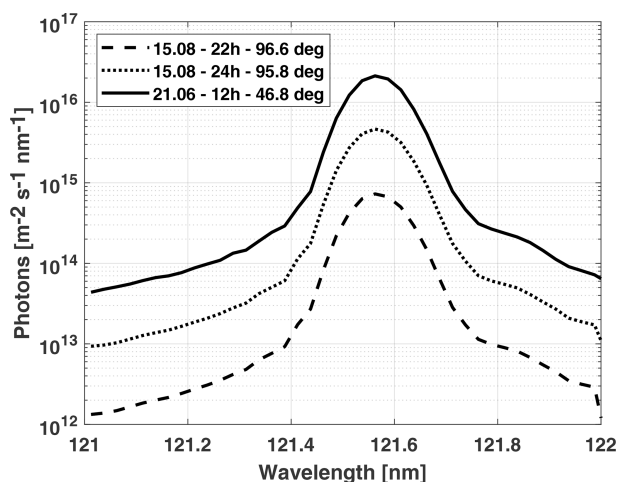
Figure 2. Estimated photon flux for the Lyman-α line for 21 June at 12:00 h (UT) and 15 August at 22:00 and 24:00 h (UT) at 85 km altitude. Solar zenith angles used in the estimation included in the label are from the International Reference Ionosphere (IRI) model (2016).

(blue line) as measured by the Aura satellite and frost-point temperature profiles (green line) estimated using the Aura water vapor data (both the temperature and water vapor were measured with the Microwave Limb Sounder (MLS) instrument). The height ranges in which the temperature is lower than the frost-point temperature indicate the regions where ice particles can form. This gives a good indication of the conditions present in the atmosphere, showing that the temperatures are cold enough to facilitate ice particle formation at PMSE altitudes. However, there could be variations due to the spatial and temporal differences between the measurements that must be kept in mind. These measurement points were the closest in time and space to the PMSE observations; the horizontal distance to Tromsø is about 490 km in Fig. 3a and about 293 km in Fig. 3b.

3.2 Radar operation and data analysis

The radar observations were made in the zenith direction with the EISCAT VHF (224 MHz) antennas near Tromsø (69.59° N, 19.23° E). The radar code used was Manda, and reference to EISCAT documentation (Tjulin, 2017) and radar and heating system parameters are given in Table 1. The EISCAT heating facility (Rietveld et al., 1993, 2016) was operated with a vertical beam at 5.423 MHz with a nominal 80 kW per transmitter, which corresponds to effective radiated power (ERP) in the range between 500 and 580 MW, and X-mode polarization was used with a sequence of 48 s on and 168 s off. The vertical extension of the heater beam extends far beyond the region covered by the radar. Given that the vertical winds and velocity fluctuations of the PMSE observed with EISCAT VHF are within a few meters per second and horizontal winds possibly a few tens of meters per

second (Strelnikova and Rapp, 2011), the radar at all times measures PMSEs that are influenced by the heating.

A standard incoherent scatter analysis, GUISDAP (Lehtinen and Huuskonen, 1996), was used to derive the radar data products. It provides the electron density derived from the incoherent scatter spectrum assuming that the electron and ion temperatures are equal (which they are not when the heater is on). The backscatter cross section is proportional to $1/(1 + T_e/T_i + \alpha^2)$ as is shown by Pinedo et al. (2014), indicating that when the heater is turned on, T_e increases and consequently the backscattered power decreases. The actual electron density is assumed to be not affected, so we use the unit of equivalent electron density as was done previously for observations of polar mesospheric winter echoes (PMWEs) (Kavanagh et al., 2006; Belova et al., 2008) and PMSEs (Mann et al., 2016). The post-experiment integration time used throughout this analysis was 24 s for computational reasons except for one of the observations when we compare with simulations. A resolution of 4.8 s was used. We found that choosing a higher time resolution for the overall discussion did not result in additional information.

3.3 Overview of observations

The observations were made from 20:00 to 02:00 UT on four nights in August 2018 and 2020. The observations are displayed in Fig. 4 and shown for the entire period with altitudes from 80–110 km, hence including PMSE and the conditions of the surrounding ionosphere. White vertical areas are observation gaps due to operational problems. We identified interesting measurement intervals in each data set we considered for analysis. A closer look at each area is given in the Supplement, and an overview of the time and altitude range of the areas is shown in Table A1 in the Appendix A.

3.4 Observation 1: the 11/12 August 2018

PMSE was observed until around 01:30 UT. One can see that the electron densities above and partly below the PMSE are high, showing the typical appearance of particle precipitation. In area 1, the precipitation is strong, and enhanced electron density was observed as low as 80 km, well below the PMSE layer. We considered the following.

- Area 1: PMSE with strong precipitation in the altitude range 83.4–85.6 km from 21:36 UT, lasting about 20 heater cycles;

- Area 2: high-altitude and long-lived PMSE layer extending from 86.3–90 km during about 40 heater cycles, starting from 23:06 UT with some precipitation;

- Area 3: low-altitude PMSE at 83.4–86.4 km from 00:00 UT lasting about 30 heater cycles with some precipitation at the end of the layer.
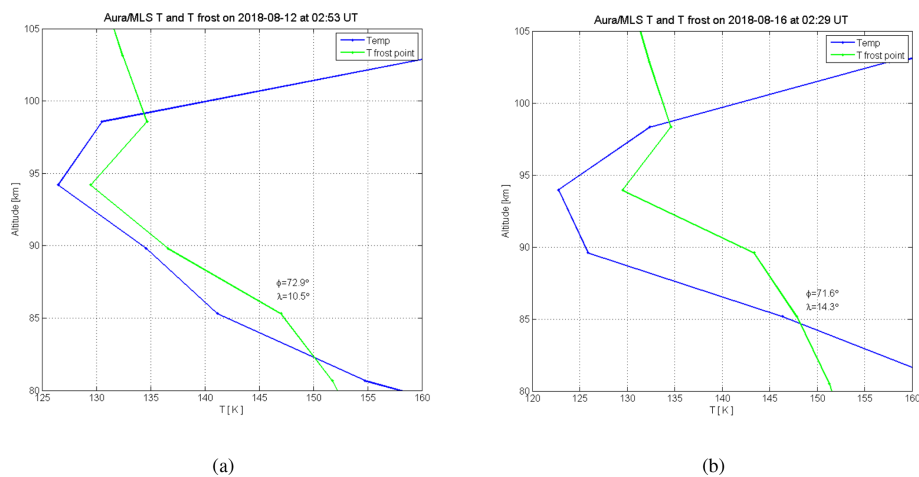
(a)   (b)

Figure 3. Temperature profiles (blue line) as measured by the Aura satellite at 12 and 16 August 2018 and frost-point temperature profiles (green line) estimated using the Aura water vapor data. Latitude and longitude of the measurement points are given in the figures by ϕ and λ respectively.

Table 1. Parameters for EISCAT VHF radar operation and EISCAT heating facility. Half of the VHF antenna is used for transmitting, and the entire antenna is used for receiving (beamwidth adjusted accordingly).

EISCAT VHF			
Frequency	224.4 MHz	Resolution in range	360 m
Wavelength	1.34 m	System temperature	240–370 K
Transmitter peak power	1.5 MW	Antenna gain	43 dBi
Radar code	Manda	Half-power beamwidth	$1(2) \times 2.4 \times 1.7°$
EISCAT heating facility			
Frequency	5.423 MHz	On time	48 s
Beamwidth	7°	Off time	169 s

3.5 Observation 2: the 15/16 August 2018

PMSE was observed before midnight and then again at 02:00 UT. at the end of the measurements. The first observed PMSE (area 1) seems to be not influenced by precipitation. The PMSE observed later (areas 2 and 3) are influenced by moderate precipitation. Modulation is seen in the backscattered power of the lightly ionized portion of the ionosphere from 90–110 km, which can be seen around 20:00–21:00 UT. We considered the following.

- Area 1: high-altitude weak PMSE observed around 20:30 UT at 88–90 km;

- Area 2: PMSE observed from 20:50 to 21:50 UT at 86–88 km, in parts influenced by precipitation;

- Area 3: PMSE from 22:00 UT influenced by moderate precipitation extending over altitudes 83.4–87.8 km during about 30 heater cycles.

3.6 Observation 3: the 5/6 August 2020

PMSE was observed only before midnight. Some observations (areas 1 and 2) show no apparent influence of precipitation. Before the start of area 1, there is PMSE present. However, this is not included in the analysis due to (most likely) direct interference from the heater caused by arcing, which can be seen as vertical lines extending through all altitudes. For completeness, we also consider area 3, which displays a layered structure and is influenced by the heating. The height and the shape suggest, however, that this is not PMSE but rather a sporadic E layer. We considered the following.

- Area 1: strong PMSE in the absence of apparent precipitation for about 1 h from 21:30 UT at 82–88 km;

- Area 2: PMSE at 83–87 km in the absence of apparent precipitation between 22:50 and 23:50 UT;

- Area 3: structure observed above 90 km from 22:45 UT consistent with a sporadic E layer; not included in analysis.
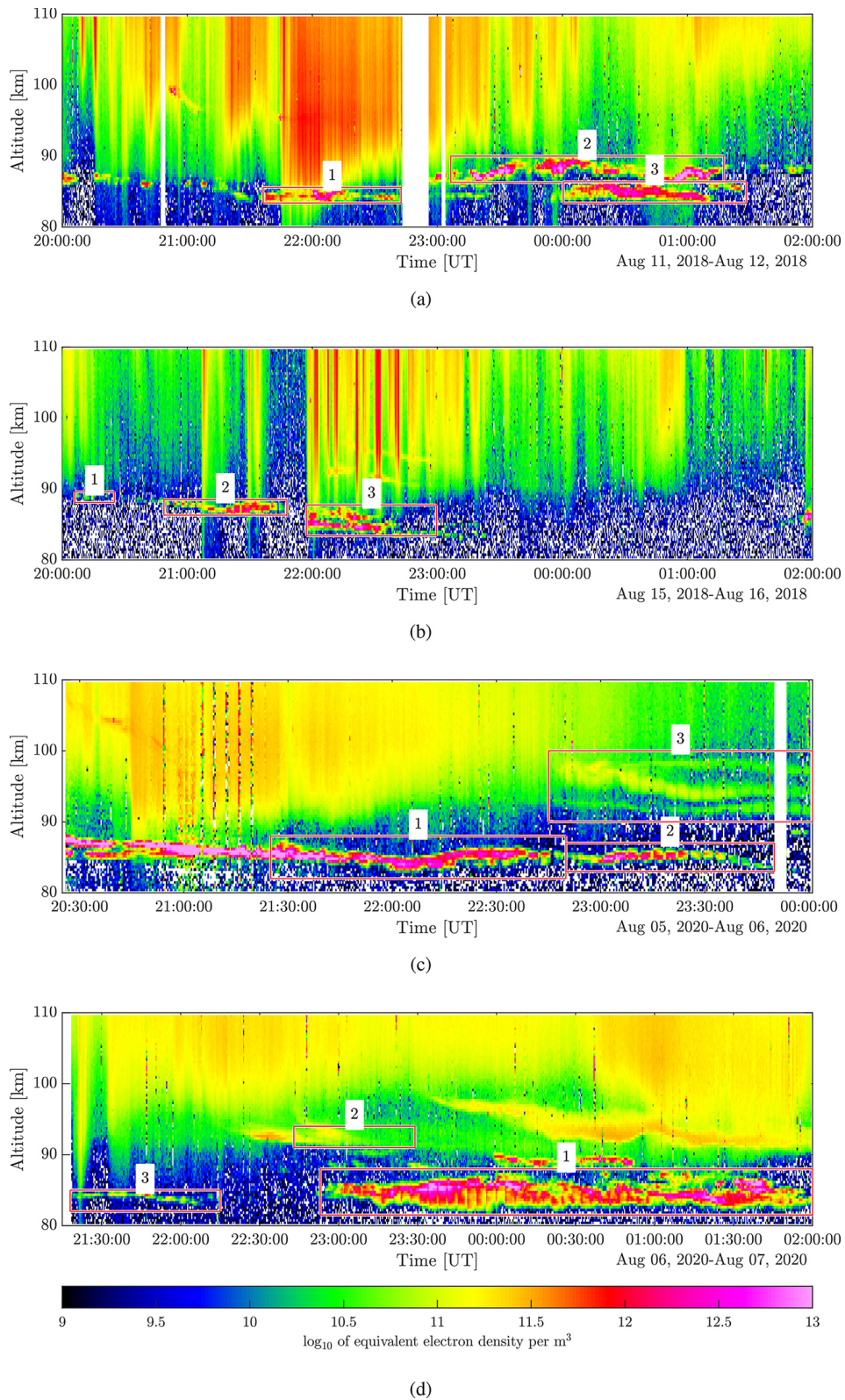
Figure 4. Overview of all four observation days with time intervals and dates given in each respective figure.
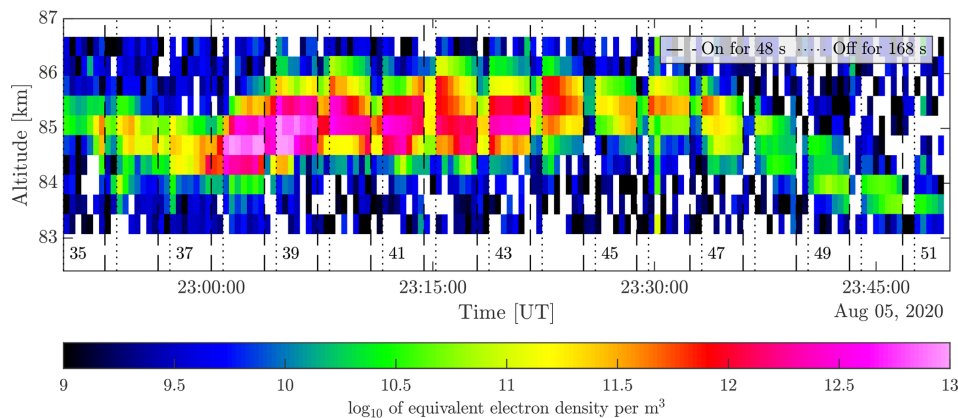
Figure 5. Backscattered power as a function of altitude and heating intervals observed during the night of 5/6 August 2020, in area 2.

3.7 Observation 4: the 6/7 August 2020

From the fourth observation, we see a low-altitude PMSE layer only slightly influenced by precipitation, a second layer at high altitude influenced by heating that also might be a sporadic E layer, and a third area extending over a long period in time and many altitudes that do not seem to be influenced by particle precipitation. We considered the following.

- Area 1: a long interval of PMSE between 81–88 km partly in the quiet ionosphere and partly influenced by precipitation;

- Area 2: sporadic E layer above PMSE height; not included in analysis;

- Area 3: a weak PMSE with little apparent precipitation for about 1 h from 21:30 UT at 82–88 km.

We find, in general, that the overshoot effect disappears in the presence of strong or moderate precipitation, as seen in the 15/16 August 2018 observation in Fig. 4. This is better illustrated in the figures given in the Supplement, where each area is enhanced. At the beginning of the observation campaign on 15/16 August 2018 (area 1), a weak PMSE developed under very quiet ionospheric conditions. The echoes are only weakly enhanced in comparison to surrounding areas, the backscattered power is reduced during heating, and an overshoot is also observed (see Fig. S4).

4 Observed PMSE modulation

First, we discuss two selected cases, one with little or no particle precipitation and one with moderate precipitation. Then we summarize the heating effect and overshoots visible in all the observations, and we discuss these findings in the context of previous observations. Finally, we compare a selected case with simulations of the overshoot cycle and discuss what information we can gain from modulating PMSE with heating.

4.1 PMSE modulation under quiet ionospheric conditions

To discuss PMSE modulation under quiet ionospheric conditions, we chose an area with no apparent energetic particle precipitation; we consider area 2 from the 5/6 August 2020 observation (Fig. 4c). The overshoot curves can be assessed using the overall power plot shown in Fig. 5. The beginnings of new heating cycles are marked with dashed lines when the heater is turned on. The dotted line indicates the time when the heater is turned off again. In many cases, the PMSE signal changes at the heater on and off times and during the cycles themselves. The PMSE layer lies within the altitude range of 83–87 km with a maximum extension of 2 km at its widest. There are clear indications of reduced PMSE power when the heater is on; in many cases, we can see clear overshoots.

In Fig. 6, we have selected two altitude sections for a closer look, altitude 85.2 and 85.6 km, where we can see overshoots in many of the cycles. In general, the overshoots are relatively large, with some an order of magnitude larger than the pre-heater value and with some showing no apparent increase in the PMSE power after the heater is turned off. This seems especially true for the top altitude where the PMSE power is at its highest, the lower height has a somewhat lesser PMSE power, and more overshoots are visible. The decline is visible in many of the cycles and is very strong for cycles 40–47. One can also see that characteristics of decline and overshoot often change between adjacent heating cycles and height intervals, e.g., in heating cycle 41.

For a closer investigation, we describe the ratios of the amplitudes during the different phases of the heating cycle. The different power amplitudes are marked in the overall sketch given in Fig. 1. The different amplitudes observed during the heating cycles are plotted in Fig. 7, where the amplitude ratios are considered. We find that during most heating cycles, the signal drops when the heating is switched on (decline $R_1 < R_0$, Fig. 7a).
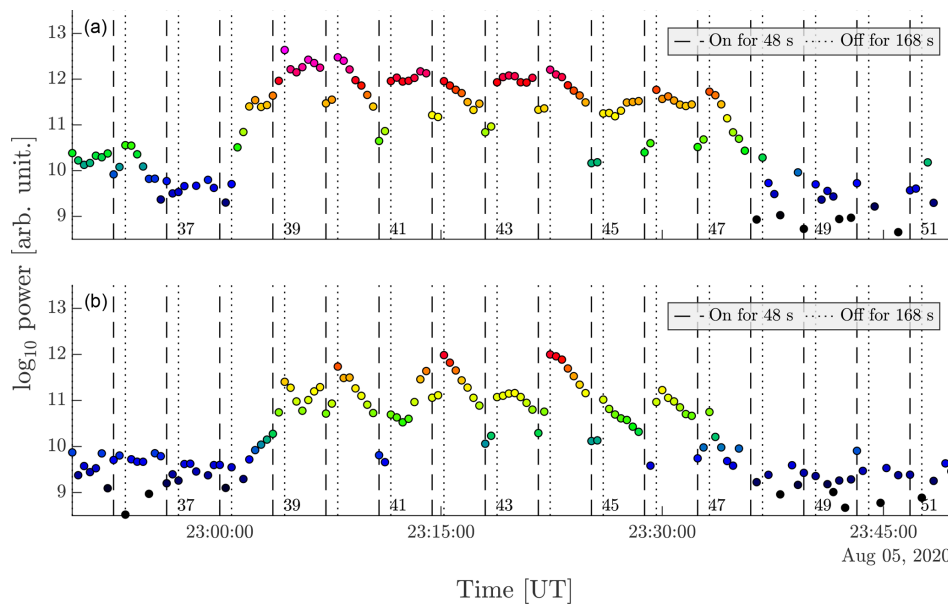
Figure 6. Backscattered power at altitude 85.2 km **(b)** and 85.6 km **(a)** and heating intervals observed during the night of 5/6 August 2020 in area 2. The color of the dots follows the color scale of Fig. 5.

We assume that the observed signals are PMSE when $R_0 > 10^{10.5}$ (which corresponds to around 3.16×10^{10}; Ullah et al., 2019), and one can see that in most cases that do not meet this requirement; there is no PMSE modulation visible. However, as we will see later, this condition removes a few instances of low-power modulated PMSE with large overshoots. The same can be said for the green points that show a decline but are below the threshold. They could be showing a decline but also be noise due to random fluctuations from the two measurement points.

The ratio of the amplitudes R_0 and R_3 describes an overshoot ($R_0 < R_3$), and this comparison shows that overshoots and undershoots are equally abundant, independent of the signal strength (Fig. 7b). Comparing the signals at the beginning of subsequent cycles (Fig. 7c) shows no trend and a broad range of values which suggests variation either due to ionospheric conditions or due to neutral turbulence (rather than dust).

One can see in Fig. 7d that for strong signals the amplitude stays constant or decreases slightly during the heater-on phase. The change in amplitude during the heating can indicate the charging process of the dust particles, where the faster timescale of diffusion or dust charging dominates (Mahmoudian et al., 2011). According to Havnes et al. (2015), large PMSE structures can cause the diffusion timescale to be longer and, consequently, have a quicker and larger increase in power during the heater-on phase. The comparison of R_2 and R_3 in Fig. 7e describes to what extent the signal increases again when the heater is switched off. This increase is seen in most cases except for the small am-

plitudes, which might be either low-power PMSE or random fluctuations.

Finally, in Fig. 7f, the ratio of R_3 and R_4 describes the signal after the heater is switched off (relaxation). One can see a broad scatter symmetrically around the diagonal, indicating that the natural variations in the PMSE power are dominant. Any relaxation after heating is difficult to discern from this since their contribution could disappear due to a significant background increase in PMSE power. This is due to the considerable period between the two points (168 s), which according to Havnes (2004), is enough time for the ionosphere to change or dust to become discharged, whereas 48 s used for the on time is not.

We compile these results in histograms of the amplitude ratios (Fig. 8). The histograms contain only cycles with a value $R_0 > 10^{10.5}$ of the PMSE amplitude before the heater is turned off to only include those with PMSE and exclude the cycles that contain noise or are mostly noise. We only include those cycles that show a decline due to heating in all the histograms. In Fig. 8a, we see that 55 % of the ratios are smaller than 1 and thus show a decline (affected by the heater) and that the average value of those ratios that are below 1 is 0.72. This is a reduction of 28 % of the pre-heater value on average when the heater is turned on. We have the overshoot in Fig. 8b. Only 10 % of the cycles show an overshoot with an average value of 0.44. Even though there are not many overshoots for this observation, those observed show an average reduction of more than half, indicating very large overshoots. Figure 8c shows that most (95 %) of the observations show a decrease in power while the heater is on. Figure 8d shows that 66 % of the cycles show an increase in power when the
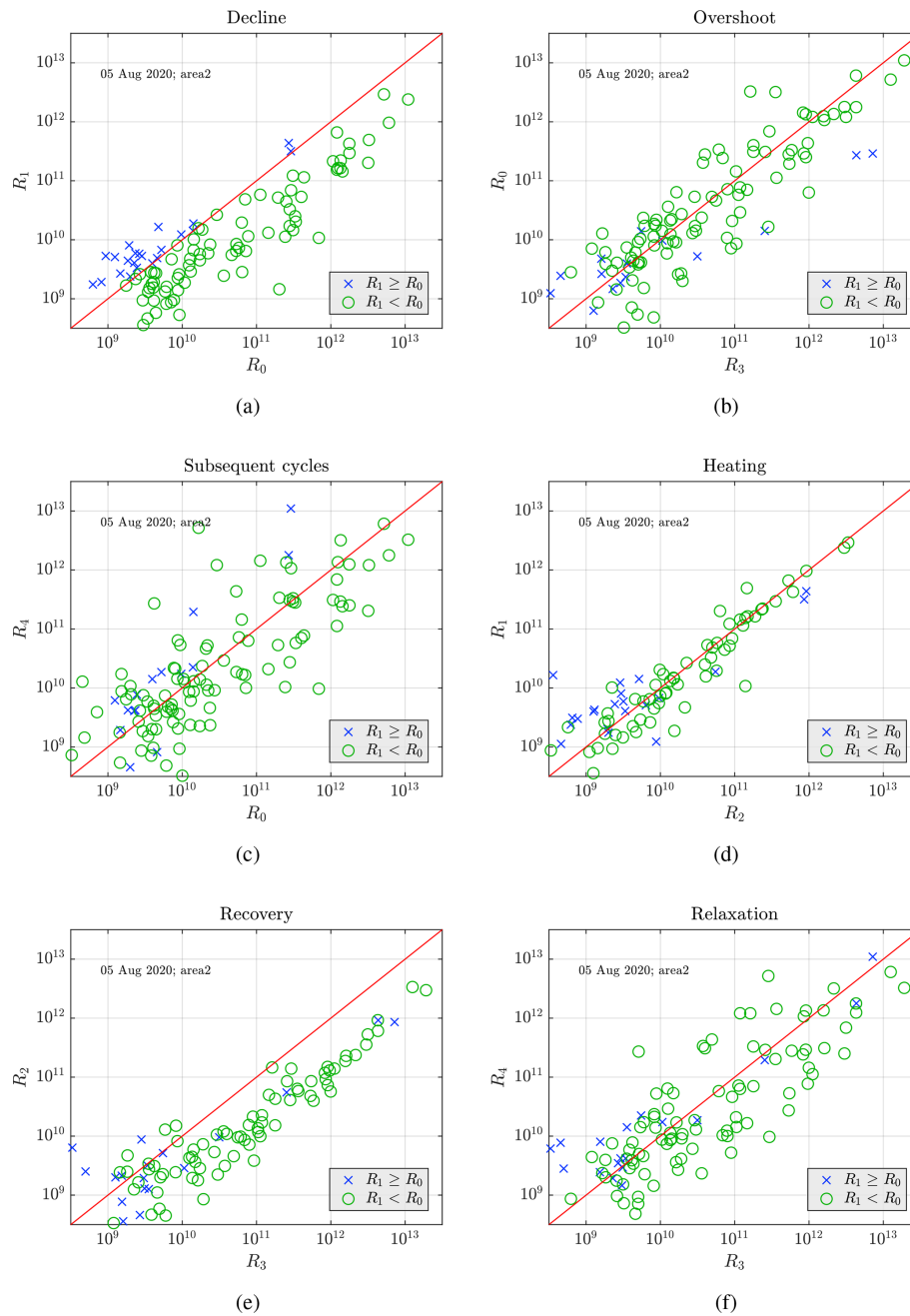
Figure 7. Comparison of the power amplitudes observed on 5/6 August 2020, area 2.

heater turns off, which is similar to the number of cycles that show a power reduction when the heater is turned on. Then in Fig. 8e, we see a general increase in power from cycle to cycle. Thus a general decrease to pre-heater value cannot be determined, most likely due to increasing background PMSE dominating the signal and the histogram, where 87 % of the cycles show an increase in power in subsequent cycles. This can be related to why we see so few overshoots in this observation, and that increase in PMSE power is significant for

many of the cycles. The overshoot disappears due to background variations.

4.2 PMSE modulation during moderate particle precipitation

Conditions with moderate particle precipitation are observed in area 2 of the observation from 15/16 August 2018 (see Fig. 4b). The overall power plot is shown in Fig. 9. As discussed above, some heating intervals have noticeably very
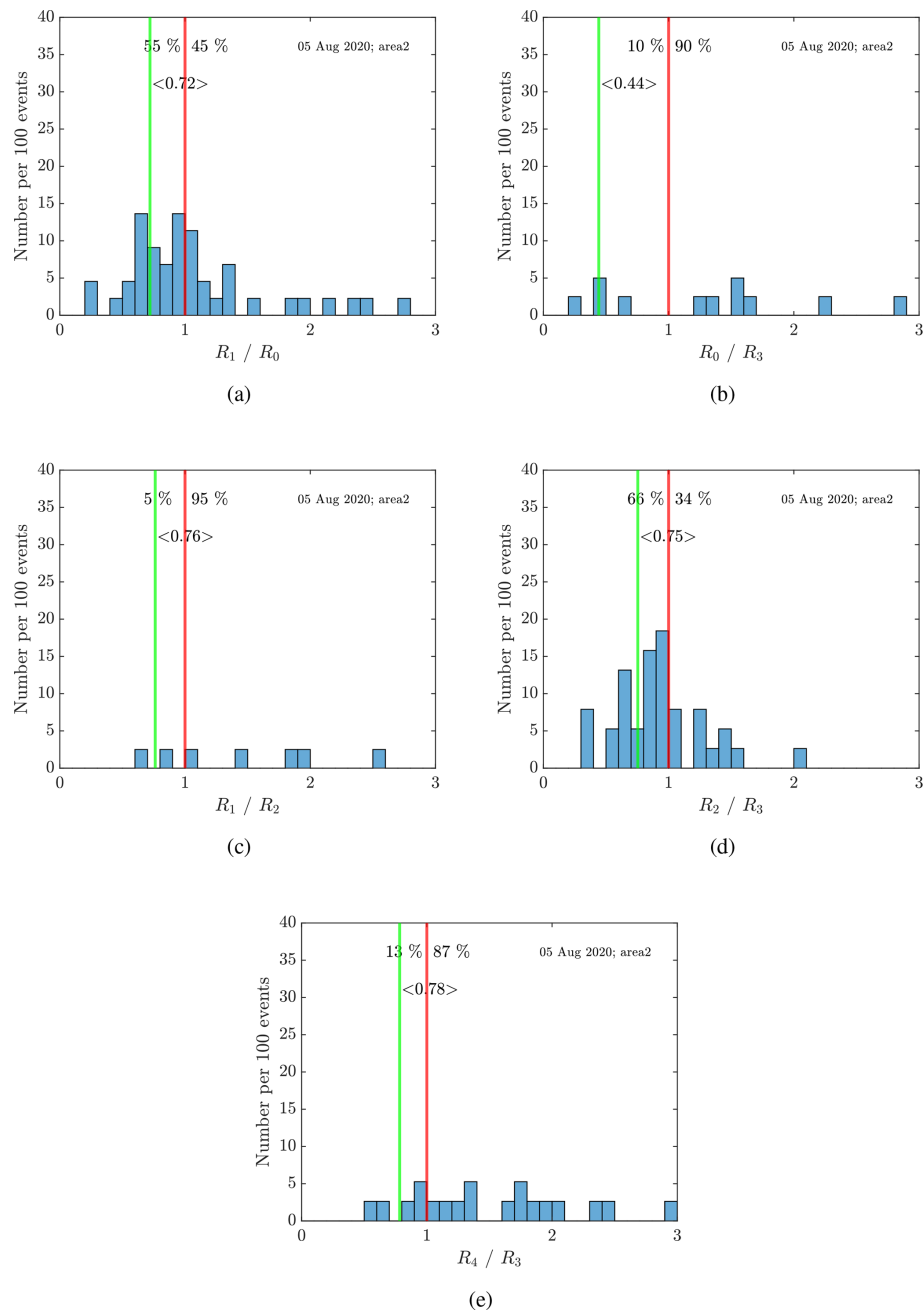
Figure 8. Average of (**a**) decline, (**b**) overshoot, (**c**) heating, (**d**) recovery, and (**e**) relaxation for the observed data on 5 August 2020 in area 2. Only overshoot curves with a minimal background amplitude of $R_0 > 10^{10.5}$ are considered. The ratios are chosen so that if we observe an overshoot curve like shown in Fig. 1, all ratios are smaller than 1. Thus, the histograms are clipped at a maximum ratio of 3. The green line and the corresponding number display the mean for all ratios smaller than 1.

strong overshoots (14, 15, 16, 17). One can note that the influence of the heating is most pronounced at the beginning and the very end of the observation interval when there is no apparent particle precipitation. Precipitation occurs in cycles 18 and 19 and then in cycles 24 and 25. When the heater is switched on, there is no reduction in power, and the precipitation dominates the received signal for all altitudes in

these cycles. The power plot for two selected height intervals shown in Fig. 10 shows this in more detail, where the modulation entirely disappears in the cycles influenced by precipitation. This is to be expected and has been shown before. One of the reasons why the modulation disappears in the PMSE layer is that the atmosphere below the layer is ionized due to the strong precipitation, and the HF radio wave might be

strongly absorbed before it reaches the PMSE layer and thus not be strong enough to heat the electrons appreciably in the layer.

The different amplitudes observed during the heating cycles in this area are plotted in Fig. 11. We find that during most heating cycles, the signal drops when the heating is switched on (decline, Fig. 11a). The cases that show no decline are spread over all amplitudes, indicating the cycles that might be influenced by precipitation and thus might show an increase in power when the heater is on. The overshoots and undershoots are equally abundant independent of the signal strength (Fig. 11b). As observed in the area discussed above, there is no trend when comparing the signals at the beginning of subsequent cycles (Fig. 11c). The change of amplitude during the heating (Fig. 11d) is small for most observations.

In most cases, the amplitude increases (Fig. 11e) when the heater is switched off, similar to the heated cycles, which is to be expected. Finally, in Fig. 11f, the ratio of R_3 and R_4 describes the relaxation, showing a large spread around the diagonal with somewhat more observations showing a reduction. This large spread can be attributed to the ionospheric variability due to the large timescale of the off time, as was mentioned previously.

The histograms of the power amplitudes are shown in Fig. 12 with the same criterion as before (also given in the figure text). Here the overshoot is seen in 55 % of the cycles with an average of 0.75 decline ratio (Fig. 12a), similar to the previous observation. Here the overshoot is seen in 31 % of the observations with an average of 0.64 overshoot ratio (Fig. 12b), which is more than the previous observation, even with precipitation. Similar to the previous observation, when the PMSE power increases (and is not influenced by precipitation), we see an influence of the heater but not an overshoot (or a minimal overshoot). For the cycles with a lower PMSE power (like in cycle 15), the overshoot is large, but the background PMSE power is lower; thus, the overshoot is easy to see. During the heating, there seems to be a general decrease in the values, with 76 % of the values showing a decrease during the heater-on phase (Fig. 12c). The recovery (Fig. 12d) ratio shows that 58 % has an increase in power when the heater is turned off, showing similar values to those for when the heater is turned on (decline). Then there seems to be a little over half of the cycles that show a general increase in pre-heater values between cycles (Fig. 12e).

4.3 Overall observational discussion

Here we summarize, in Table 2, the decline and overshoot ratios for all the observations (see Figs. S27–S36 in the Supplement for reference). In general, the heating effect is seen in more than half of the heating cycles for each respective area, with most of the average ratios showing values close to 0.75. These calculations show only the observations with a

value of $R_0 > 10^{10.5}$ to indicate the presence of PMSE and exclude noisy data.

This, however, causes the faintest PMSE to be excluded from the histograms, as is seen for the overshoot ratio for area 1 from 15 August 2018; here, the PMSE power is below the threshold. Thus no cycles are included in the calculation despite 100 % of the cycles showing a decline due to heating. This would suggest manually inspecting low-power PMSE influenced by heating would be a better option or introducing other criteria to include these.

To summarize, we see only overshoots in less than half of the cycles, with many cycles often more influenced by background ionospheric conditions that might overshadow the heating of the PMSE. Ullah et al. (2019) show a more significant occurrence of overshoots in their observations, with around 40 %–70 %, where their observations were during daytime. Havnes et al. (2015) observations had a much larger ratio of cycles with decline present and a slightly higher percentage of overshoots present.

However, in our case, we see a few instances where the overshoot in some cycles is unusually large. Myrvang et al. (2021) found that a higher electron temperature due to heating could be achieved during nighttime compared to daytime, which might help explain some of these large overshoots. However, Kassa et al. (2005) found for their observations that the heating temperature effect observed increased for the observation with the most amount of sunlight (near noon).

Other possible reasons for unusually large overshoots could be a change in the PMSE/NLC season, as is noted by Latteck et al. (2021), when the season is getting longer. Since our observations are in reduced sunlight and close to the end of the season, more varying background conditions might influence our observations than those during the day in June/July.

4.4 Comparison of a selected observation to simulation

Here we take a closer look at the approximately 1 h time interval, which is marked as area 2 in the observation from 15–16 of August 2018, shown in Fig. 13; the data cover the heating cycles 12 to 27 and range over seven height intervals of around 360 m each. The ionosphere is influenced by precipitation in cycles 18 and 19 and then again in cycles 24 and 25, and there are no overshoots present in those heating cycles, as mentioned before. The PMSE in intervals marked with A, B, and C in the figure shows a decrease when the heater is on and overshoots when the heater is turned off. Interval A shows relatively low PMSE power but quite high overshoot curves compared to intervals B and C, as we will investigate further.

Individual heating cycles are shown in Fig. 14a for both altitudes from interval A, with PMSE power and measurement error provided by the EISCAT GUISDAP analysis. The corresponding average overshoot cycle for the respective altitude is shown on the right in Fig. 14b; in blue is the corre-
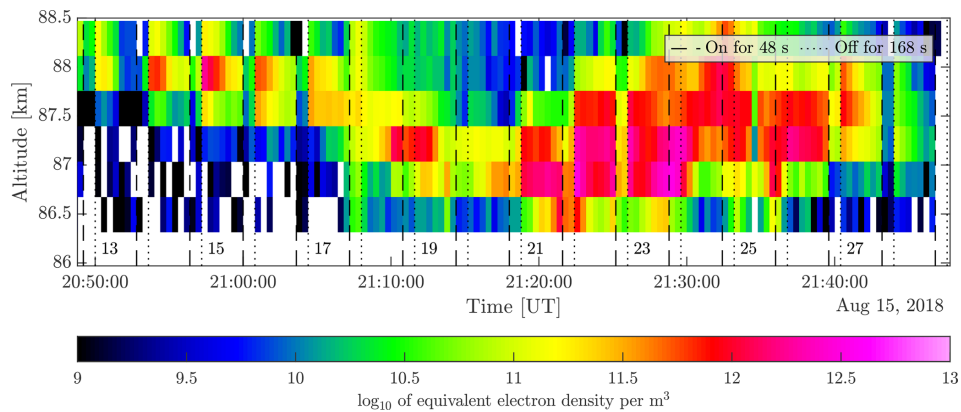
Figure 9. Backscattered power as a function of altitude and heating intervals observed during the night of 15/16 August 2018, in area 2.
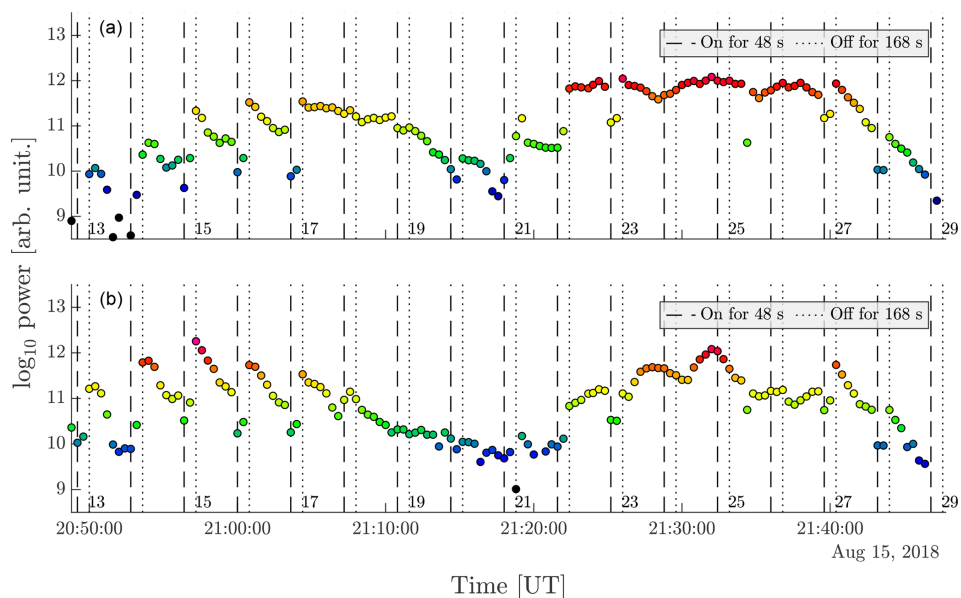

Figure 10. Backscattered power at altitude 87.4 km **(b)** and 87.8 km **(a)** and heating intervals observed during the night of 15/16 August 2018 in area 2. The color of the dots follows the color scale of Fig. 9.

sponding average overshoot cycle for the respective altitude. As can be seen, the overshoot is relatively strong for many of the heating cycles, especially the strong overshoot seen in cycle 15 for both altitudes with relatively high but decreasing overshoot on both sides of the cycle. Note the two y-axis scales for the different altitudes, where the heating cycles from altitude 88 km have such a low background PMSE power that the scale is an order of magnitude lower than the altitude below. Both altitudes have relatively low background PMSE power compared to intervals B and C, with the PMSE at 88 km altitude barely present or the irregularities on the limit of being seen by the VHF radar. It is thus interesting to find such large overshoot cycles for this particular interval.

Individual heating cycles from intervals B and C are shown in Fig. 15a with their corresponding altitude average on the right-hand side in blue (Fig.15b; note that here the y-axis

scale is the same for all the altitude ranges). They cover heating cycles 21, 22, and 23. The overshoots are present for the lower altitudes but are not as high as in interval A. However, the overshoot does not decline evenly but increases again before reaching the initial signal level. This influence can be seen in the averaged heating curve for altitude 86.7 km, where after about 120 s, the power starts to increase again. This is either because of the beginning influence of particle precipitation on the ionosphere or variation of the PMSE structure due to the long relaxation time (Havnes et al., 2015). This influence is very strong in the subsequent cycle (cycle 24), where the PMSE power increases during the heater-on period. This type of ionospheric variation can influence the observations to the extent that heating effects are less visible. In the same time interval (intervals 21, 22, 23) at the altitude above, the overshoots are small, es-
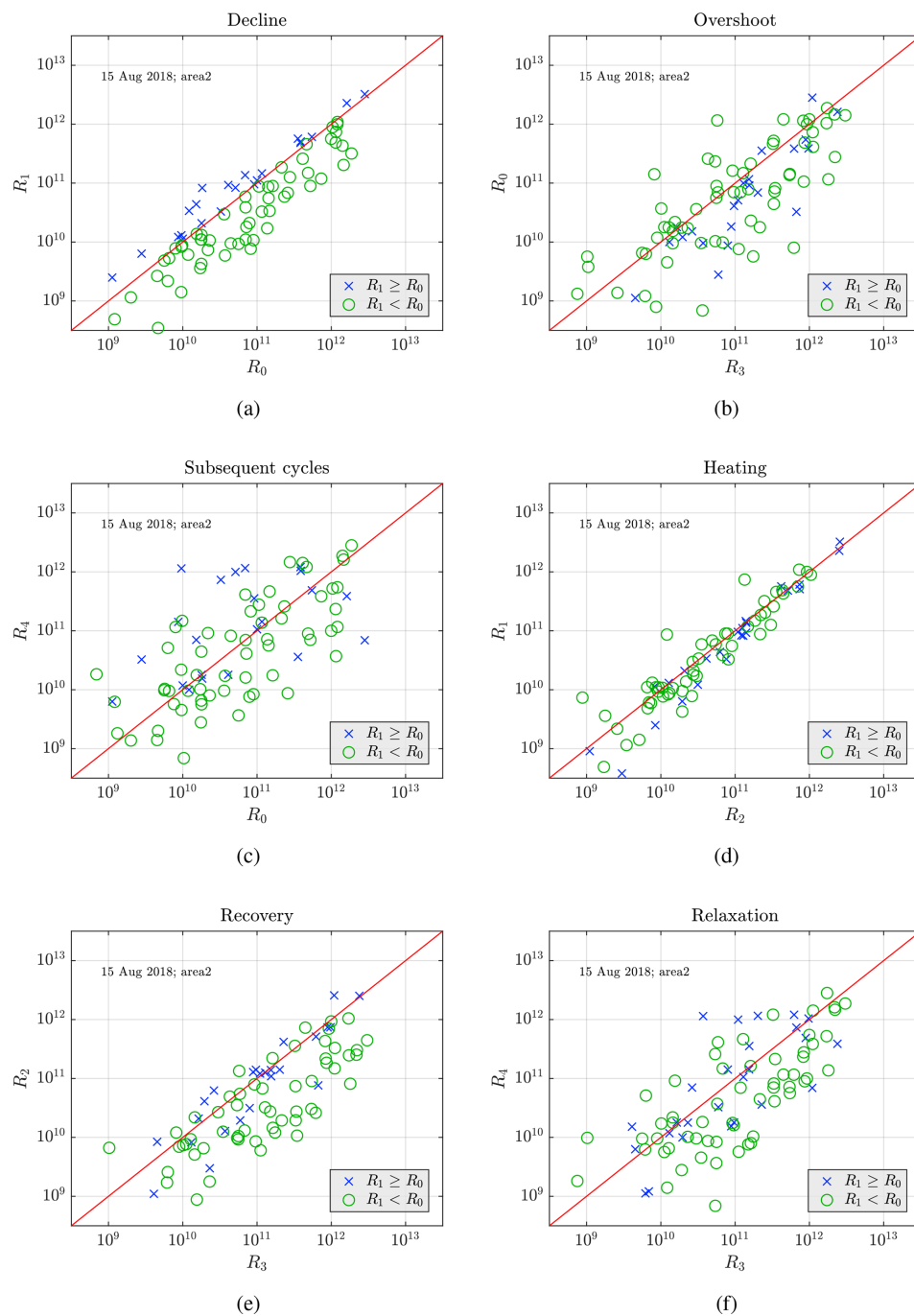
Figure 11. Comparison of the power amplitudes observed on the 15 August 2018 in area 2.

pecially for the first cycle (21), while the PMSE power is relatively low. This is in contrast to the observation made at the higher altitude in interval A where a significant overshoot is observed at low PMSE power. This might indicate that there are different conditions at play for these two cases. Havnes et al. (2015) has mentioned that higher altitudes of PMSE reside in more turbulent conditions, thus a more significant

variation in cloud structure and a longer relaxation time after heater turn-off time as a result.

A comparison of the average overshoot curves for each interval (A, B, and C) is shown in Fig. 16a and their corresponding normalized average curves in panel (b). The values are normalized to the initial PMSE power taken as the average of the last five values (24 s) before the heater is turned on. This is chosen to have sufficient data when some mea-

(a)

(b)

(c)

(d)

(e)
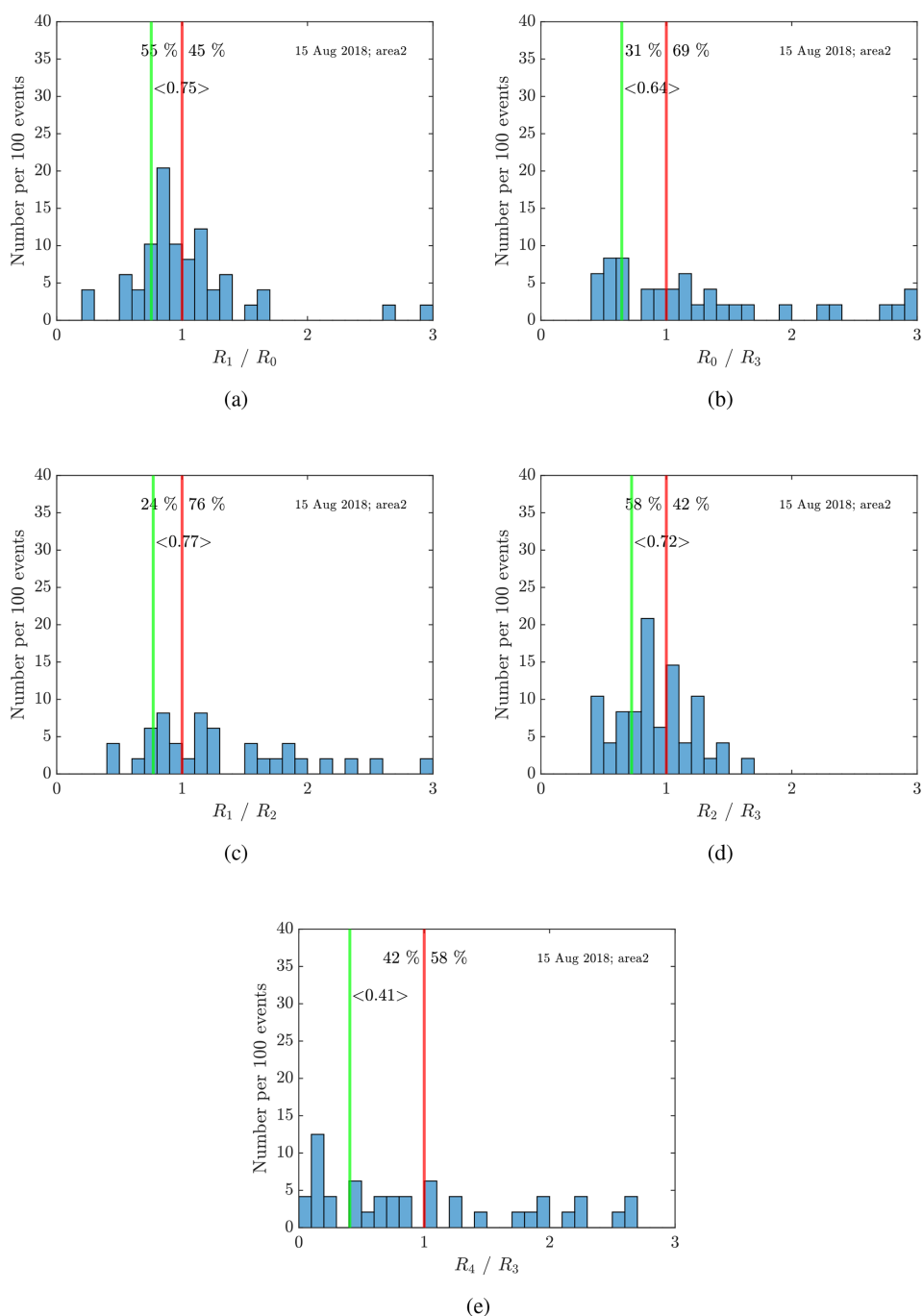
Figure 12. Average of **(a)** decline, **(b)** overshoot, **(c)** heating, **(d)** recovery, **(e)** relaxation for the observed data on 15 August 2018 in area 2. Only overshoot curves with a minimal background amplitude of $R_0 > 10^{10.5}$ are considered. The ratios are chosen so that if we observe an overshoot curve like shown in Fig. 1, all ratios are smaller than 1. Thus, the histograms are clipped at a maximum ratio of 3. The green line and the corresponding number display the mean for all ratios smaller than 1.

surement points are missing and to better compare to the rest of the data used in this article which are at a resolution of 24 s. Data were normalized after averaging the cycles from each interval. We can see that the highest normalized overshoot (b) is the one from interval A, which has the lowest background PMSE power (a) and that the lowest normalized

overshoot is from interval C, which has the corresponding highest PMSE background power. This high PMSE power is possibly due to an onset of precipitation which becomes apparent in the subsequent cycle 24 right after intervals B and C.

Table 2. Summary of histogram results (see histograms (Figs. S27–S36) in the Supplement) for the decline (R_1 / R_0) and the overshoot (R_0 / R_3) ratio when they are smaller than 1 (indicating heating effect and overshoot) for all four observations. These numbers only include observations with minimum background amplitude $R_0 > 10^{10.5}$. A1 refers to area 1 for that observation's date and so forth.

		Decline $R_1 / R_0 < 1$		Overshoot $R_0 / R_3 < 1$	
		Average of ratio	% of ratio	Average of ratio	% of ratio
11/12 August 2018	A1	0.76	58 %	0.56	45 %
	A2	0.75	61 %	0.57	51 %
	A3	0.77	55 %	0.61	50 %
15/16 August 2018	A1	0.74	100 %	–	–
	A2	0.75	55 %	0.64	31 %
	A3	0.69	63 %	0.41	40 %
5/6 August 2018	A1	0.72	46 %	0.48	44 %
	A2	0.72	55 %	0.44	10 %
	A3	0.75	66 %	0.87	17 %
6/7 August 2018	A1	0.74	59 %	0.54	53 %
	A2	0.90	61 %	0.89	10 %
	A3	0.52	83 %	0.24	17 %
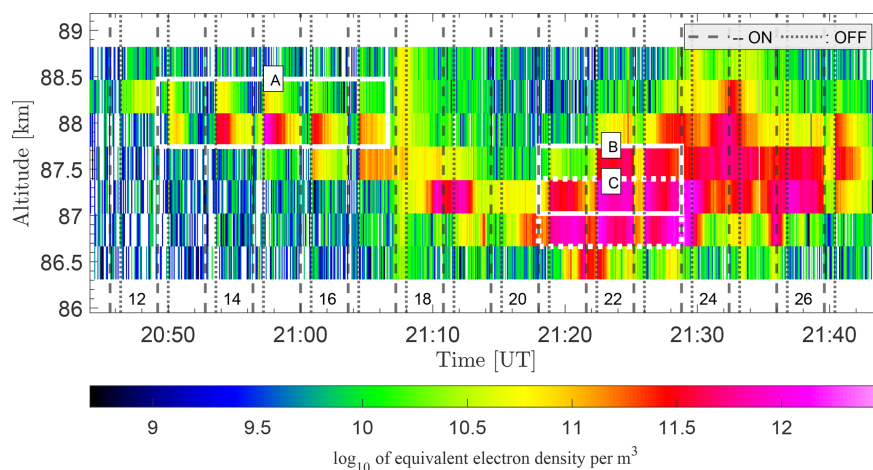
Figure 13. Overview of Area 2 – 15 of August 2018, with interesting visible overshoot cycles marked with intervals A, B, and C. Data resolution is 4.8 s. Cycles are marked in the figure (from 12 to 27) as well as their corresponding On/OFF period.

We compare these selected overshoot curves to a computational model initially developed at Virginia Tech. It treats the plasma as a fluid including an arbitrary number of charged particles, neutral particles, and dust particles; the dust charging is described in the orbital-motion-limited (OML) approach (see, e.g., Scales and Mahmoudian, 2016). The model's parameters include the electron diffusion time scale, the charging time scale, and the time evolution of electron and ion densities. The dust charging causes electron density depletion, and the amplitude of electron density fluctuations determines the radar backscattered amplitude. The simulations assume an initial plasma temperature of $T_i = 150\,\mathrm{K}$ and a background electron density of $2 \times 10^9\,\mathrm{m}^{-3}$. Which fits well with the same parameters derived from the IRI model (2016) for the time and date of the observation. The simula-

tion also assumes a reduced photoemission rate used in the charging equations in line with the experiments being done for conditions with low photoemission.

The resulting simulated overshoot curves are shown in Fig. 17b and for comparison are the averaged and normalized observations from intervals A, B, and C (marked in the same color and symbol as previous figures) shown on the left. The simulations best fit to the observed overshoot curves for 3 nm dust particles. However, there is little difference for similar sizes of dust (e.g., 3–4 nm). This result fits well with the altitude range we measure the observed PMSEs since, in general, we can assume to find smaller particles of dust at higher altitudes (however subject to neutral air movement) as well as the fact that there were no NLCs observed and thus the particles were not optically visible (larger > 20 nm).
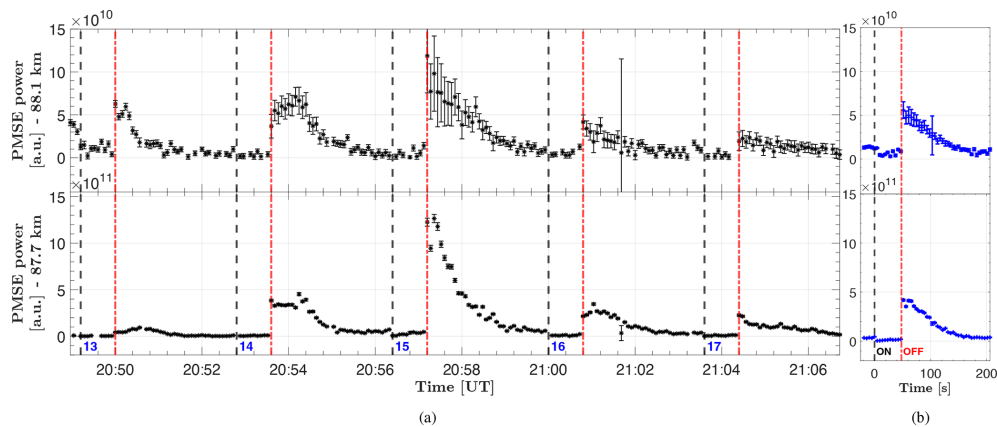
Figure 14. Individual overshoot curves **(a)** from interval A (from Fig. 13) shown with their corresponding altitude average on the right-hand side **(b)**. Heating cycle numbers are shown at the bottom, and the on-and-off period for the averaged cycles is also shown. Note that the y-axis scale for altitude 88 km is an order of magnitude smaller than for the altitude 87.7 km.
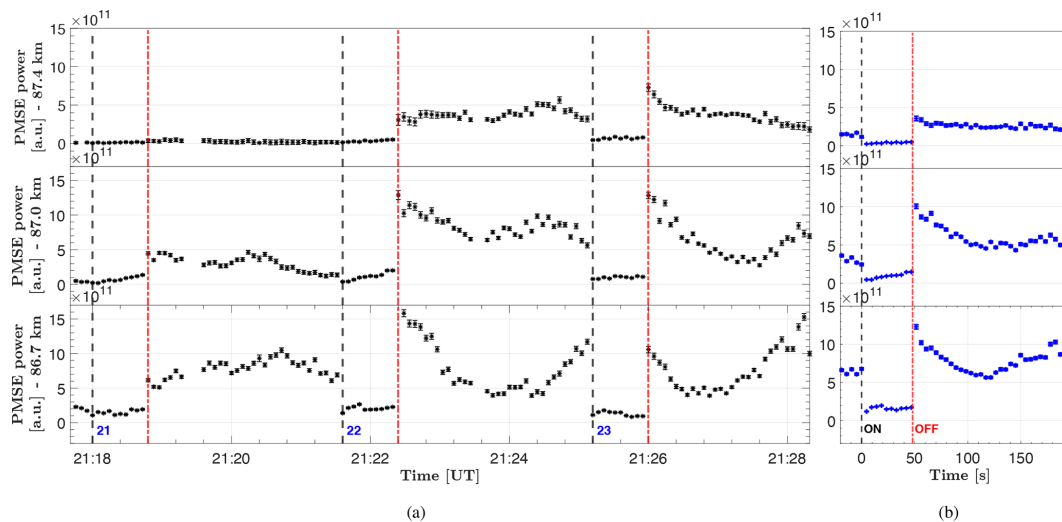

Figure 15. Individual overshoot curves **(a)** from intervals B and C (from Fig. 13) shown with their corresponding altitude average on the right-hand side **(b)**. Heating cycle numbers are shown at the bottom, and the on-and-off period for the averaged cycles is also shown.

The normalized and averaged data from interval A has a higher overshoot than the simulations can produce, where the simulation has an overshoot of around 8.4. At the same time, the observations show an overshoot of almost 9.9. The timescale of the simulation for interval A runs for 300 s, while the observation has a much quicker equalization toward the "background" PMSE value/undisturbed plasma values. For the simulation to reach such a high overshoot, the ratio between dust and electron number density is only at 35 %, and with a heating ratio increase for electron temperature of 8 times the pre-heater value. This would indicate that the dust density is lower than for the other two intervals and that the heating effect is consequently larger. As discussed later, the electrons gain a higher temperature, and charging onto the dust particles is, therefore, more effective, where some dust particles can gain more than a single charge.

A comparison of observations for intervals B and C and their corresponding simulations show a better agreement where the overshoot and relaxation are very similar. For these overshoots to be produced in the simulation, the ratio of dust to electrons must be higher, with 60 % for interval B and 68 % for interval C. The increase at the end of the relaxation period for both intervals is not reproduced in the simulations; this is assumed to be due to the influence of the precipitation that occurs clearly in cycle 24 and is already increasing the background PMSE power in the previous cycles. Compared to the observations, the simulated signals drop slower during the heater-on phase and rise more slowly to the overshoot when the heater is switched off again. The measured response of the PMSE to the heating is instantaneous within the 4.8 s resolution of the data. A possible explanation for this difference is that the numerical model might have miss-
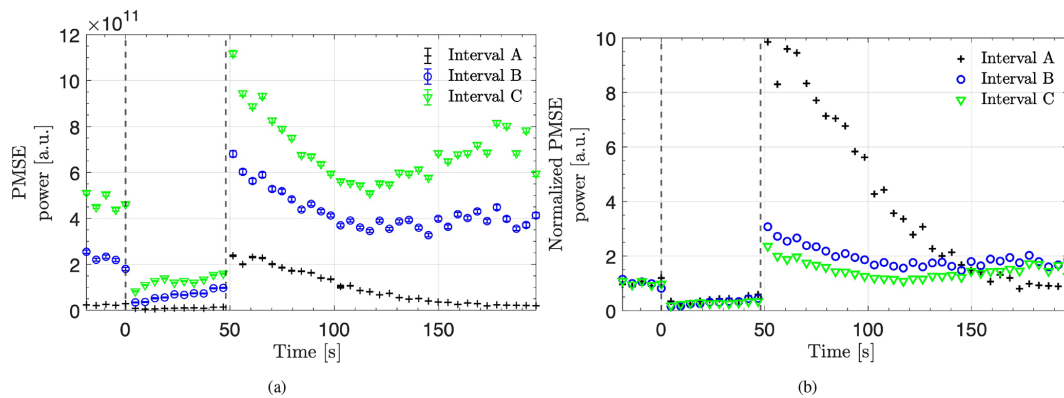
Figure 16. Average overshoot curves for each respective interval **(a)** and normalized average overshoot curves **(b)** for the same intervals. They are normalized with the average of the last five values before the heater was turned on.

ing parameters or processes to simulate this increase. This is in contrast to the decrease we see in most observations, as was discussed previously.

On the left-hand side in Fig. 18a, we can see the average charge number found for the simulation for each respective interval (marked in the figure). For interval A the average charge number reaches a maximum of about 1.38 charges per dust particle during the heater-on phase. This indicates that to achieve such a high overshoot, the charging efficiency of the dust particles needs to be high and that (due to high electron heating temperature) many dust particles will gain more than one negative charge during the heating cycle. Note the longer timescale shown in the simulation for interval A (300 s), indicating that it takes longer for the overall average charge on the dust particles to equalize back to pre-heater values. As was mentioned before, the dust population is much lower for interval A compared to the other two intervals since the ratio of dust to electrons is lower. Consequently, the significant increase in temperature (by a factor of 8) causes a larger average charge number on the dust particles during the heater-on phase. For the other intervals (B and C), the maximum average charge number is less than one during the on phase of the heater for both cases, with interval B being around 0.9 charges per dust. For interval C, the average dust charge lies at about 0.86. This corresponds well with the observed and simulated overshoot curves from Fig. 17, where the higher overshoot is observed in interval B. Thus the average charge number is consequently higher. So the effective charging of the dust during the heater-on phase for these intervals is less than for interval A, and a smaller overshoot is observed.

On the right-hand side in Fig. 18b, we have the ratio of the diffusion time to the charging time scales for each respective interval. Here we can see the variation between the two timescales and how this changes during the heating cycle. For all the intervals, there is an increase in the ratio when the heater turns on, a relaxation during the heater-on period, a sharp increase when the heater is turned off, and a slow decrease during the heater-off period. The significant increase

Table 3. Neutral density for each interval from NRLMSISE-00 atmosphere model (Hedin, 1991) taken at 21:00 UT and the estimated ion–neutral collision frequency (see Ieda, 2020; Cho et al., 1998).

Interval	Neutral density (m^{-3})	v_{in} ($1\,s^{-1}$)
A	1.19×10^{20}	3.44×10^4
B	1.33×10^{20}	3.85×10^4
C	1.48×10^{20}	4.26×10^4

in the heater-on time could be understood as the charging timescale becoming smaller with increased electron charging onto dust particles due to the increased electron temperature. This corresponds well with the increased average electron charge on the dust particles seen in Fig. 18a. Here the average dust charge is highest for interval A, and the ratio of timescales is also highest for this interval, which might indicate a faster charging timescale for that interval than for the other two. The increase at heater turn-off time is also due to a decrease in the charging times; more dust is being charged now by the ion portion of the plasma, which drags the electrons along and causes the observed overshoot. Thus for interval A the simulation of the overshoot curve fits best with a lower ratio of dust particles to electron density. Therefore we might argue that there is more plasma than in the other two intervals. This larger plasma population might then charge the dust more quickly, causing a smaller charging timescale and, consequently, a larger overshoot in interval A.

Another difference could arise in the diffusion timescales in the respective intervals. The diffusion timescale is proportional to the ion–neutral collision frequency, which decreases with decreasing neutral density. Hence in interval A at a higher altitude and with lower neutral density, the diffusion timescale can be shorter than in the other interval (Havnes et al., 2015). The estimated ion–neutral collision frequencies are given in Table 3, which are derived using neutral density from the NRLMSISE-00 atmosphere model (Hedin, 1991).
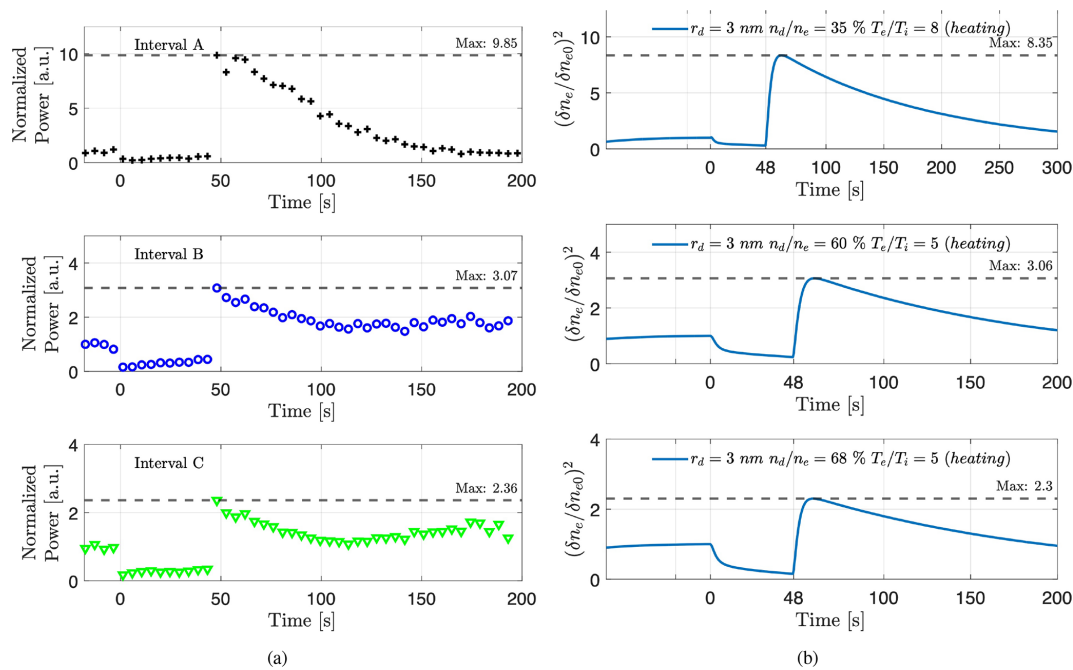
Figure 17. Comparison of the averaged and normalized heating cycles for each interval **(a)** to its corresponding simulation of the overshoot cycles **(b)**. Note the longer timescale of simulation of interval A (longer time needed for simulation to return to equilibrium).

The timescale that is the fastest is the dominating one. So when the heater turns on, the diffusion timescale might be lower for interval A. So when the heater is turned on, the diffusion timescale decreases even more due to its dependence on the temperature ratio (T_e/T_i), and we expect/need a more significant temperature increase for the electrons in interval A to explain such a large overshoot. As the heater is turned on, the charging timescale decreases due to the increase in electron temperature. A larger charging effect is seen in the interval A simulation (average charge number) compared to the other intervals. Consequently, a larger overshoot is seen.

So to summarize, the decreased diffusion timescale for interval A due to reduced neutral density and the significant increase in electron temperature combined help explain the large overshoot seen for interval A. The higher electron temperature could be explained by greater absorption of the heater's energy in the interval. According to Havnes et al. (2015), the amount of electron density per altitude will determine where the heater's energy is absorbed and how much. This generally causes lower altitudes of PMSE to become more heated than higher altitudes. Interval A is at a higher altitude than the other two intervals. Still, the precipitation present in cycle 18 before intervals B and C could cause the altitude regions below these intervals to have a higher electron content and, thus more absorption of the heater's energy below.

5   Discussion and conclusion

For the presented observations, we find that artificial heating affects the PMSE signals during less than half of all the observed heating cycles with a pre-heated PMSE power $R_0 > 10^{10.5}$; the average reduction of the power is about 25 % from the pre-heated value. The cutoff, $R_0 > 10^{10.5}$, excludes cycles that do not show PMSE and cycles being highly influenced by noise. With this criterion, we covered most of the PMSE. However, some very faint ones were excluded, and some were affected by heating and showed large overshoots. We find that the heating has little effect on PMSE during ionospheric conditions with particle precipitation which other authors also see. This is especially so for strong and moderate particle precipitation. We assume that under these conditions of higher ionization, the heating waves are mainly absorbed in lower altitudes, thus not causing a heating effect in the PMSE layer. Often the background ionospheric conditions strongly influence the PMSE profile during one heater cycle, and it is thus challenging to derive a correct relaxation time, which would be an interesting parameter because it depends on the dust conditions present in the layer.

As to the shape of the PMSE modulation curves, the variation of the PMSE during the heater-on period (from R_1 to R_2) is affected by two competing processes: the charging and the diffusion. For the presented observations, most heating cycles display a signal decrease from R_1 to R_2. Less than half of the cycles influenced by heating show an overshoot when the heater is turned off. However, observed overshoots
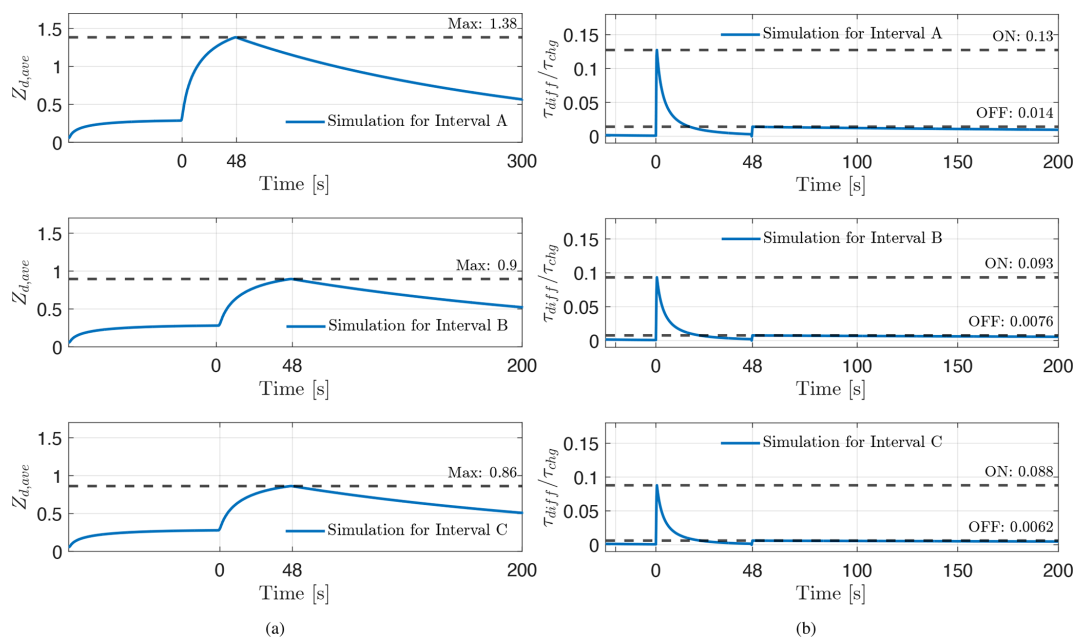
Figure 18. Simulations of average dust charge number on **(a)** for each respective interval and the ratio between the diffusion time and the charging time scales for the same intervals on **(b)**.

are generally high and, in some cases, very high. These high overshoots could be attributed to the dust charge in the presented observations being more strongly influenced by heating, as the influence of photoemission is smaller than during daytime observations.

It is also possible that the size of ice particles and their formation and sublimation rates are different toward the end of the PMSE season; most other heating studies were carried out earlier in the year. A general trend toward a more extended PMSE season (Latteck et al., 2021) and larger particles at PMSE altitudes (at high latitudes) due to increased water vapor content (Lübken et al., 2021) could also cause these recent PMSE observations to show different modulation curves.

The computational overshoot model we considered cannot account for some of the high overshoot cases we observed, and we are unaware of a model that does so. Some processes might need to be included to reproduce these cases of large overshoots. The influence of variation in the ionospheric background with time over the cycles reduces the overshoots and dominates the relaxation phase. We form, however, averaged curves as was done in other studies and compare those to the model calculations. We find that simulations with dust size around 3 nm best fit to all cases considered.

While different electron heating ratios and dust-to-electron densities are needed to match the observational data, a larger temperature heating ratio and a lower dust density are required to best match the large average overshoot observed. The amount of absorption from the heater's energy is impor-

tant in how effectively the electrons can be heated. And since there is precipitation between the first interval with large overshoots and the two other intervals, it stands to reason that the altitudes below the PMSE layer have increased electron content after moderate precipitation. This causes a larger absorption of the heater's energy below the PMSE layer. Therefore a combination of decreased heater energy and lower diffusion time can help explain the large overshoot in the first interval.

We conclude that the presented observations during HF heating confirm that high-power radio waves modulate PMSE amplitudes, with the observed modulation varying on short spatial and temporal scales. The presented observations differ from previous studies since they are done late in the PMSE season and during lower solar illumination (dusk/night). In general, we see both an influence of the heating and an overshoot in about half of the heating cycles, which is somewhat lower than previous observations done earlier in the season around midday. We see very high overshoots compared to previous observations and note that increased PMSE power is connected to smaller overshoots.

Appendix A: Overview of the measurements

Table A1. Days of measurements and selected areas. Symbols t_{start} and t_{end} define the beginning and the end of the area. The altitude of the atmosphere, where the analysis is done, is described with h_{low} and h_{high}.

Day/area	t_{start}	t_{end}	h_{low}	h_{high}
Night of 11/12 August 2018	11 August, 20:00	12 August, 02:00	80.0 km	110.0 km
Area 1	11 August, 21:36	11 August, 22:42	83.4 km	85.6 km
Area 2	11 August, 23:06	12 August, 01:17	86.3 km	90.0 km
Area 3	12 August, 00:00	12 August, 01:28	83.4 km	86.4 km
Night of 15/16 August 2018	15 August, 20:00	16 August, 02:00	80.0 km	110.0 km
Area 1	15 August, 20:06	15 August, 20:25	88.1 km	89.6 km
Area 2	15 August, 20:48	15 August, 21:47	86.3 km	88.5 km
Area 3	15 August, 21:57	15 August, 22:59	83.4 km	87.8 km
Night of 5/6 August 2020	5 August, 20:25	6 August, 00:00	80.0 km	110.0 km
Area 1	5 August, 21:25	11 August, 22:50	82.0 km	88.0 km
Area 2	5 August, 22:50	12 August, 23:50	83.0 km	87.0 km
Area 3	5 August, 22:45	6 August, 00:00	90.0 km	100.0 km
Night of 6/7 August 2020	6 August, 21:15	7 August, 02:00	80.0 km	110.0 km
Area 1	6 August, 22:53	7 August, 02:00	81.5 km	88.0 km
Area 2	6 August, 22:43	6 August, 23:29	91.0 km	94.0 km
Area 3	6 August, 21:15	6 August, 22:15	82.0 km	85.0 km

Table A2. Values of ERP given in the EISCAT heating facility logs from sample beam patterns for each of the measurements for reference. It seems that on 6 August 2020 at around 23:08:25 UT three transmitters changed phases such that the beam became broader, with about 360 MW X-mode and 17 MW O-mode, which remained so until the end, which is why we have 359 MW X-mode at 01:07:13 UT (7 of August).

Day	Time (UT)	ERP
11 August 2018	20:50:13	560 MW
12 August 2018	01:20:13	541 MW
15 August 2018	20:06:19	568 MW
16 August 2018	00:39:49	580 MW
5 August 2020	20:47:01	495 MW
6 August 2020	19:29:58	567 MW
7 August 2020	01:07:13	359 MW

References

Belova, E., Smirnova, M., Rietveld, M., Isham, B., Kirkwood, S., and Sergienko, T.: First observation of the overshoot effect for polar mesosphere winter echoes during radiowave electron temperature modulation, Geophys. Res. Lett., 35, https://doi.org/10.1029/2007GL032457, 2008.

Biebricher, A., Havnes, O., Hartquist, T., and LaHoz, C.: On the influence of plasma absorption by dust on the PMSE overshoot effect, Adv. Space Res., 38, 2541–2550, 2006.

Chilson, P. B., Belova, E., Rietveld, M. T., Kirkwood, S., and Hoppe, U.-P.: First artificially induced modulation of PMSE using the EISCAT heating facility, Geophys. Res. Lett., 27, 3801–3804, 2000.

Cho, J. Y. and Röttger, J.: An updated review of polar mesosphere summer echoes: Observation, theory, and their relationship to noctilucent clouds and subvisible aerosols, J. Geophys. Res.-Atmos., 102, 2001–2020, 1997.

Cho, J. Y., Sulzer, M. P., and Kelley, M. C.: Meteoric dust effects on D-region incoherent scatter radar spectra, J. Atmos. Sol.-Terr. Phy., 60, 349–357, 1998.

Czechowsky, P., Rüster, R., and Schmidt, G.: Variations of mesospheric structures in different seasons, Geophys. Res. Lett., 6, 459–462, 1979.

Dalin, P., Kirkwood, S., Moström, A., Stebel, K., Hoffmann, P., and Singer, W.: A case study of gravity waves in noctilucent clouds, Ann. Geophys., 22, 1875–1884, https://doi.org/10.5194/angeo-22-1875-2004, 2004.

Ecklund, W. and Balsley, B.: Long-term observations of the Arctic mesosphere with the MST radar at Poker Flat, Alaska, J. Geophys. Res., 86, 7775–7780, 1981.

Giono, G., Strelnikov, B., Asmus, H., Staszak, T., Ivchenko, N., and Lübken, F.-J.: Photocurrent modelling and experimental confirmation for meteoric smoke particle detectors on board atmospheric sounding rockets, Atmos. Meas. Tech., 11, 5299–5314, https://doi.org/10.5194/amt-11-5299-2018, 2018.

Gunnarsdottir, T. L., Poggenpohl, A., Mann, I., Mahmoudian, A., Dalin, P., Haeggstroem, I., and Rietveld, M., Code for: Modulation of polar mesospheric summer echoes (PMSEs) with high-frequancy heating during low solar illumination, DataverseNO, V1., [code], https://doi.org/10.18710/NGISOA, 2022.

Havnes, O.: Polar Mesospheric Summer Echoes (PMSE) overshoot effect due to cycling of artificial electron heating, J. Geophys. Res., 109, https://doi.org/10.1029/2003JA010159, 2004.

Havnes, O., La Hoz, C., Rietveld, M. T., Kassa, M., Baroni, G., and Biebricher, A.: Dust charging and density conditions deduced from observations of PMWE modulated by artificial electron heating, J. Geophys. Res.-Atmos., 116, https://doi.org/10.1029/2011JD016411, 2011.

Havnes, O., Pinedo, H., La Hoz, C., Senior, A., Hartquist, T. W., Rietveld, M. T., and Kosch, M. J.: A comparison of overshoot modelling with observations of polar mesospheric summer echoes at radar frequencies of 56 and 224 MHz, Ann. Geophys., 33, 737–747, https://doi.org/10.5194/angeo-33-737-2015, 2015.

Hedin, A. E.: Extension of the MSIS thermosphere model into the middle and lower atmosphere, J. Geophys. Res., 96, 1159–1172, 1991.

Hervig, M. E., Deaver, L. E., Bardeen, C. G., Russell III, J. M., Bailey, S. M., and Gordley, L. L.: The content and composition of meteoric smoke in mesospheric ice particles from SOFIE observations, J. Atmos. Sol.-Terr. Phy., 84, 1–6, 2012.

Hunten, D. M., Turco, R. P., and Toon, O. B.: Smoke and dust particles of meteoric origin in the mesosphere and stratosphere, J. Atmos. Sci., 37, 1342–1357, 1980.

Ieda, A.: Ion-neutral collision frequencies for calculating ionospheric conductivity, J. Geophys. Res., 125, https://doi.org/10.1029/2019JA027128, e2019JA027128, 2020.

Kassa, M., Havnes, O., and Belova, E.: The effect of electron bite-outs on artificial electron heating and the PMSE overshoot, Ann. Geophys., 23, 3633–3643, https://doi.org/10.5194/angeo-23-3633-2005, 2005.

Kavanagh, A., Honary, F., Rietveld, M., and Senior, A.: First observations of the artificial modulation of polar mesospheric winter echoes, Geophys. Res. Lett., 33, https://doi.org/10.1029/2006GL027565, 2006.

Latteck, R., Renkwitz, T., and Chau, J. L.: Two decades of long-term observations of polar mesospheric echoes at 69° N, J. Atmos. Sol.-Terr. Phy., 216, 105576, https://doi.org/10.1016/j.jastp.2021.105576, 2021.

Lehtinen, M. S. and Huuskonen, A.: General incoherent scatter analysis and GUISDAP, J. Atmos. Sol.-Terr. Phy., 58, 435–452, 1996.

Lübken, F.-J.: Thermal structure of the Arctic summer mesosphere, J. Geophys. Res.-Atmos., 104, 9135–9149, 1999.

Lübken, F.-J., Baumgarten, G., and Berger, U.: Long term trends of mesospheric ice layers: A model study, J. Atmos. Sol.-Terr. Phy., 214, 105378, https://doi.org/10.1016/j.jastp.2020.105378, 2021.

Mahmoudian, A., Scales, W. A., Kosch, M. J., Senior, A., and Rietveld, M.: Dusty space plasma diagnosis using temporal behavior of polar mesospheric summer echoes during active modification, Ann. Geophys., 29, 2169–2179, https://doi.org/10.5194/angeo-29-2169-2011, 2011.

Mahmoudian, A., Senior, A., Scales, W., Kosch, M. J., and Rietveld, M.: Dusty space plasma diagnosis using the behavior of polar mesospheric summer echoes during electron precipitation events, J. Geophys. Res., 123, 7697–7709, 2018.

Mahmoudian, A., Kosch, M. J., Vierinen, J., and Rietveld, M. T.: A new technique for investigating dust charging in the PMSE source region, Geophys. Res. Lett., 47, e2020GL089639, https://doi.org/10.1029/2020GL089639, 2020.

Mann, I., Häggström, I., Tjulin, A., Rostami, S., Anyairo, C., and Dalin, P.: First wind shear observation in PMSE with the tristatic EISCAT VHF radar, J. Geophys. Res., 121, 11–271, 2016.

Megner, L., Rapp, M., and Gumbel, J.: Distribution of meteoric smoke – sensitivity to microphysical properties and atmospheric conditions, Atmos. Chem. Phys., 6, 4415–4426, https://doi.org/10.5194/acp-6-4415-2006, 2006.

Myrvang, M., Baumann, C., and Mann, I.: Modelling the influence of meteoric smoke particles on artificial heating in the D-region, Ann. Geophys., 39, 1055–1068, https://doi.org/10.5194/angeo-39-1055-2021, 2021.

Pinedo, H., La Hoz, C., Havnes, O., and Rietveld, M.: Electron–ion temperature ratio estimations in the summer polar mesosphere when subject to HF radio wave heating, J. Atmos. Sol.-Terr. Phy., 118, 106–112, https://doi.org/10.1016/j.jastp.2013.12.016, 2014.

Rapp, M. and Lübken, F.-J.: Electron temperature control of PMSE, Geophys. Res. Lett., 27, 3285–3288, 2000.

Rapp, M. and Lübken, F.-J.: Polar mesosphere summer echoes (PMSE): Review of observations and current understanding, Atmos. Chem. Phys., 4, 2601–2633, https://doi.org/10.5194/acp-4-2601-2004, 2004.

Rapp, M. and Thomas, G. E.: Modeling the microphysics of mesospheric ice particles: Assessment of current capabilities and basic sensitivities, J. Atmos. Sol.-Terr. Phy., 68, 715–744, 2006.

Rietveld, M., Kohl, H., Kopka, H., and Stubbe, P.: Introduction to ionospheric heating at Tromsø—I. Experimental overview, J. Atmos. Sol.-Terr. Phy., 55, 577–599, 1993.

Rietveld, M. T., Senior, A., Markkanen, J., and Westman, A.: New capabilities of the upgraded EISCAT high-power HF facility, Radio Sci., 51, 1533–1546, 2016.

Rosinski, J. and Snow, R.: Secondary particulate matter from meteor vapors, J. Atmos. Sci., 18, 736–745, 1961.

Scales, W. and Mahmoudian, A.: Charged dust phenomena in the near-Earth space environment, Rep. Prog. Phys., 79, 106802, https://doi.org/10.1088/0034-4885/79/10/106802, 2016.

Strelnikova, I. and Rapp, M.: Majority of PMSE spectral widths at UHF and VHF are compatible with a single scattering mechanism, J. Atmos. Sol.-Terr. Phy., 73, 2142–2152, 2011.

Tanaka, K. K., Mann, I., and Kimura, Y.: Formation of ice particles through nucleation in the mesosphere, Atmos. Chem. Phys., 22, 5639–5650, https://doi.org/10.5194/acp-22-5639-2022, 2022.

Tjulin, A.: EISCAT experiments, EISCAT Scientific Association, (March), https://eiscat.se/wp-content/uploads/2022/02/Experiments_v20220203.pdf (last access: 29 September 2021), 2017.

Ullah, S., Li, H., Rauf, A., Meng, L., Wang, B., and Wang, M.: Statistical study of PMSE response to HF heating in two altitude regions, Earth, Planet. Space, 71, 1–14, 2019.

PAPER III

Influence of Meteoric Smoke Particles on the Incoherent Scatter Measured with EISCAT VHF

Gunnarsdottir, T. L., Mann, I., Feng, W., Huyghebaert, D. R., Haeggstroem, I., Ogawa, Y., Saito, N., Nozawa, S. and Kawahara T. D., Annales Geophysicae, Preprint, 2023

Influence of Meteoric Smoke Particles on the Incoherent Scatter Measured with EISCAT VHF

Tinna L. Gunnarsdottir[1], Ingrid Mann[1], Wuhu Feng[2], Devin R. Huyghebaert[1], Ingemar Haeggstroem[3], Yasunobu Ogawa[4], Norihito Saito[5], Satonori Nozawa[6], and Takuya D. Kawahara[7]

[1]Department of Physics and Technology, UiT The Arctic University of Norway, Tromsø, Norway
[3]EISCAT Scientific Association, Kiruna, Sweden
[4]National Institute of Polar Research, JAPAN
[6]Institute for Space-Earth Environmental Research; Nagoya University, Japan
[2]National Centre for Atmospheric Science, University of Leeds, United Kingdom
[5]RIKEN Center for Advanced Photonics, RIKEN, Japan
[7]Faculty of Engineering, Shinshu university, Japan

Correspondence: Ingrid Mann (ingrid.b.mann@uit.no)

Abstract. Meteoric ablation in the Earth's atmosphere produces particles of nanometer-size and larger. These particles can become charged and influence the charge balance in the D-region (60-90 km) and the incoherent scatter observed with radar from there. Radar studies have shown that if enough dust particles are charged, they can influence the received radar spectrum below 100 km, provided the electron density is sufficiently high ($>10^9$ m^3). Here, we study an observation made with the EISCAT VHF radar on 9 January 2014 during strong particle precipitation so that incoherent scatter was observed down to almost 60 km altitude. We found that the measured spectra were too narrow in comparison to the calculated spectra. Adjusting the collision frequency provided a better fit in the frequency range $\pm$ 10-30 Hz. However, this did not lead to the best fit in all cases, especially not for the central part of the spectra in the narrow frequency range of $\pm$ 10 Hz. By including a negatively charged dust component, we obtained a better fit for spectra observed at altitudes 75-85 km, indicating that dust influences the incoherent scatter spectrum at D-region altitudes. The observations at lower altitudes were limited by the small amount of free electrons, and observations at higher altitudes were limited by the height resolution of the observation. Inferred dust number densities range from a few particles up to $10^4 cm^{-3}$ and average sizes range from approximately 0.6 to 1 nm. We find an acceptable agreement with the dust profiles calculated with the WACCM-CARMA model. However, these do not include charging, which is also based on models.

1 Introduction

Cosmic dust material enters Earth's atmosphere each day, globally around 25.0 ± 7.0 tonnes/day as recently suggested (Hervig et al., 2021). Much of this material ablates in the altitude region of 70-110 km (Plane, 2012). This meteoric material recondenses to form nanometer-sized solid dust called meteoric smoke particles (Hunten et al., 1980; Rosinski and Snow, 1961). These particles influence the charge balance in the D-region ionosphere (Baumann et al., 2015); and they possibly facilitate the nucleation of ice particles in the cold summer mesopause (Rapp and Lübken, 2004). The distribution of meteoric smoke parti-

cles is influenced by several processes, the influence of the atmospheric background wind being particularly important (Megner et al., 2006). Model calculations show that due to atmospheric transport, the number density and size distribution of meteoric smoke particles vary with season in the polar regions (Megner et al., 2006, 2008; Bardeen et al., 2008). Their small size has made it difficult to observe them directly, and many observation techniques only manage to infer their existence. For example, in-situ rocket measurements showed a depletion of the electron density in the main altitude ranges of meteoric smoke particles. It is assumed that charge neutrality is preserved as negative charges accumulate on the dust, and observed electron deficits are interpreted as an indication of dust particles (Friedrich et al., 2012). Charged dust particles are also measured by rocket-borne Faraday probes; the interpretation of these measurements is complicated, however, since the charge and fragmentation of the particles can also occur in the detector (Antonsen et al., 2017).

In the altitude range where these dust particles can be found, the ionospheric parameters are measured with radars by means of incoherent scatter. The incoherent scatter comes from the scattering of electrons that are coupled through charge oscillations to the other ionospheric components, including positive ions, negative ions, and charged dust; in addition, the collisions with the neutral atmosphere affect the incoherent scatter because they damp the charge oscillations, as the plasma is collisionally dominated. The role of charged dust particles in incoherent scatter has been studied so far only a handful of times. To describe the incoherent scatter from the D-region ionosphere, an approach was developed that considers charged dust in addition to negative and positive ions (Cho et al., 1998b). This model approach has been used to derive estimates from incoherent scatter observations of dust size and positively charged dust number density (Rapp et al., 2007; Strelnikova et al., 2007; Fentzke et al., 2009). In recent work (Gunnarsdottir and Mann, 2021), we extended the description by Cho et al. (1998b) including a dust charge distribution; and investigated the influence of charged dust on incoherent scatter for the ionospheric conditions at the EISCAT VHF radar site. We have found that conditions of high electron density in the winter months are best for studying the dust signatures in the spectrum. We also suggested supporting the analysis by using temperature information from independent measurements. This is due to the large influence that temperature has on the spectrum, of the same order as charged dust.

In this work, we present an analysis of incoherent scatter observations selected from the EISCAT VHF radar data archive to investigate the influence of charged dust on the spectrum and we attempt to derive a dust distribution. The paper is structured as follows. In Section 2 we briefly describe the incoherent scatter model used and the radar data analysis approach. In Section 3 we describe the data used including radar observations, lidar observations, temperature and atmospheric models, the dust number densities obtained from a simulation run, and the dust charging model. Section 4 includes the data processing and analysis and Section 5 contains the conclusion.

2   Model of the incoherent scatter spectrum and selection of the observational data

If the number density of charged dust particles in the ionosphere is sufficiently large, they form dusty plasma and participate in incoherent scatter and influence the spectrum. Cho et al. (1998b) extended the incoherent scatter theory by Mathews (1978) to include charged dust. They developed an N-fluid description of the ionospheric plasma that includes a polydisperse charged dust component in addition to positive and negative ions. The shape of the radar spectrum depends on the electron density,

mean ion mass, neutral density, dust size, dust charge distribution, and temperature of all constituents. The presence of positive dust particles or large (>0.5 nm) negative particles causes the spectrum to narrow, while smaller (<0.5 nm) negative particles cause the spectrum to broaden. Dust only affects the spectrum if its charged population has a high enough number density compared to the electron density, so it changes the electron diffusion rate and consequently the spectrum (Cho et al., 1998b; Rapp et al., 2007). The plasma in the D-region is collisionally dominated, and so collisions with the neutral atmosphere affect incoherent scatter spectrum because they dampen charge oscillations. Furthermore, because the neutral density is high in the D-region, the electrons and ions have temperatures approximately equal to those of the neutral gas.

Gunnarsdottir and Mann (2021) extended the models developed by Cho et al. (1998b) to include dust with a charge distribution. This approach was used and combined with a dust charge distribution model (Baumann et al., 2015) to calculate radar spectra and analyze the effect of charged dust on the spectra throughout the year. Comparison of the calculated spectra revealed that the influence of dust was most prominent in the winter spectra. Therefore, winter months in combination with a high electron content in the ionosphere were the criteria for selecting the observation data.

So far, the contribution of charged dust to incoherent radar scatter has been investigated only in a few cases. Most of these works investigated radar autocorrelation measurements. By fitting them with an adjusted Lorentz profile, a single dust size and the number density of positively charged dust were derived (Rapp et al., 2007; Strelnikova et al., 2007; Fentzke et al., 2009). Here, we consider the frequency spectrum, which is the Fourier transform of the autocorrelation function, and compare it directly to the calculated spectra. We calculate the spectra using the neutral temperature as the temperature of all components; and obtain the neutral temperatures from available LIDAR observations or otherwise from a model. We used dust distribution data calculated with the WACCM-CARMA model (Bardeen et al., 2008), dust charging from model assumptions, and neutral densities from an empirical model of the upper atmosphere nrlmsise-00 (Hedin, 1991). To obtain the best fit, we vary the ion-neutral collision frequency and the amount of charged dust with the size distribution given by the WACCM-CARMA model.

3 Observational and atmospheric model data

3.1 EISCAT VHF measurement

We chose an observation from 9 January 2014, 8-22 UT, with the EISCAT VHF radar (224 MHz) where a high amount of particle precipitation is present; see figure 1. This large amount of particle precipitation could be connected to the strong solar proton event on 6-9 January 2014 (NASA). Here, we see particle precipitation going below 80 km and enhanced electron densities measured by the radar down to 65 km during the day. Two small dots, around 68 km (13:30 UT) and 78 km (21:30 UT), are not included in the data analysis, as they are unlikely to be from incoherent scatter.
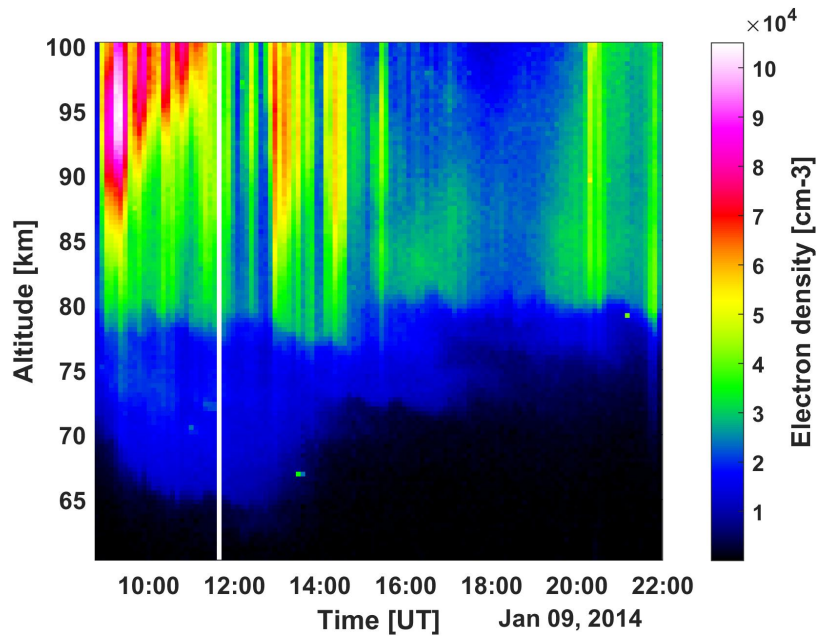
Figure 1. Electron density measured with the EISCAT VHF radar at 9 January 2014 from around 8-22 UT. White line in between 11-12 UT shows data removed due to some artifact in the measurement.
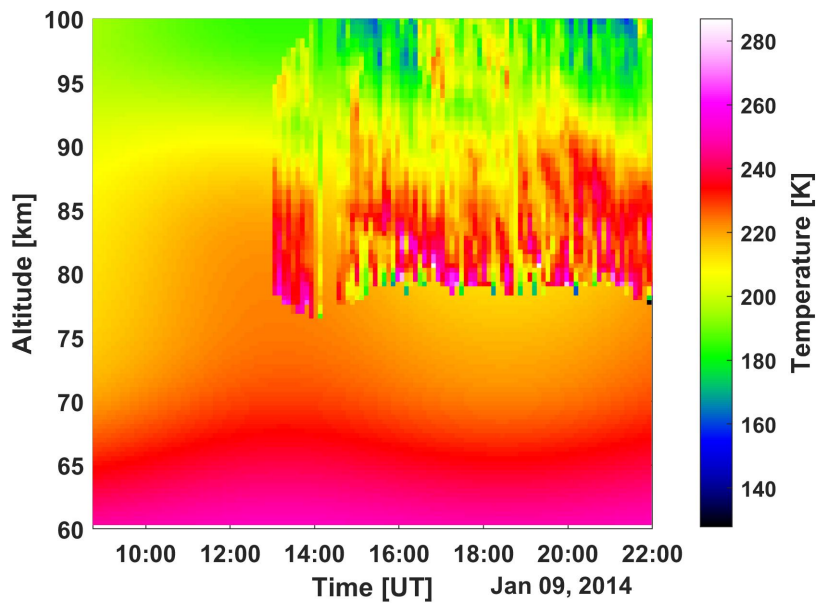

Figure 2. LIDAR temperature measured by the Tromsø Sodium Lidar on 9 Jan 2014 from 08-22 UT. Resolution is 6 min temporal and 0.5 km altitudinal. Only data points with error <5K are included in the plot and the data analysis. Where LIDAR temperature is not available we include model temperature from the nrlmsise-00 model.

4

3.2 LIDAR measurements of temperature.

In our previous study (Gunnarsdottir and Mann, 2021) we showed that the spectrum is highly influenced by atmospheric
temperature, so to accurately estimate the spectrum, we used the temperature measured by the Tromsø sodium LIDAR (Nozawa
et al., 2014). The LIDAR measured the temperature for only part of the observation time; thus we include the model temperature
from the nrlmsise-00 model when there are no available LIDAR measurements. An overview of the temperature measured
with the LIDAR and the added model temperature is given in figure 2. Here, we have only included LIDAR temperature
measurements that have measurement error <5K. Temperature differences of, for example, 20-30 K can alter the spectrum in
a similar way as the charged dust does, and we therefore want to minimize the influence of the temperature. The comparison
of the LIDAR measurements with the model temperature shows that this sometimes deviates and therefore all dust densities
derived by using the model temperature have an additional uncertainty.

3.3 Dust density profiles from WACCM-CARMA

To fit the data with a charged dust profile, we start with number densities from a global atmospheric dust model (Brooke et al.,
2017; Plane et al., 2015; Hervig et al., 2017). The height profiles of meteoric smoke particles are derived from the Whole
Atmosphere Community Climate Model (WACCM) (based on Hervig et al. (2017)) with a sectional microphysics model,
the Community Aerosol and Radiation Model for Atmospheres (CARMA) (Bardeen et al., 2008). A meteoric smoke particle
density of 2 g/cm^3 was assumed (Saunders and Plane, 2011). The model simulation was free-running for 21 years from 2000,
enough time to reach a steady state of the model data. It used version 1 of the Community Earth System Model (CESM1) as a
common numerical framework (Hurrell et al., 2013). The model run is atmosphere-only simulations with interactive chemistry
and aerosol forced with observed sea surface temperatures, etc. (Marsh et al., 2013). The simulation has a horizontal resolution
of 1.9° (in latitude) × 2.5° (in longitude) on 66 σ-pressure vertical levels (1000-5.96×10$^-$6 hPa). The vertical resolution in
the mesosphere and lower thermosphere is about 3.5 km. The resulting dust profiles have 28-size bins, with 0.2 nm being the
smallest and 102.4 nm the largest, with monthly average dust densities. Figure 3 shows the dust densities for 14 size bins(0.2
to 4.032 nm) for the altitude range 60-100 km in the first three panels. The last panel shows the total dust number density for
the entire altitude range (including all sizes with number densities greater than 1).

Although the shown number density is the total average monthly number density for January, we do not know how much it is
charged at any given time. Most rocket observations and model calculations suggest that dust particles are probably negatively
charged (Rapp et al., 2012; Baumann et al., 2013). In the absence of direct observations, we use the charging probability based
on model calculations Antonsen (2019) and combine this with the dust number densities given by the WACCM-CARMA
model. The charging probabilities are shown in Figure A2 in the Appendix. Based on these values, the smallest dust remains
uncharged (<0.5 nm) and the resulting number density profiles of negatively charged particles in the 0.5-4 nm size range are
shown in Figure 4. Here, the smallest particle sizes have a lower charging probability than the larger particles. Due to the
large amount of particle precipitation seen in the observation, there might be additional charging processes occurring that,
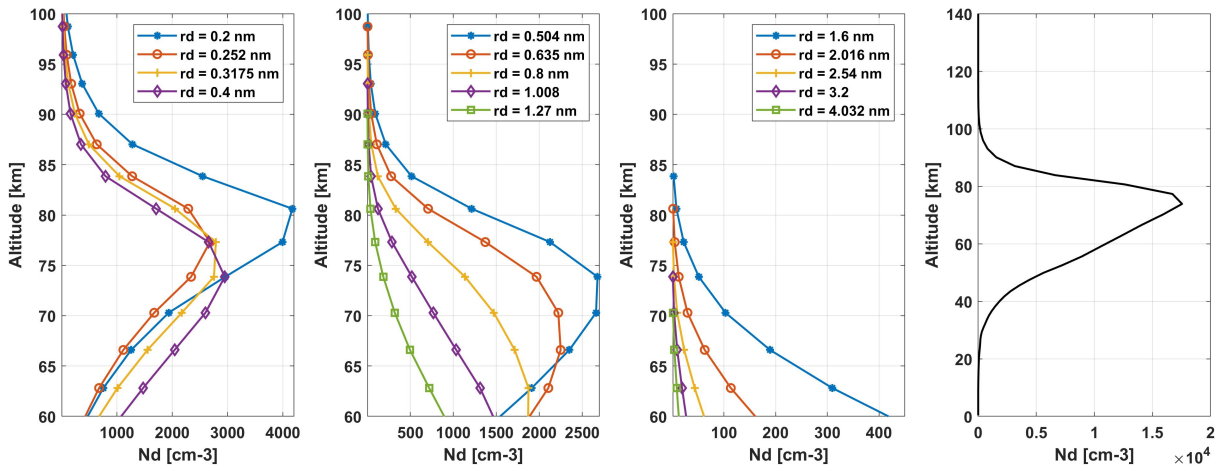
Figure 3. Dust distribution for sizes 0.2 - 4.032 nm in the altitude range 60-100 km from the WACCM-CARMA model shown in the first three panels. Last panels shows the total number density of dust for all sizes in the altitude range 0-140 km. Monthly average data for January with longitude and latitude closes to the EISCAT site.

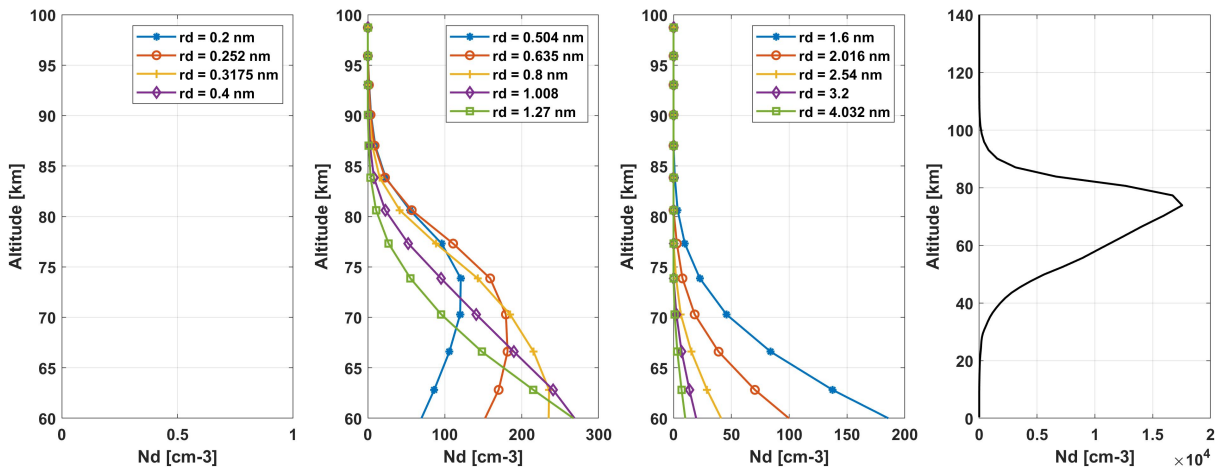115 without extensive modeling, we can only guess at. In a later section, we also discuss results obtained when using other charge distributions or charge polarity.

Figure 4. Estimated negatively charged dust distribution. We assume that dust particles below 0.5 nm have zero charge state and that sizes in the range 0.504-4.032 nm are charged according to the charge probability in Figure A2 for dust sizes without photodetachment.

4 Data processing and analysis

The dust signature in the radar data is quite small and difficult to detect, and many influences on the radar measurements can mask these dust signatures. Therefore, careful data processing is required to minimize noise that could distort the spectra.
120 Unwanted signals include echoes of meteors and satellites that pass through the radar beam. Using the Grand Unified Incoherent Scatter Design and Analysis Package (GUSIDAP) (Lehtinen and Huuskonen, 1996) we can improve the data by removing the presence of meteors in the raw signals. GUSIDAP has a built-in code that removes data influenced by satellites. This code can also be used to remove meteors by increasing the threshold of what is considered "bad data". The raw data are then run through the EISCAT Real Time Graph (EISCAT). to obtain the spectra. Here, we have chosen a time resolution of about 6.5 minutes and
125 the usual 360 m altitude resolution for the resulting spectra. Examples of spectra measured at two selected times of observation are shown in figure 5. Here, one can see some interesting features of the spectra. In the lower region, the spectrum appears to narrow at certain altitudes before widening with altitude, as expected. Above 90 km the spectrum becomes increasingly noisy due to large range resolution, and mostly below 75 km (after 14 UT) the electron density present is to low to discern a good radar signal. In the time interval 9-14 UT the increased electron density allows some spectra to be derived below 75 km. In
130 further data analysis, we remove cases that are entirely noisy, and smooth the cases that are heavily influenced by noise (using a Savitzky-Golay filter).
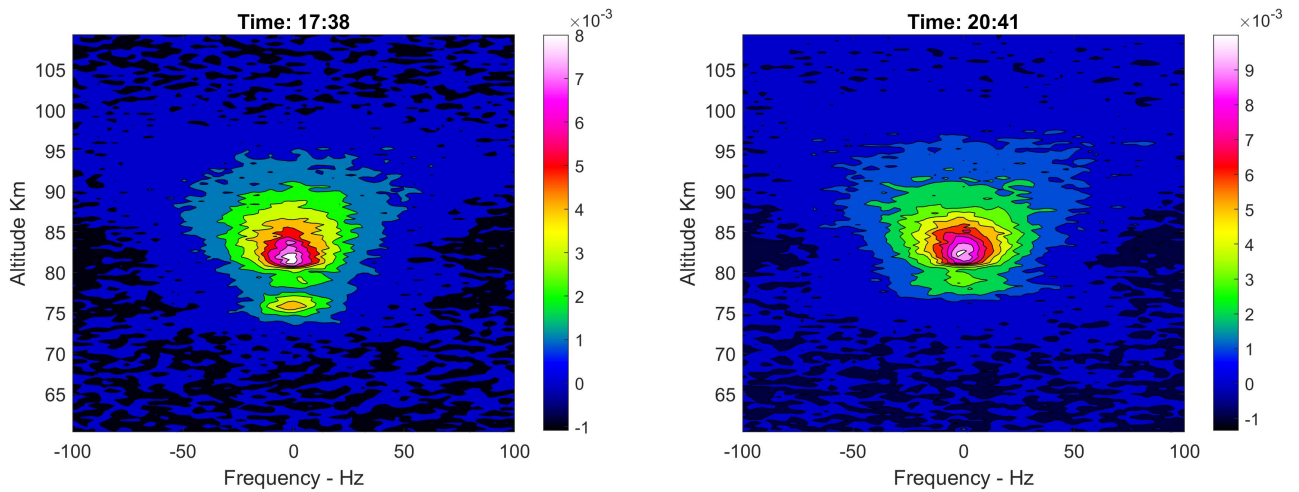
Figure 5. Measured spectrum by the EISCAT VHF for times 17:38 UT on the left and 20:41 UT on the right. The altitude range shown is 60-110 km. The spectrum is shown in a contour plot with arbitrary color-scales.

4.1 Modeled spectra without a dust component - adjusting the collision frequency

We first start by comparing the measured spectra with modeled spectra, where we assume that there is no dust component. An example of this is given in Figure 6, where we can see that the modeled spectra are too broad compared to the measured spectra

135 in the frequency range ± 10-30 Hz. The presence of large charged dust will narrow the spectrum by introducing a narrow peak on top of the normal broad background spectrum, and thus consequently decrease the spectral width. Here, we see, however, that many cases of measured spectra are actually narrower than predicted. However, they are narrower in the frequency range up to ± 50 Hz. And this cannot be fully explained by the presence of dust. It was, however, seen also in other observations. Recently, Thomas et al. (2023) noticed that the collision frequency modeled in the D region is off by a certain factor, which can

140 help explain this discrepancy between observation and model. Therefore, we run the model again with varying multipliers of the collision frequency (range used 0.1 to 3) and determine the best fit to the data in the frequency range ± 50 Hz. This results in the left panel of Figure 7, where the color scale represents the best-fit multiplier for the collision frequency with respect to the observed spectrum. The right panel shows the modeled ion-neutral collision frequency with this adjustment. Using the adjusted collision frequency when modeling the spectra, we get a better agreement with the measured spectra. This can be seen

145 in Figure 6 as the black line with circles, where for this particular case we have a very good agreement with the observation.
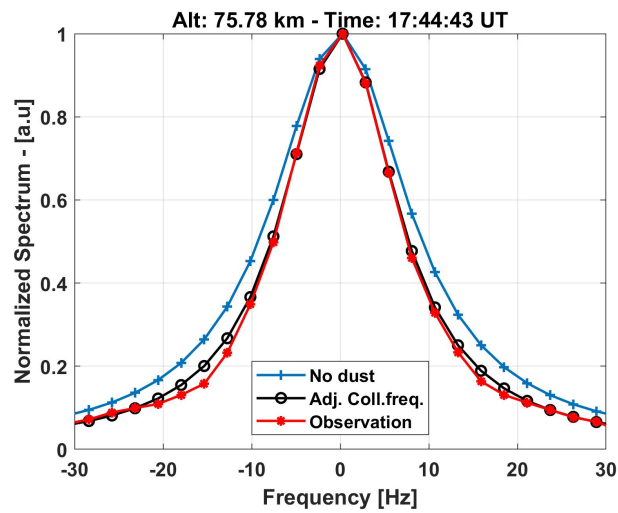
Figure 6. Comparison of a selected case of observed spectra (red circles) with a model calculation of a spectrum without a dust component (blue crosses) and the same model calculation with an adjusted collision frequency (black empty circles).

In Figure 8 we compare the estimated ion-neutral collision frequency (which depends on the neutral density and ion mass) using the neutral density from the nrlmsise-00 model, the adjusted collision frequency using the adjustment found above, and the collision frequency estimated from the IS spectrum fitting using GUISDAP. It is often difficult to derive the collision frequency from the IS spectrum fitting in the D- and E-regions, so we integrated the IS spectrum for 1 hour and derived it as

150 accurately as possible. The other two estimated collision frequencies were then averaged over 1 hour and compared with the GUISDAP results: the collision frequencies derived from the IS spectrum fit are sometimes an order of magnitude higher than the other two at 70-85 km altitudes (e.g. 10, 16 and 20 UT). However, due to the large IS fitting errors, the other two collision frequencies are also included in their error ranges.
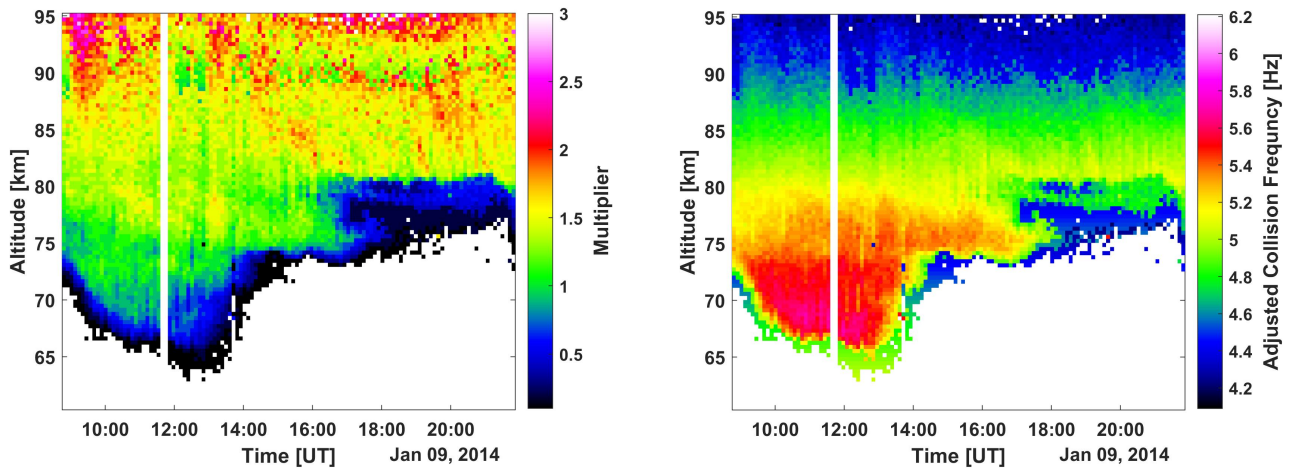
8

Figure 7. Estimated adjustment of the collision frequency where the left panels shows the factor needed to multiply the ion-neutral collision frequency to better fit the spectrum in the frequency range ± 50 Hz. And on the right is the adjusted model ion-neutral collision frequency.
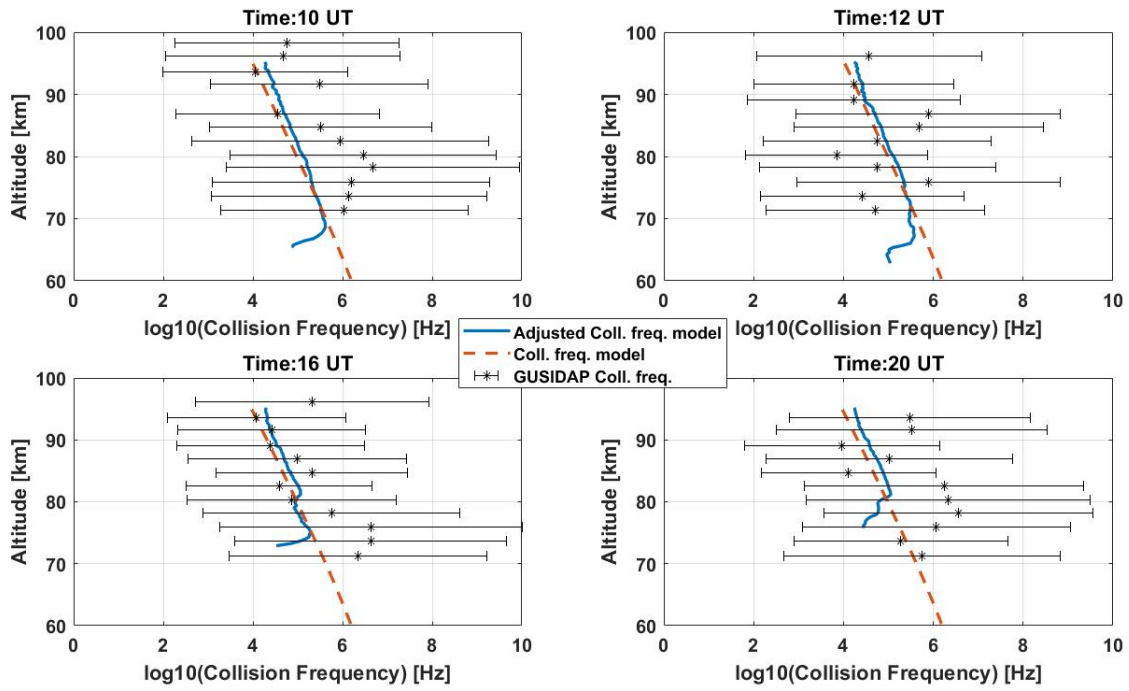

Figure 8. Comparison of the estimated model ion-neutral collision frequency (blue line), adjusted collision frequency (red dashed line) using the adjustment found above, and the collision frequency estimated from the IS spectrum fitting using GUISDAP (black stars with errorbars). See appendix Figure A3 for more detail on derived collision frequency.

4.2 Including dust in modeled spectrum

155 After adjusting the collision frequency, several observed spectra fit well with the modeled spectra in the frequency range $\pm$ 10-30 Hz, but often not in the most inner part of the spectrum, in the frequency range $\pm$ 10 Hz. This range is where we would expect a dust component to influence the spectrum (Cho et al., 1998a). We include a dust component in the modeled spectrum, with charged dust number densities shown in Figure 4 based on model assumptions outlined above to examine whether this will lead to a better fit in the frequency range $\pm$ 10 Hz. Due to the increased electron density seen during the observation,

160 we ran model calculations with several different variations of this number density. In this way, we could investigate whether a much larger amount of charged dust is required to fit the observed spectra or a smaller one. Figure 9 on the left shows an example spectrum where including a dust component leads to a better agreement with the observation. The charged dust number densities used to calculate the spectrum are shown on the left.

When including a charged dust component in the model, we assume that charge neutrality is kept. In practice, this means

165 that, since we assume the dust is negatively charged, we increase the ion population in the model to be equal to the sum of the number of charged dust components and the total electron density measured by the radar (derived by GUISDAP). We also assume a dust mass density of 2 g/cm^-3 (same as the WACCM-CARMA model). The ion mass is kept at 31 amu, which should be the mean ion mass above 80 km. Below 80 km the mean mass is assumed to vary for both negative and positive ions.
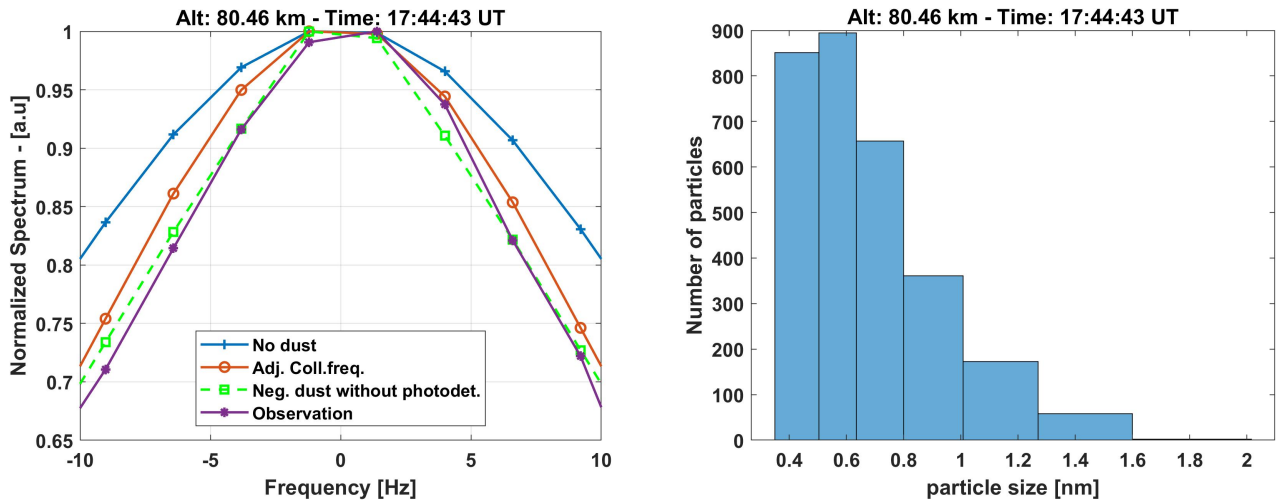
Figure 9. Comparison of a selected case of observed spectra (purple circles) with a model calculation of a spectrum without a dust component (blue crosses), the same model calculation with an adjusted collision frequency (red empty circles) and the a model calculation with and adjusted collision frequency as well as a charged dust component (green squares) is shown on the left. Time and altitude of the selected case is given above the figure. On the right is the associated size distribution (cm^-3) of the charged dust used in the model calculation on the left.

For each individual observed spectrum, we calculate spectra assuming different densities of negatively charged dust and

170 find the best fit to the observation. This is then compared to the model calculation of a spectrum without dust and to a model calculation with an adjusted collision frequency. In Figure 10 we show the cases where including dust in the modeled spectrum

results in the best fit of these three cases. The total number density (log scale) of dust assumed for the fit is given. As one can see, including dust in the model calculations fits better than the other two cases in quite a few cases in the altitude ranges of 75-85 km. After 17 UT the measured electron density is too low to obtain good measurements of the spectra at the lower altitudes. A few cases are seen when the electron density is quite low below 75 km; here, however, the associated measurement error of the electron density is high and the number density of dust is low compared to the electron density, so that these fits are not very reliable (see the right panel of Figure A4 in the Appendix). The lack of knowledge of an exact mean ion mass could also introduce an additional error. The same can be said for fits above 90 km, where the range resolution is much poorer and the measured spectra are quite noisy.
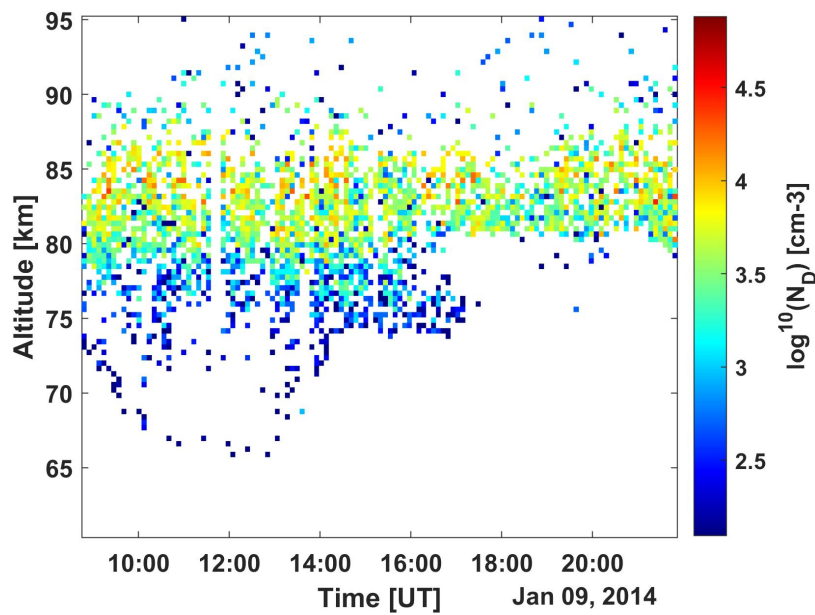
Figure 10. Derived number density (cm^{-3}) of negatively charged dust needed to fit to measured spectrum, shown for the time and altitude range of the observation. The quality (residuals) of these fits are shown in Figures A6-A12 in the Appendix.

Using data from Figure 10 we show the average dust number density derived for charged dust and compare it with the total dust number density from the WACCM-CARMA model (Figure 3 and the average measured electron density. Here, we can see that the average dust density needed follows the total modeled number density above 85 km, but below this altitude the number density decreases, as does the average electron density. The lowest number densities of dust at high and low altitudes are unreliable, as has been discussed. It seems that a peak of the average number density occurs around 85 km. We also considered the influence of the assumed temperature on the result. Comparison of the number densities using the LIDAR temperature and the model temperature (see Figure A5) shows that in the main altitude range where we see dust particles, the dust number density needed is lower for the cases modeled with the LIDAR temperature. This is due to the use of higher temperature measurements (the LIDAR temperature at that altitude is slightly higher than the model temperature), where the higher temperature causes a broader spectrum, and thus the number densities using the model temperature can be too high. In

the right panel of Figure 11 the average dust size is shown, with an increasing average dust size with decreasing altitude. Other methods for determining dust size from radar measurements have shown dust radii close to 1 nm throughout the altitude range (Strelnikova et al., 2007; Rapp et al., 2007).
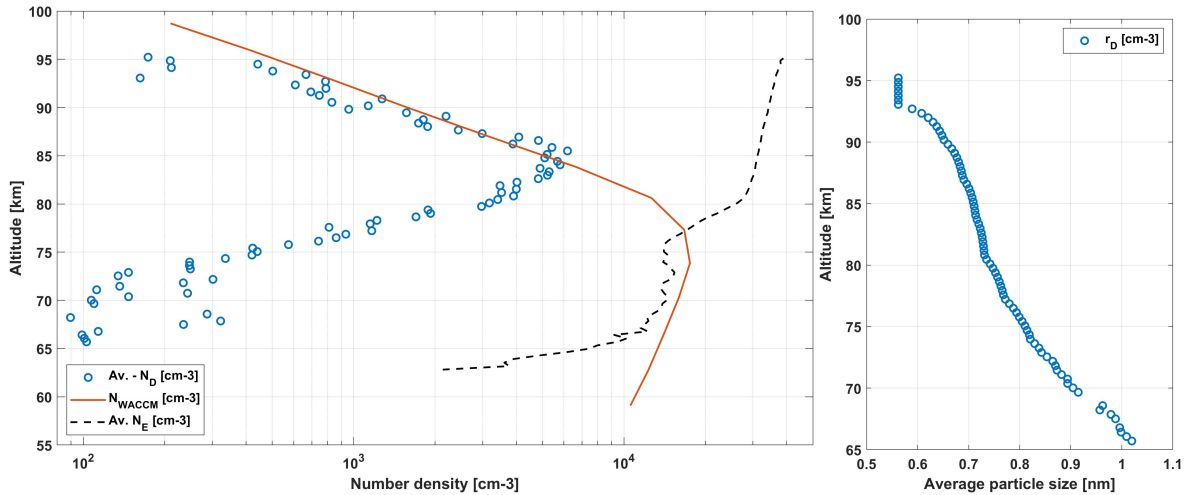

Figure 11. Derived average dust number density (Figure 10) for each altitude compared to the total WACCM-CARMA dust number density (Figure 3) and the average measured electron number density (Figure 1) shown in the left panel. The right panel shows the derived average dust sizes corresponding to the average dust densities in the left panel.

Here, we have assumed that the dust is charged negatively in the range of 0.5-4 nm. However, the model relies heavily on charge neutrality, and thus, by including a positive dust component instead, we get similar average sizes, but with a slightly reduced number density. The average positive number density has a shape similar to the negative average number density distribution in Figure 11. This is due to the fact that when a positive dust component is included, the ion population is reduced in the model and the entire range of positive dust sizes will narrow the spectrum, while small negative dust will broaden the spectrum. Large positive and negative particles influence the model in the same way for each size. It is mainly the decrease of the ion component when positive dust is included, that a reduced number density of positive particles is needed compared to a negative component. Therefore, we cannot say whether any dust present is positively or negatively charged or a combination of both. Only that, if the dust is positively charged, the number densities would be lower than estimated here. According to the Baumann et al. (2015) model, the dust appeared to be mostly positively charged below 80 km during the day and negative particles were found at higher altitudes with a higher number density at night. However, their results were during relatively quiet ionospheric conditions in September, as our observation is in January with apparent high amounts of particle precipitation. Therefore, we cannot conclude where and how much positive and/or negative dust might reside.

We have assumed that the small particles remain uncharged and consequently do not influence the spectrum. If the smallest dust particles were charged negative, they would cause a broadening of the spectrum, and we would need a larger number density of large charged dust to narrow the spectrum adequately to fit the observation. This additional broadening would be

difficult to distinguish from an additional larger dust distribution. Including small positive dust particles would narrow the spectrum, however, due to the size dependence of the model, a very large number of small charged population are needed to narrow the spectrum enough to fit the observed spectrum.

5 Conclusions

Our analysis strongly suggests that the incoherent scatter spectra in the considered height interval are influenced by the presence of charged dust particles and their amount is of similar order as suggested by models. For the spectra that we calculated to fit the observations, we assumed a dust component calculated with the WACCM-CARMA model with dust height profiles from 60 to 100 km and 28 size bins. We assumed a charging probability that varied with size and zero charges for particles smaller than 0.5 nm and varied the absolute dust number density by multiplying the WACCM-CARMA profiles by a constant factor.

We could best evaluate the observations at heights 75 to 85 km. Only a fraction of the observed spectra could be analyzed for higher altitudes, where the observations are limited by the low-altitude resolution of the data used, and at lower altitudes, where the observations are limited because of low electron densities.

We have analyzed the incoherent scatter spectra observed with the EISCAT VHF radar in a selected time interval during ionospheric conditions with a high electron content in winter. The winter season was chosen because when applying model assumptions on the annual variation of the dust, its size distribution and height profile in winter are favorable for generating clear signatures in the spectra. The observation was made from 9 January 2014 approximately 8:00 to 22 UT, after several days with high solar flare activity, which we assume caused the unusually high electron content low down in the atmosphere.

Considerable electron densities were observed for some of the observation intervals even at altitudes as low as 65 km. We investigated the obtained individual spectra in the range of the ion line and after meteor and satellite subtraction and collision frequency correction fitted them with a spectrum including a charged dust component. The temperatures entered in the calculations were taken from LIDAR observations made at the same location as the radar and the temperature of the nrlmsise-00 model when no LIDAR measurements were available. where there is an indication of a lower dust number density using the LIDAR data in the altitude area 75-85 km.

When investigating individual spectra, we found that a large fraction of them were too narrow compared to calculated spectra over a rather large frequency range ($\pm$ 50 Hz). This could not be explained solely by the influence of a charged dust component. The spectra were better reproduced when the ion-neutral collision frequency assumed for the model calculations was varied with factors roughly 0.5 up to 2. Running for comparison a GUISDAP analysis with the collision frequency as a free parameter led to similar results. This mismatch of the collision frequencies was also observed in D-region studies carried out by other groups (Thomas et al., 2023). A possible explanation could be that the applied incoherent scatter models do not sufficiently describe the collisions of the different ionospheric constituents, which are paramount at these altitudes because of the high neutral density.

When including negatively charged dust particles in size ranges of 0.5-4 nm, we see a possible dust layer in the altitude range of 75-85 km with a few good fits below 80 km when the electron density is high enough to produce a good enough spectrum.

13

A comparison to modeled spectra without dust shows that assuming a dust component improves the fit in the frequency range $\pm\,10$ Hz around the peak of the spectrum.

In view of possible future investigations, we note that the neutral density and temperature are best measured independently with other instruments to ensure a good analysis of the spectra. Temperature is quite variable on short timescales due to atmospheric dynamics. Therefore, the combination of radar and LIDAR studies would be helpful. Furthermore, the derivation of the total dust distribution is based on assumptions about dust charging. Especially in the observations studied here, the ionospheric conditions are far from typical, which leads to further uncertainties regarding the charge, which is based on model assumptions anyway. The derived number density and the average size also depend on the assumed dust input parameters. The average dust size is highly dependent on all the small negative dust particles included. Due to their small size, they do not influence the spectrum as much as the large particles and mainly influence its amplitude, while the larger particles narrow the spectrum (Gunnarsdottir and Mann, 2021).

The present study was carried out with data taken with the Manda radar code (Tjulin, 2017). The Manda code is well suited for studying layers in the mesosphere, but measures the ionosphere higher up with low resolution. Different radar codes should be considered for future studies. Since the EISCAT_3D radar measures at similar frequency, our study can be used to estimate the conditions for this new instrument. The transmit power of the phase of the new radar is about a factor of 3 higher than that of the system used in this study, so that the quality of measured spectra may improve. Our study shows, in line with other recent investigations, that the incoherent scatter from the D-region is not sufficiently described with the assumptions on collision rates in the present models used for analysis. Here theoretical investigations could be helpful as the D-region spectra are difficult to understand and influenced by several different parameters, all of which are variable and partly interrelated.

Code and data availability. EISCAT data are available under https://madrigal.eiscat.se/madrigal (accessed on 14 July 2023).

Author contributions. TG outlined the work, selected the observation time, and wrote the original draft of the paper. TG and IM conceived the idea for this work. TG, DH, EH, SN, YO and IM discussed the EISCAT observations and analyses. YO carried out GUIDAP analysis to derive collision rates. NS, SN, and TK provided lidar measurements used. WF provided WAACM-CARMA data used. All authors have read and agreed to the published version of the manuscript.

Competing interests. At least one author is serving on the editorial board of the journal. The authors declare that there is no conflict of interest otherwise. The funders had no role in the design of the study; in the collection, analysis, or interpretation of data; in the writing of the manuscript, or in the decision to publish the results.
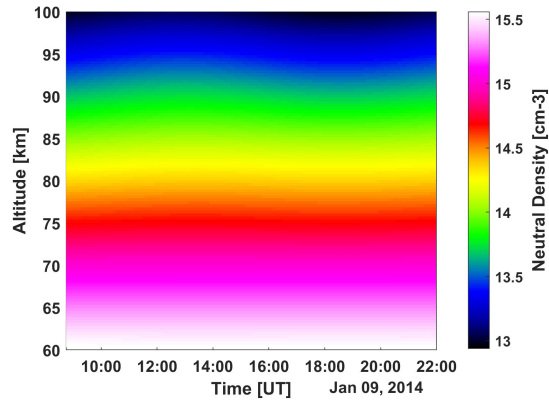
15

Appendix A: Appendix figures

Figure A1. Neutral density used in the model calculations of the spectrum and ion-neutral collision frequency. From the nrlmsise-00 model, using F107 = 188.2, F107 monthly = 151.2, APH = 8
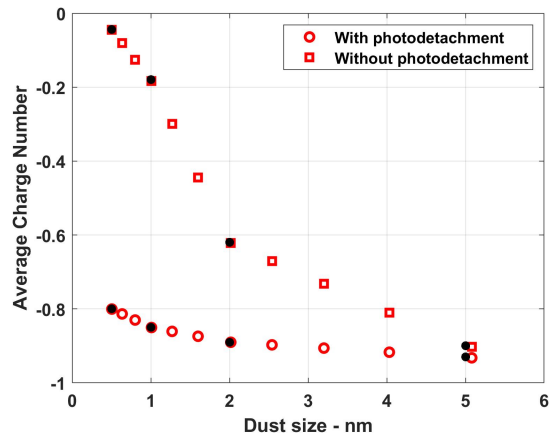

Figure A2. Average charge number for negative dust particles of sizes 0.5-5 nm. The cases shown are with and without photodetachment. The black dots / squares are based on the charging model of Antonsen (2019) and the red data is interpolated to match the size bins from the WACCM-CARMA model.
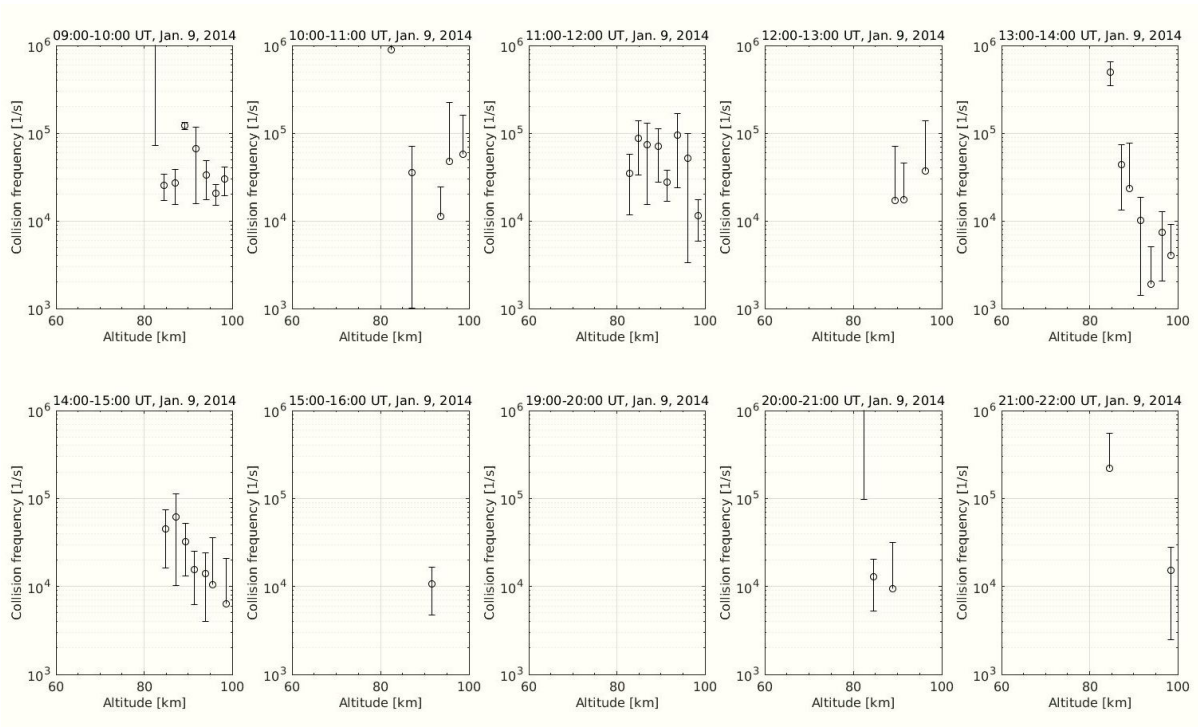
Figure A3. collision frequency estimated from the IS spectrum fitting using GUISDAP. The IS spectrum is integrated for 1 hour and derived as accurately as possible.
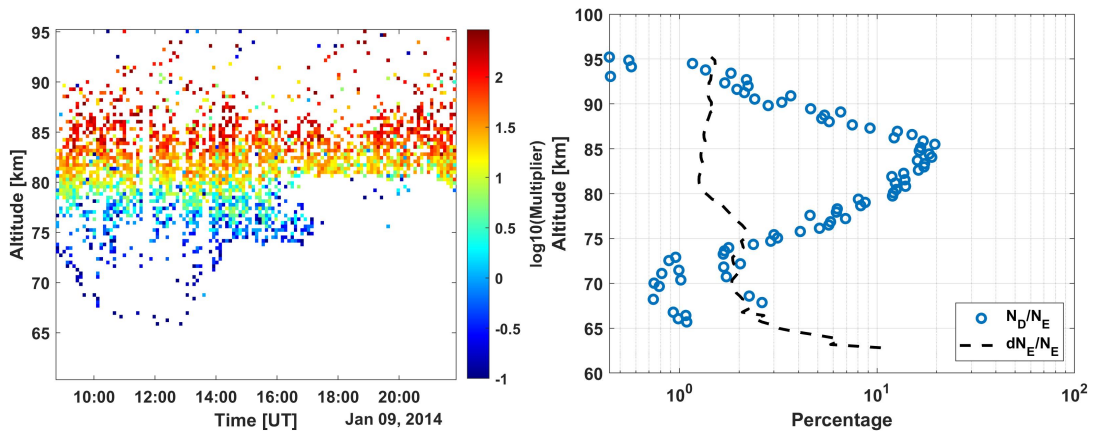
Figure A4. The left panel shows the charge multiplier needed to fit the spectrum of cases shown (log scale). Used for figure 10. The right panel shows the relative number of charged dust to electron density (average) and the relative error of the derived electron density with the EISCAT VHF radar (See Figure 11).
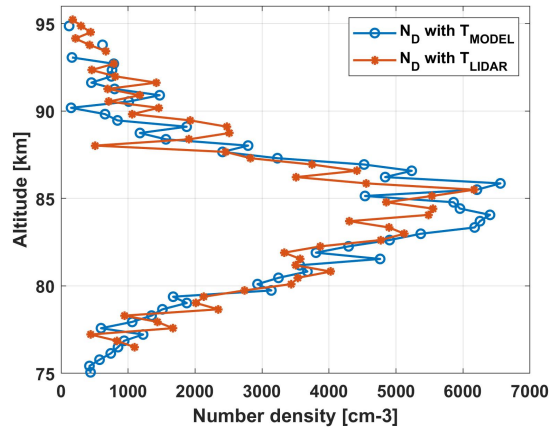
Figure A5. Average derived dust number densities (cm-3) using model temperature from nrlmsise-00 model and the LIDAR temperature respectively.
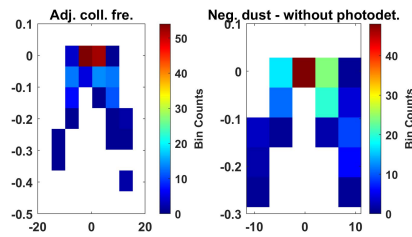
Figure A6. Residuals for 60-65 km. Model points minus observational points around the zero frequency (11 measurement points). Only showing best fits for this altitude segment.
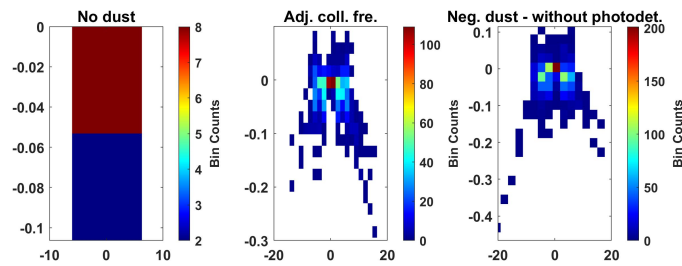

Figure A7. Residuals for 65-70 km. Model points minus observational points around the zero frequency (11 measurement points).
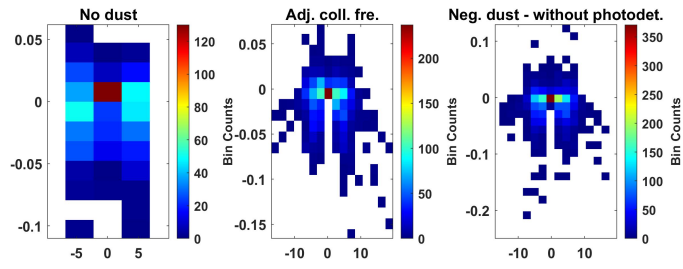
Figure A8. Residuals for 70-75 km. Model points minus observational points around the zero frequency (11 measurement points).
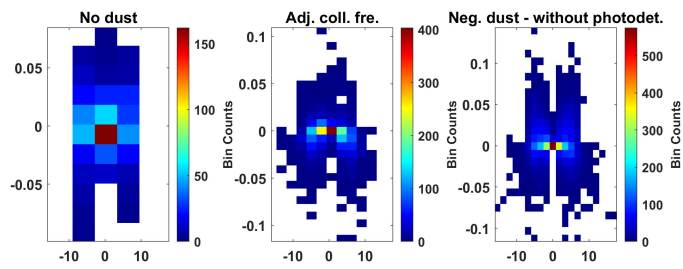

Figure A9. Residuals for 75-80 km. Model points minus observational points around the zero frequency (11 measurement points).
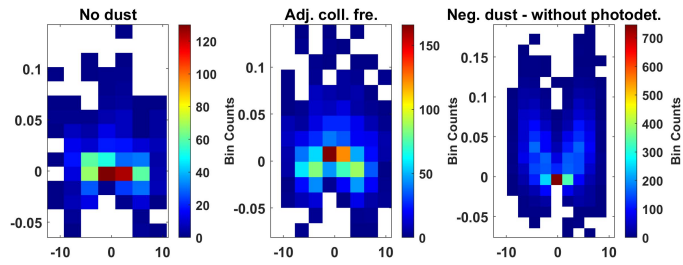

Figure A10. Residuals for 80-85 km. Model points minus observational points around the zero frequency (11 measurement points).
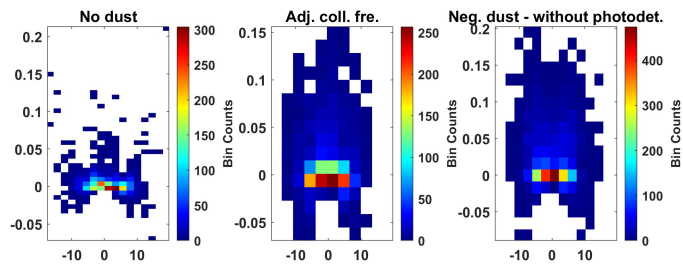

Figure A11. Residuals for 85-90 km. Model points minus observational points around the zero frequency (11 measurement points).
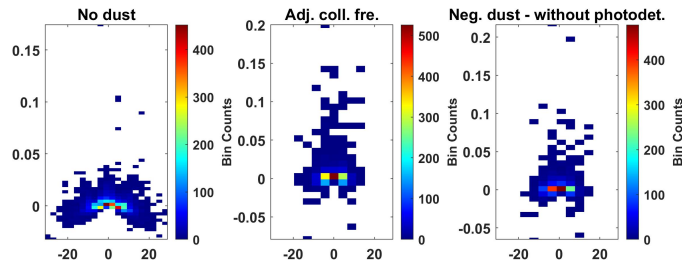
Figure A12. Residuals for 90-95 km. Model points minus observational points around the zero frequency (11 measurement points).

280 **References**

Antonsen, T.: In-situ Measurements of Mesospheric Aerosols - On the observable characteristics of nanoscale ice and meteoric smoke particles, Ph.D. thesis, UiT, 2019.

Antonsen, T., Havnes, O., and Mann, I.: Estimates of the Size Distribution of Meteoric Smoke Particles From Rocket-Borne Impact Probes, Journal of Geophysical Research: Atmospheres, 122, 2017.

285 Bardeen, C., Toon, O., Jensen, E., Marsh, D., and Harvey, V.: Numerical simulations of the three-dimensional distribution of meteoric dust in the mesosphere and upper stratosphere, Journal of Geophysical Research: Atmospheres, 113, https://doi.org/https://doi.org/10.1029/2007JD009515, 2008.

Baumann, C., Rapp, M., Kero, A., and Enell, C.-F.: Meteor smoke influences on the D-region charge balance–review of recent in situ measurements and one-dimensional model results, in: Annales Geophysicae, vol. 31, pp. 2049–2062, Copernicus GmbH, 2013.

290 Baumann, C., Rapp, M., Anttila, M., Kero, A., and Verronen, P. T.: Effects of meteoric smoke particles on the D region ion chemistry, Journal of Geophysical Research: Space Physics, 120, 10–823, 2015.

Brooke, J. S., Feng, W., Carrillo-Sánchez, J. D., Mann, G. W., James, A. D., Bardeen, C. G., Marshall, L., Dhomse, S. S., and Plane, J. M.: Meteoric smoke deposition in the polar regions: A comparison of measurements with global atmospheric models, Journal of Geophysical Research: Atmospheres, 122, 11–112, 2017.

295 Cho, J. Y., Sulzer, M. P., and Kelley, M. C.: Meteoric dust effects on D-region incoherent scatter radar spectra, Journal of atmospheric and solar-terrestrial physics, 60, 349–357, 1998a.

Cho, J. Y., Sulzer, M. P., and Kelley, M. C.: Meteoric dust effects on D-region incoherent scatter radar spectra, Journal of atmospheric and solar-terrestrial physics, 60, 349–357, 1998b.

EISCAT: Real Time Graph, https://eiscat.se/scientist/user-documentation/real-time-graph/, [Online; accessed 13-october-2021].

300 Fentzke, J., Janches, D., Strelnikova, I., and Rapp, M.: Meteoric smoke particle properties derived using dual-beam Arecibo UHF observations of D-region spectra during different seasons, Journal of atmospheric and solar-terrestrial physics, 71, 1982–1991, 2009.

Friedrich, M., Rapp, M., Blix, T., Hoppe, U.-P., Torkar, K., Robertson, S., Dickson, S., and Lynch, K.: Electron loss and meteoric dust in the mesosphere, in: Annales Geophysicae, vol. 30, pp. 1495–1501, Copernicus GmbH, 2012.

Gunnarsdottir, T. L. and Mann, I.: Charged dust in the D-region incoherent scatter spectrum, Journal of Plasma Physics, 87, 905870 502,
305 https://doi.org/10.1017/S0022377821000866, 2021.

Hedin, A. E.: Extension of the MSIS thermosphere model into the middle and lower atmosphere, Journal of Geophysical Research: Space Physics, 96, 1159–1172, 1991.

Hervig, M. E., Brooke, J. S., Feng, W., Bardeen, C. G., and Plane, J. M.: Constraints on meteoric smoke composition and meteoric influx using SOFIE observations with models, Journal of Geophysical Research: Atmospheres, 122, 13–495, https://doi.org/https://doi.org/10.1002/2017JD027657, 2017.

Hervig, M. E., Plane, J. M., Siskind, D. E., Feng, W., Bardeen, C., and Bailey, S. M.: Meteoric smoke and meteor influx from Global Sofie Observations, Authorea, https://doi.org/10.1002/essoar.10506714.1, 2021.

Hunten, D. M., Turco, R. P., and Toon, O. B.: Smoke and dust particles of meteoric origin in the mesosphere and stratosphere, Journal of the Atmospheric Sciences, 37, 1342–1357, 1980.

Hurrell, J. W., Holland, M. M., Gent, P. R., Ghan, S., Kay, J. E., Kushner, P. J., Lamarque, J.-F., Large, W. G., Lawrence, D., Lindsay, K., Lipscomb, W. H., Long, M. C., Mahowald, N., Marsh, D. R., Neale, R. B., Rasch, P., Vavrus, S., Vertenstein, M., Bader, D., Collins, W. D., Hack, J. J., Kiehl, J., and Marshall, S.: The Community Earth System Model: A Framework for Collaborative Research, Bulletin of the American Meteorological Society, 94, 1339 – 1360, https://doi.org/https://doi.org/10.1175/BAMS-D-12-00121.1, 2013.

Lehtinen, M. S. and Huuskonen, A.: General incoherent scatter analysis and GUISDAP, Journal of Atmospheric and Terrestrial Physics, 58, 435–452, https://doi.org/https://doi.org/10.1016/0021-9169(95)00047-X, selected papers from the sixth international Eiscat Workshop, 1996.

Marsh, D. R., Mills, M. J., Kinnison, D. E., Lamarque, J.-F., Calvo, N., and Polvani, L. M.: Climate Change from 1850 to 2005 Simulated in CESM1(WACCM), Journal of Climate, 26, 7372 – 7391, https://doi.org/https://doi.org/10.1175/JCLI-D-12-00558.1, 2013.

Mathews, J. D.: The effect of negative ions on collision-dominated Thomson scattering, Journal of Geophysical Research: Space Physics, 83, 505–512, 1978.

Megner, L., Rapp, M., and Gumbel, J.: Distribution of meteoric smoke - sensitivity to microphysical properties and atmospheric conditions, Atmospheric Chemistry and Physics, 6, 4415–4426, https://doi.org/10.5194/acp-6-4415-2006, 2006.

Megner, L., Siskind, D., Rapp, M., and Gumbel, J.: Global and temporal distribution of meteoric smoke: A two-dimensional simulation study, Journal of Geophysical Research: Atmospheres, 113, 2008.

NASA: Solar Proton Events from 1976, https://umbra.nascom.nasa.gov/SEP/, [Online; accessed 20-june-2023].

Nozawa, S., Kawahara, T., Saito, N., Hall, C., Tsuda, T., Kawabata, T., Wada, S., Brekke, A., Takahashi, T., Fujiwara, H., et al.: Variations of the neutral temperature and sodium density between 80 and 107 km above Tromsø during the winter of 2010–2011 by a new solid-state sodium lidar, Journal of Geophysical Research: Space Physics, 119, 441–451, 2014.

Plane, J. M., Feng, W., and Dawkins, E. C.: The mesosphere and metals: Chemistry and changes, Chemical reviews, 115, 4497–4541, 2015.

Plane, J. M. C.: Cosmic dust in the earth's atmosphere, Chem. Soc. Rev., 41, 6507–6518, https://doi.org/10.1039/C2CS35132C, 2012.

Rapp, M. and Lübken, F.-J.: Polar mesosphere summer echoes (PMSE): Review of observations and current understanding, 2004.

Rapp, M., Strelnikova, I., and Gumbel, J.: Meteoric smoke particles: Evidence from rocket and radar techniques, Advances in Space Research, 40, 809–817, 2007.

Rapp, M., Plane, J., Strelnikov, B., Stober, G., Ernst, S., Hedin, J., Friedrich, M., and Hoppe, U.-P.: In situ observations of meteor smoke particles (MSP) during the Geminids 2010: constraints on MSP size, work function and composition, in: Annales geophysicae, vol. 30, pp. 1661–1673, Copernicus Publications Göttingen, Germany, 2012.

Rosinski, J. and Snow, R.: Secondary particulate matter from meteor vapors, Journal of Meteorology, 18, 736–745, 1961.

Saunders, R. W. and Plane, J. M.: A photo-chemical method for the production of olivine nanoparticles as cosmic dust analogues, Icarus, 212, 373–382, 2011.

345 Strelnikova, I., Rapp, M., Raizada, S., and Sulzer, M.: Meteor smoke particle properties derived from Arecibo incoherent scatter radar observations, Geophysical Research Letters, 34, 2007.

Thomas, N., Kero, A., and Virtanen, I.: Study of D region ionosphere using incoherent scatter radar measurements, https://doi.org/https://doi.org/10.5194/egusphere-egu23-12698, 2023.

Tjulin, A.: EISCAT experiments, EISCAT Scientific Association,(March), 2017.